Systems Definition Space Based Power Conversion Systems

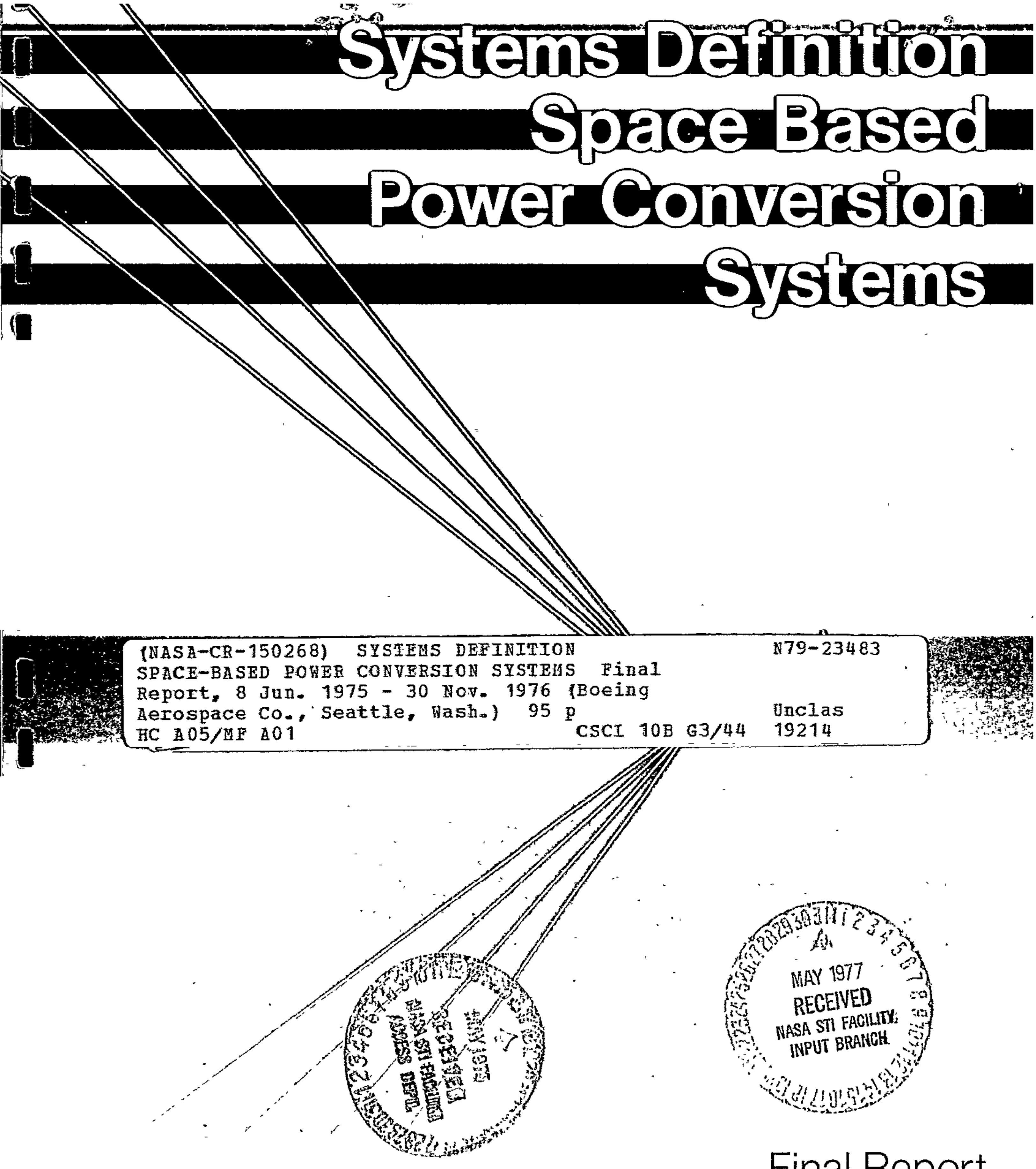

(NASA-CR-150268) SYSTEMS DEFINITION N79-23483
SPACE-BASED POWER CONVERSION SYSTEMS Final
Report, 8 Jun. 1975 - 30 Nov. 1976 (Boeing
Aerospace Co., Seattle, Wash.) 95 p Unclas
HC A05/MF A01 CSCL 10B G3/44 19214

Final Report
Detailed Technical Report

BOEING

FINAL REPORT

TECHNICAL REPORT
(DPD ITEM MA-04)

SYSTEMS DEFINITION
SPACE-BASED
POWER CONVERSION SYSTEMS

Submitted to
The National Aeronautics and Space Administration
George C. Marshall Space Flight Center

Study Contract
NAS8-31628

The Boeing Aerospace Company

D180-20309-2

CONTENTS

CONTENTS (Continued)

LIST OF ILLUSTRATIONS

LIST OF ILLUSTRATIONS (Continued)

LIST OF ILLUSTRATIONS (Continued)

1.0 INTRODUCTION AND BACKGROUND

1.1 INTRODUCTION

1.1.1 The Study Effort

This study was initiated on June 8, 1975 and continued until November 30, 1976. Its purpose was the investigation of potential space-located systems for the generation of electrical power for use on Earth. These systems were of three basic types:

1) Systems producing electrical power from solar energy;

2) Systems producing electrical power from nuclear reactors;

3) Systems for augmenting ground-based solar power plants by orbital sunlight reflectors.

Systems 1) and 2) would utilize a microwave beam system to transmit their output to Earth.

Configurations implementing these concepts were developed through an optimization process intended to yield the lowest cost for each. A complete program was developed for each concept, identifying required production rates, quantities of launches, required facilities, etc. Each program was costed in order to provide the electric power cost appropriate to each concept.

1.1.2 Contributers

Mr. Walter Whitacre was contracting officer's representative at Marshall Space Flight Center. At Boeing, the study effort was directed by Daniel Gregory. Subcontractors were: the Garrett Corporation (thermal engines), directed by Mr. Anthony Pietsch, and the Thermo Electron Corporation (thermionics) directed by Dr. Peter Oettinger. Dr. J. Richard Williams of the Georgia Institute of Technology was the consultant on space-based nuclear reactors.

1.1.3 Related Efforts

Studies which were underway during some portion of the study and which contributed to the data base are:

1) NAS8-31308 (MSFC), "Space-Based Solar Power Conversion and Delivery Systems Study" Econ Incorporated.

2) NAS9-14323 (JSC), "Future Space Transportation Systems Analysis Study," Boeing Aerospace Company.

3) NAS3-17835 (LeRC), "Microwave Power Transmission System Studies" Raytheon/Grumman.

4) NAS9-14710 (MSFC), "Systems Concepts for STS-Derived Heavy Lift Launch Vehicle Study" Boeing/Grumman.

5) Contract NAS8-31444 (MSFC), "Payload Utilization of SEPS" Boeing/GE.

6) Contract E-(04-3)-1111 (ERDA) "Central Receiver Solar Thermal Power System," Boeing Engineering and Construction.

1.2 BACKGROUND

1.2.1 The Space Power Concept

Figure 1-1 may be used to understand the basic principle of the Satellite Power Station (SPS). A power generating system produces electric power which is converted into a narrow (total divergence angle of approximately 1/100 degree) microwave beam by the microwave transmitter. These systems are located in equatorial geosynchronous orbit and thus remain in line-of-sight of their associated microwave power receiving stations on the ground. At these stations the microwave power is converted into a form of electricity suitable for insertion into the local power network. The energy source for the SPS would be sunlight, or alternatively, nuclear reactors.

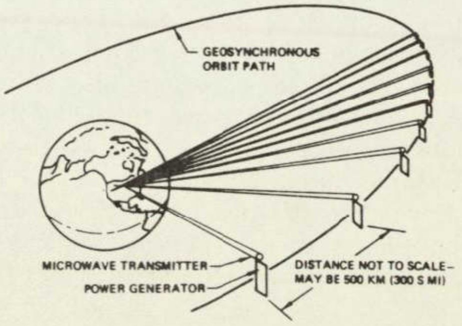

Fig. 1-1. Satellite Power Stations

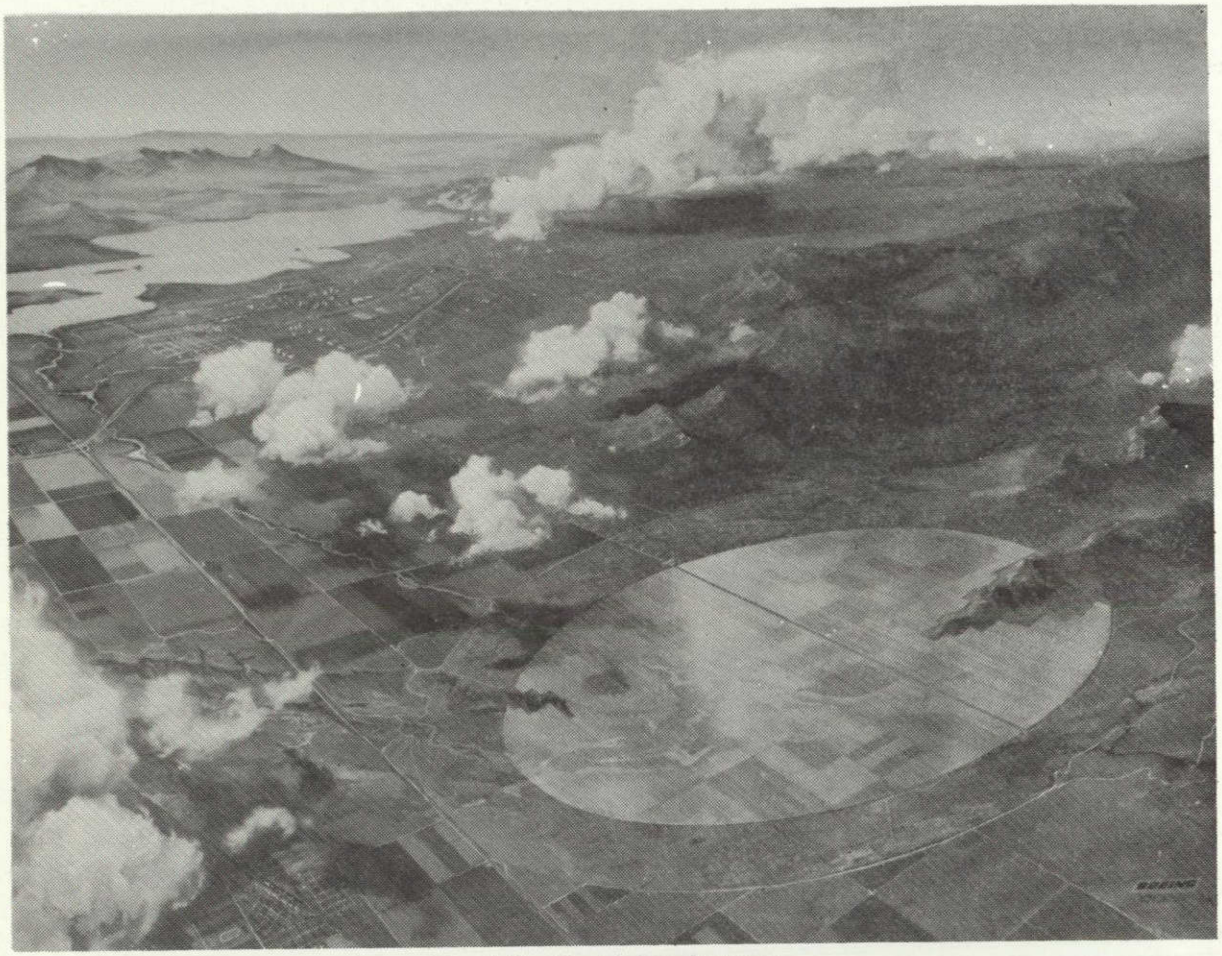

Fig. 1-2. Receiving Antenna

The receiving stations for the SPS consist of a large number ($\approx 10^9$) of small receiving antennas integrated in an oval array. Rectification of the received energy to direct current is accomplished by circuit elements which are integral to the antennas. Figure 1-2 shows such an array.

Since the antenna may block most of the microwave energy but would be nearly transparent to sunlight, it is possible that agriculture could be accomplished beneath it. Surrounding the antenna is a buffer zone to contain those microwave "side-lobes" which are more energetic than the continuous exposure standard (assumed to be more than 10 times more stringent than the current standard which is 10 mW/cm^2). These antennas could be placed relatively near demand points (note the city in the background of Figure 1-2).

Figure 1-3 shows, as an example, one of the concepts studied; a solar Brayton SPS. Four power generator modules feed the circular microwave transmitter. Each power module consists of a reflector which concentrates solar energy into a cavity absorber at the focal point. The resultant high temperatures are used to energize turbomachines which turn electrical generators which power the transmitter.

In this study the technical and economic practicality of these systems was investigated. While these systems produce large quantities of power (e.g., 10,000,000 kilowatts per satellite), the forecasted demands of the United States alone are sufficient to require a significant number of satellites. In the program baselined in this study, 60 satellites are made operational by the year 2016.

1.2.2 Auxiliary Systems

The criterion for optimization of these systems was minimum cost per kilowatt hour of energy produced (while maintaining set standards on factors such as environmental impact). To achieve low cost

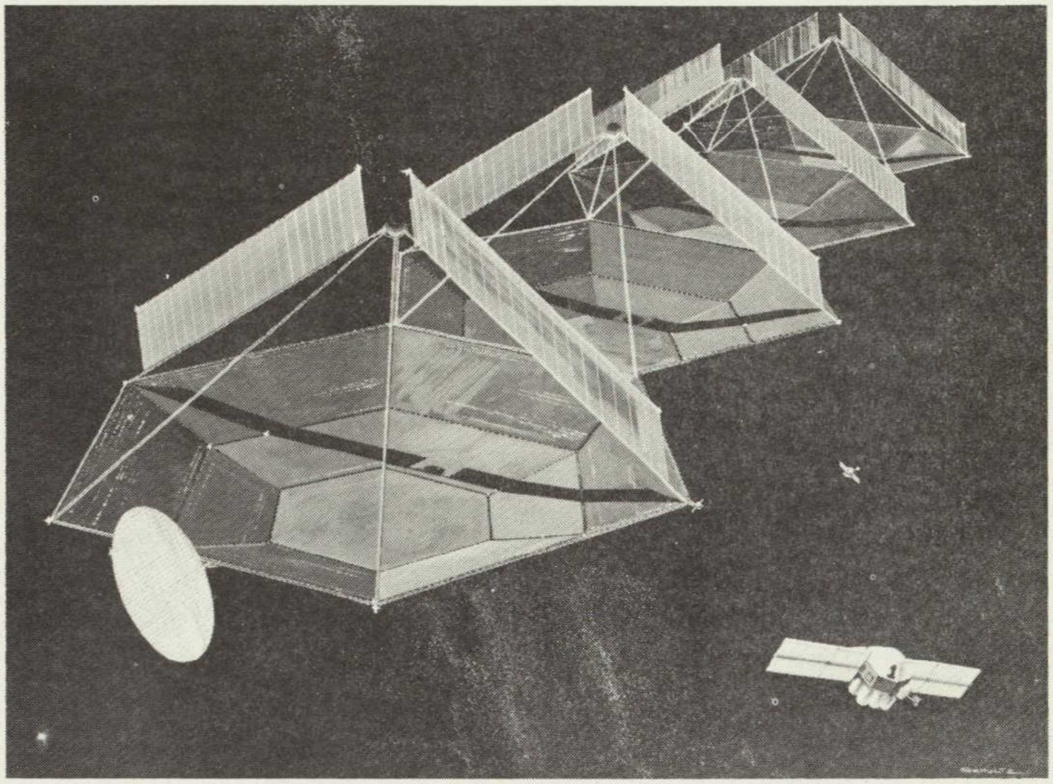

Fig. 1-3. Solar Turbomachine Power Satellite Option

per kWhr, all significant elements of the program must also be appropriately low in cost. This includes not only the power generation and transmission systems, but also the systems used for space transportation and space assembly. These auxiliary systems were of necessity considered in this study although their investigation was not a primary goal. An example of an auxiliary system is the heavy lift launch vehicle ("space freighter") used to transfer SPS material to low orbit. It is shown in Figure 1-4 during the landing phase; a portion of the ascent propulsion system is used to

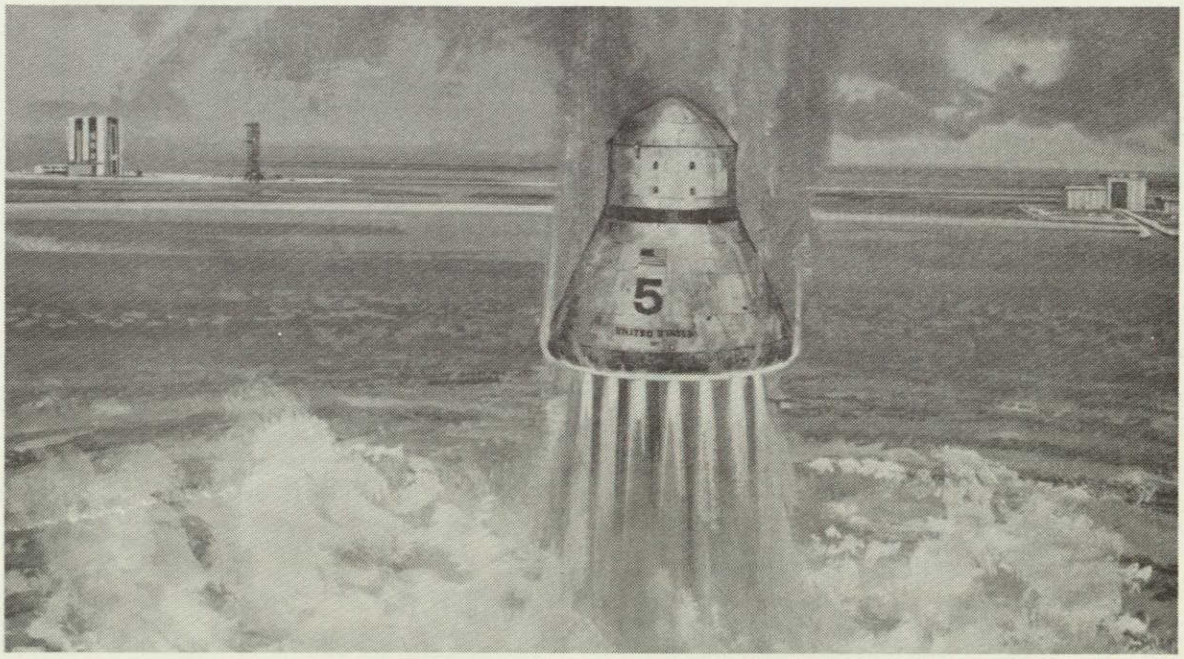

Fig. 1-4. "Space Freighter" Lands

affect a soft landing in water. Thus the vehicle is available for reuse, contributing to the required low operational cost.

Another significant auxiliary system is the orbital construction facility required to provide the necessary production rate for satellite power stations. A concept for such a station is shown in Figure 1-5.

1.2.3 Energy Overview and the SPS

Ever increasing rates of consumption of the Earth's available fossil and nuclear fuel stores are characteristic of this latter half of the twentieth century. Global population is increasing, and so also is the fraction of that population which forms the energy consuming "middle class." This is true not only in the U.S., Russia, Japan, etc., but in the so called emerging nations.

As a consequence, we may expect these existing global energy sources to last only to these rather approximate dates: oil, 1995 to 2005; coal, 2030 to 2080; uranium (without breeder reactors), 2020 to 2050. As they are consumed, four additional factors come into play: first their cost steadily increases as remaining quantities become more difficult to obtain (e.g., thinner coal veins). Second, their consumption releases additional pollutants to the biosphere (for example, CO_2 removed from the atmosphere millenia ago by plants, which formed coal, is now being returned). Third, since energy sources are geographically concentrated (e.g., most coal in U.S., most oil in Middle East), a potential for great international tension and even war may be created as reserves dwindle. Fourth, nuclear fission involves by-product materials which may be used for weapon production by either governments or outlaws.

Thus some attention is now turning to "renewable" or "non-depletable" energy sources. Primary candidates for electric power appear to be nuclear breeder reactors, nuclear fusion and solar energy.

These are characterized by varying degrees of complexity, technical risk, pollution, cost, etc. Each could reduce our dependence on imports, and if adopted by other nations, serve to reduce international tensions.

Solar power may be used directly for heating and cooling; it may also be used for the production of

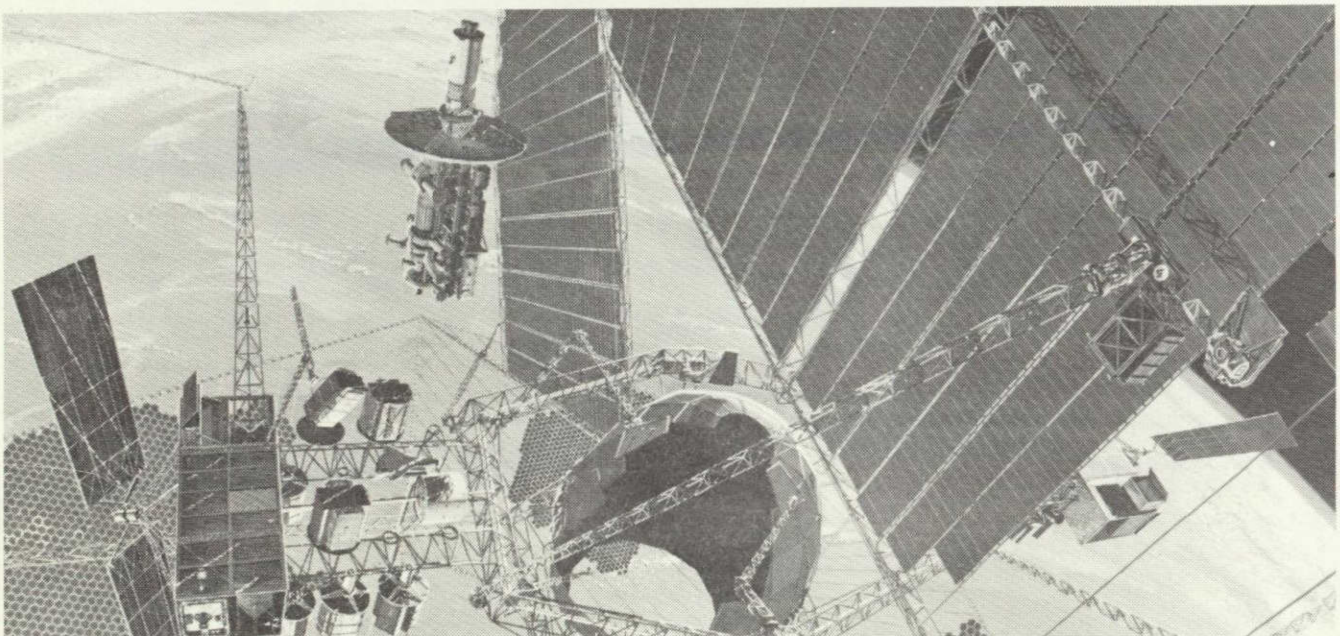

Fig. 1-5. Orbital Construction Facility

electricity. Primary concepts for electric power production on Earth are photovoltaic (solar cell arrays or "farms") and the thermal engine "tower top." In the tower top concept a field of steerable mirrors (heliostats) focuses energy onto a tower-mounted heat absorber. This heat can provide steam or some other fluid to turn turbogenerators.

Solar power plants on Earth suffer from the diffuse nature of solar radiation (insolation), reduction in insolation from clouds, haze, etc., the varying angle of the sun's rays and, of course, nightfall. A power plant located in space can receive nearly direct, unfiltered sunshine almost without interruption. For a given reception area, a space system will receive six times more energy per year than will the "sunniest" areas on Earth, and about 15 times more energy than a U.S. location with "average" weather.

In geosynchronous orbit 35,786 kilometers (22,236 statute miles) above the equator, a satellite has an orbital period of 24 hours and so remains in constant line of sight to stations on the ground. Solar power satellites in such orbits would generate electric power which would be converted to microwaves and beamed to receiving stations for distribution to consumers as conventional electric power. Receiving stations in various parts of the U.S. could be associated with a number of satellites in orbit.

Thus satellite systems can provide high availability "base load" power without the energy storage or backup facilities which greatly impact the cost and operational flexibility of terrestrial solar power stations. Space offers other advantages:

- Thermal pollution from the power generation process is released in space rather than to the biosphere.
- The low gravity potential permits low-mass construction of the large areas necessary to intercept the solar energy. Consequently the total amount of resources used is less than for ground solar stations.
- No oxidation or corrosion.
- No tidal waves, earthquakes, etc.
- Far removed from demonstrators, terrorists, etc.

Other potential advantages of the SPS concept include contribution to U.S. energy independence, possibility of export, reduced pollution and improved economic stability (from reduction of inflationary pressures).

2.0 PROGRAMMATICS

2.1 DERIVATION OF SATELLITE ENERGY SYSTEM PROGRAM DEFINITION

The methodology used to select the system size guidelines is as follows:

Background—Utilization of space-based power generation could conceivably occur as a legislated action, prompted by the resultant increase of national energy independency, reduced pollution, infinite source, etc. However, about three-fourths of our electric power currently is produced by private utilities, suggesting that economics may be a major factor influencing space-based power incorporation. Thus, market elasticity must be considered, i.e. sales will be influenced by the price of the product.

Many factors have contributed to the increases in installed capacity (kW) and consumption (kWh).

1) Population growth—from 1956 to 1973 the rate was 1.3% per year. The rate is predicted to decline to 0.8% in the 1973 to 1990 period. Resultant populations, millions (1)*:

1964	192
1974	212
1984	231
1994	249

2) Rising standard of living—disposable income per person has been increasing; the trend is expected to continue (1):

1964	3248
1974	4592
1984	5677
1994	7071

3) Relative reduction in electricity cost—as pointed out by Hannon (2), the cost of electricity energy has reduced relative to labor costs (electricity does not strike for higher wages). It thus seems appropriate that about 40% of our national electricity use is for process heat and industrial power while only 9% goes for lighting (3). In the following plot (Figure 2-1) from (2) the ratio of manufacturing workers hourly wage to industrial kWh cost of electricity is represented as 1.0 in 1951 on the ratio index scale.

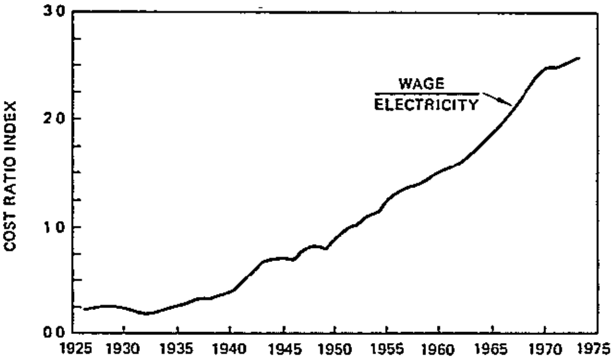

Fig. 2-1. Electricity/Labor Cost Ratio

Forecasts—Figure 2-2 shows trends in national installed generating capacity. Note the difference between the 1973 and 1974 forecasts. It is significant that the 1973 article in (5) was titled "Utilities Plan Expansion to Meet Record Demands" and that the 1974 title in (1) was "Slower Growth In Sales and Peaks Sparks Sharp Cut in Expansion Plans and Cost."

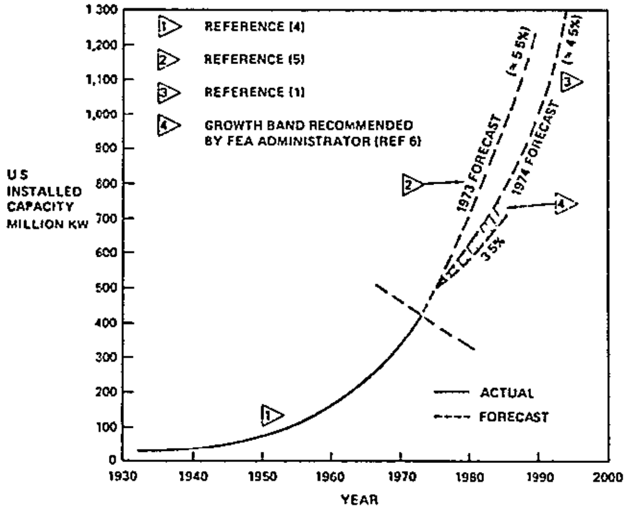

Fig. 2-2. Growth in U.S. Installed Capacity

An explanation for the change in forecast is given in (1): at the end of 1973 an increase of 33,100 MW in the summer peak requirement was forecast. An increase of 43,607 MW in capacity was planned for 1974 to meet this peak, retire some obsolescent units and raise the national reserve margin to 21%. However, energy conservation (partly from recession-caused production decreases) cut the load growth, to only 15,530 MW, resulting in a gener-

---

*References are given at the end of this session.

ating margin of 26.2%. Consequently, some of this margin can be applied to subsequent growth needs, depressing the growth curve. Figure 2-3 shows variation of this margin with time. 18% is generally considered by utilities to be desirable: the margin was 16.6% in 1969 when reductions and curtailments occurred.

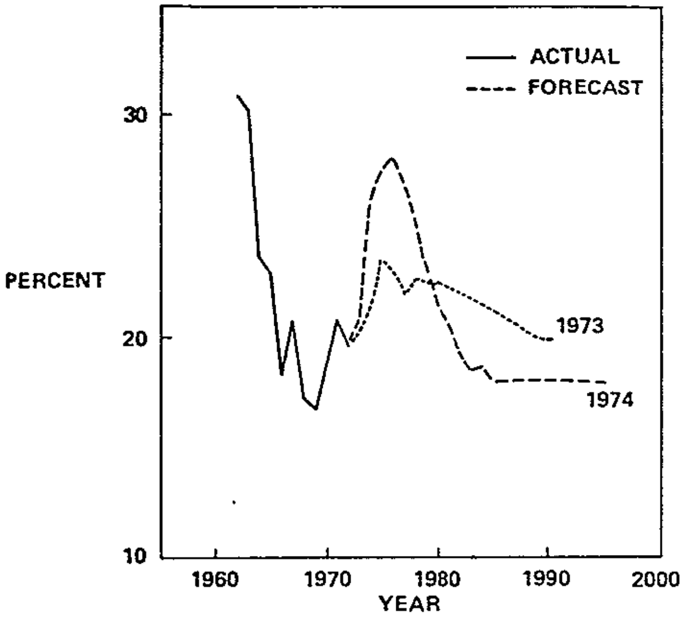

GROSS PEAK MARGIN (FROM 1 & 5)

Fig. 2-3. U.S. Capacity Margin

Some authors have forecast and/or recommended very low or even zero energy growth rate. Hannon (2) recommends a more labor intensive economy, i.e. one in which, in essence, human muscles perform rather than electric motors, thereby making more (lower paying) jobs. One factor is the growing labor pool resulting from population growth; if the birth rate instantly dropped to zero, the labor pool would still increase in size for two decades.

A more middle-of-the-road view is that energy growth is essential to economic health. Federal Energy Administrator Zarb has recommended a 3.5% to 4.5% installed capacity growth rate for 1975 to 1985 (6). This range was plotted in Figure 2-2. The actual growth rate for 1975 was 3.0% (8).

It is possible for national energy consumption to remain constant while the amount of electricity generated increases. In 1968 the U.S. Energy Consumption was as shown in Table 2-1 (from 3).

In 1968, 21.2% of the energy expended went to produce electricity. The last column shows a potential of 70.7% utilization without significant changes in energy use technology; for example, electricity could be used for all process heat.

Table 2-1. 1968 U.S. Energy Consumption Patterns by End Use

	Natural gas utilization by %	Oil utilization by %	Coal utilization by %	Electricity by %	% of total U.S energy consumption	Potential electrical by %
Transportation					24.9	
Aircraft		} 49.4				
Vehicles	3.1					
Trains		2.1		0.4		1.1
Ships		2.2				
Chemical feedstock	2.3	10.2	1.1		5.5	
Process heat	40.7	9.7	37.3	2.5	26.2	26.2
Industrial power				37.2	7.9	7.9
Lighting				9.3	2.0	2.0
Miscellaneous					13.6	13.6
Household	7.0	0.8		16.9		
Commercial	3.3			23.1		
Industrial				7.1		
Space heating					19.9	19.9
Home	16.5	11.2		3.5		
Commercial	6.2	9.0	4.3			
Industrial	3.1	0.7	3.0			
Electricity gen	17.8	4.7	54.3	—	—	
Totals, %	100.0	100.0	100.0	100.0	100.0	
% of total U.S. consumption	26.5	42.1	10.1	21.2	—	70.7

Current Predictions—Figure 2-4 shows historical (4) and forecasted (1 and 5) annual additions to U.S. installed capacity. Note that these are net additions after retirement of obsolete capacity. Actual sales are 1% to 2% greater. Again note the dramatic changes resulting from the capacity margin produced by reduced electricity consumption. The projected 1973 addition rate for the year 1990 was 64 GW (64000 MW); the 1974 projection is for 53 GW per year for 1990.

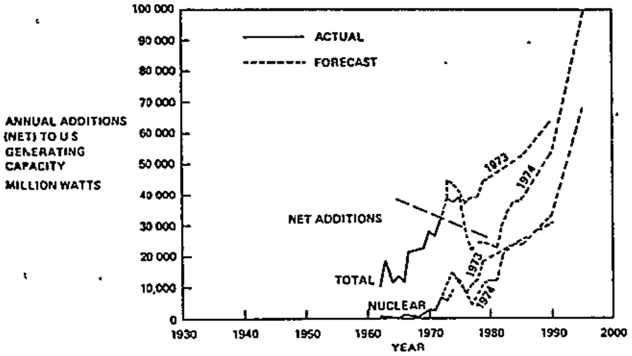

Fig. 2-4. Annual Additions to Installed Capacity

Figure 4 also shows the trend and forecast for the addition rate of nuclear-generated electricity. In 1973, nuclear provided 4.8% of our capacity. This was 16 years from the initial power reactor and nine years after the first "commercially competitive" reactor of 1964. In the 16 years from 1964 until 1980 nuclear energy is forecasted to grow to capture 13.6% of the electric power market. In another 15 years it will represent 30% of our capacity (but provide over 50% of the kWh) (1). It thus appears reasonable to assume early market capture rates of ≈15% for SPS (assuming equivalent economics). In England, nuclear capacity was added at approximately five times the percentage rate of the United States. Should superior economics be achieved, i.e., very low costs for space-based power, the capture rate could be even higher. Other factors could also accelerate space power incorporation, such as nuclear power moratoriums or legislation which levies the full "social" costs of fossil fuel usage on the electric power customer. The current social cost for the use of coal may be 13 to 15 mills/kWh (7).

2.2 REQUIREMENTS

The following requirements were applied throughout the study:

1. Provide electrical power for commercial utilization in U.S.
2. System sizes for 5 and 10 GW ground output.
3. Power source in geosynchronous orbit, microwave power transfer.
4. Program schedule highlights:

12/31/79	End of Concept Definition and Analytical Efforts, Preferred Concept Chosen, Technology Verification Plan Complete.
12/31/87	Technology Verification Activities Complete for Go-Ahead for Phase C/D on SPS, HLLV, LTV, etc.
1/1/96	Initial Operational Capability of Full Scale Power Satellite

5. Technology Level: The technology levels shall be those available for subscale (e.g., lab) demonstration five years prior to operational use.
6. Program Definition: The expansion rate of U.S. electric power generation shall be assumed to be 4.5% per year, the fraction of total capacity from satellite power shall be:
   a. 10 Years after IOC.10%
   b. 20 Years after IOC.25%
7. Nominal life of the space power units and the ground receiving stations shall be 30 years, assuming appropriate maintenance.
8. System safety is to be such that:
   a. No failure mode shall cause non-program personnel to be exposed to microwave radiation flux greater than the current U.S. exposure standard of 10 mW/cm^2.
   b. Public exposure to nuclear radiation from either system operations or failure (including reactor meltdown/vaporization/release) shall not exceed the current U.S. public exposure standard.

9. The system optimization criterion shall be minimum cost per kilowatt hour: both recurring and non-recurring costs shall be recovered from operational revenues.

10. Man will be utilized in space as required appropriate to the above minimum cost goal.

11. Nuclear reactors shall be of the breeder type.

12. In-space power conversion will be by thermionic diodes or closed Brayton cycle thermal engines, or by photovoltaic cells.

13. The low orbit boost vehicle shall be based on the Class 4 type from the Heavy Lift Launch Vehicle Study (NAS8-14710).

14. Launch latitude shall be assumed to be 28.5°N.

15. Radiator system metoroid resistance capability shall be such as to provide a degradation of 30% or less of the total area without repair or replacement of damaged panels, over a period of 30 years. This does not preclude such repair or replacement.

16. Program economics analyses shall be based on a 30-year investment horizon and a 7.5 percent discount rate.

17. Availability of the Space Shuttle shall be assumed.

18. Mass statements will not include a contingency factor.

Requirement 6, above results in a requirement for 600 GW ground output capability by the SPS system by the year 2016. This can be supplied by either 120 5-GW units or 60 10-GW units.

Requirement 15 sets an arbitrary requirement that requires 1% of the Brayton radiator systems to be repaired in each year of operation. This is not necessarily the optimum maintenance. (The optimum maintenance level would strike a proper balance between meteoroid protection mass—hence cost—and maintenance cost to yield a minimum overall cost for power.)

REFERENCES

1. Electrical World, September 15, 1974.

2. Hannon, B., "Energy Conservation and the Consumer," Science, 11 July, 1975 (Vol. 189, No. 4197).

3. Hauser, L. G., "Future Trends in Energy Supply," 1974 Textile Industry Conference.

4. Moody's Public Utility Manual, 1974.

5. Electrical World, September 15, 1973.

6. "World News Beat," Electrical World, July 1, 1975.

7. Morgan, M. G., Barkovich, B. R. and Meier, A. K., "The Social Costs of Producing Electric Power from Coal: A First Order Calculation." IEEE Proceedings, Vol. 61, No. 10, October 1973.

8. Electrical World, December 1, 1976.

3.0 ALTERNATIVE POWER GENERATION APPROACHES

3.1 CONCEPTS INVESTIGATED

The alternative satellite power systems shown in Table 3-1 were investigated:

The last concept does not generate power in space; a mirror system in geostationary orbit would reflect sunlight to an area on Earth, potentially allowing night operation of ground solar power plants.

3.2 SOLAR THERMIONIC, DIRECT RADIATION COOLED (CONCEPT 1)

In a thermionic diode, electrons are produced at the emitter (cathode) due to its elevated temperature, and travel to the lower temperature collector (anode). The circuit is completed through the load. Several processes within the emitter-collector gap tend to reduce the efficiency of power generation from the applied thermal energy. For example, the electrons in the gap tend to repel those being produced at the emitter.

The diodes are mounted in the wall of the solar cavity absorber; the emitters are heated by the concentrated solar energy. By allowing the collectors to dissipate waste heat to space, the temperature differential required for operation is produced. Fins are added to the collectors to improve cooling.

Individual diodes have outputs of approximately 0.8 volts, and it is not practical (due to insulation breakdown) to use series strings to produce the converter/transformer assemblies are used to provide the DC necessary to energize the transmitter. up the voltage. An AC to DC converter is used to provide the DC necessary to energize the transmitter.

The solar thermionic direct radiation cooled system is shown in Figure 3-1.

3.3 SOLAR THERMIONIC, LIQUID COOLED (CONCEPT 2)

In this configuration a liquid metal cooling loop is used to remove waste heat from the diode collectors. In effect, the coolant loop couples the diodes to a greater radiating area than is practical for fins directly attached to the diodes, thereby producing a lower collector temperature, a greater temperature differential across the diode and greater electrical output. Thus the diodes are more efficient, so that fewer diodes are required; however, active cooling uses power drawn from the diodes and requires a liquid metal loop with thermal radiator.

Converter/transformer assemblies are used to step-up the diode output voltage. An AC to DC

Table 3-1. Alternative Power Systems

Concept	Energy Source	Energy Converter
1	Solar	Direct Radiation Cooled Thermionic
2	Solar	Liquid Cooled Thermionic
3	Solar	Closed Brayton Cycle
4	Solar	Thermionic/Brayton Cascade
5	Solar	Silicon Photovoltaic
6	Solar	Gallium Arsenide Photovoltaic
7	Nuclear	Thermionic
8	Nuclear	Closed Brayton Cycle
9	Solar (Light Reflector)	Ground-Based Solar Power Plants

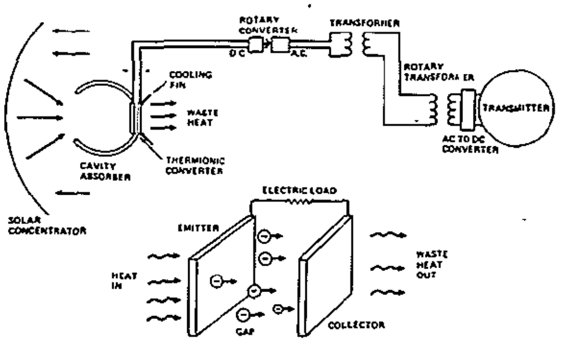

Fig. 3-1. Solar Thermionic Direct Radiation Cooled System

converter is used to provide the DC necessary to energize the transmitter.

The solar thermionic, actively-cooled system is shown in Figure 3-2.

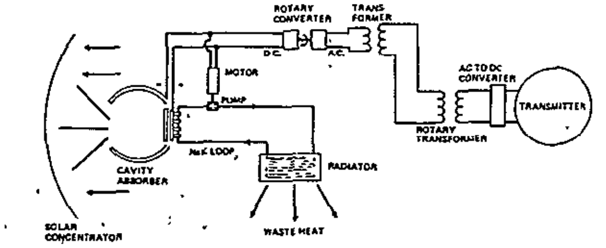

Fig. 3-2. Solar Thermionic, Liquid-Cooled System

3.4 SOLAR CLOSED BRAYTON CYCLE (CONCEPT 3)

The Brayton cycle turbomachine provides a rotating shaft output which drives the generators. Thermal energy is added to the helium working fluid in heat exchanger tubing located within the cavity absorber. The hot gas is expanded through the turbine, providing power to turn both the compressor and generator. The recuperator exchanges energy across the loop to increase the system efficiency. Waste heat is rejected through a gas-to-liquid heat exchanger to a liquid metal cooling loop; the liquid metal pumps use power drawn from the generators.

The 50,000 volt AC output of the generators is stepped-up to 382,000 volts in transformers; this high voltage facilitates on-board distribution. Step-down occurs in the rotary transformers. An AC to DC converter is used to provide the DC required to energize the transmitter.

The solar Brayton cycle system is shown in Figure 3-3.

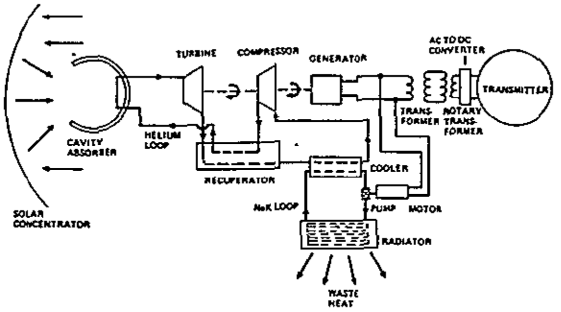

Fig. 3-3. Solar Brayton Cycle System

3.5 SOLAR THERMIONIC/BRAYTON CYCLE CASCADE (CONCEPT 4)

This "cascaded" system offers potentially high efficiency. All waste heat from the thermionic diodes is available to the Brayton cycle; the diodes are cooled by the helium flow in the Brayton loop. The Brayton loop is cooled by a liquid metal radiator.

The DC output of the diodes is stepped-up to 50,000 volts AC in the rotary converters/transformers; the turbomachine generators produce 50,000 volts AC which is combined with the output of the rotary converters/transformers. An AC to DC converter is used to provide the DC required to energize the transmitter.

The cascaded solar thermionic/Brayton cycle system is shown in Figure 3-4.

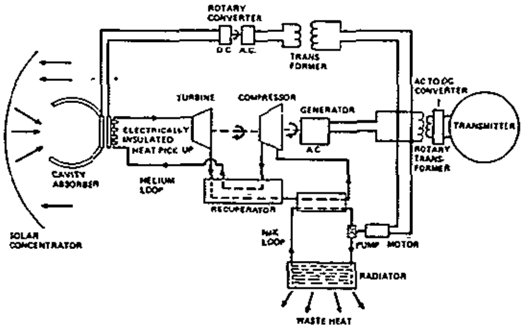

Fig. 3-4. Cascaded Solar Thermionic/Brayton Cycle System

3.6 SILICON PHOTOVOLTAIC (CONCEPT 5)

A photovoltaic, or solar, cell directly converts solar energy to electric power. Performance may be augmented, within certain limits, by concentrating solar energy upon the cell and/or by providing cooling.

Series strings of cells may be used to build to the 20,000 vdc (or 40,000 vdc), nominal, required for the microwave transmitter. Lower voltage arrays may be required if low orbit operation is required (such as for self-powered transfer) (Fig. 3-5).

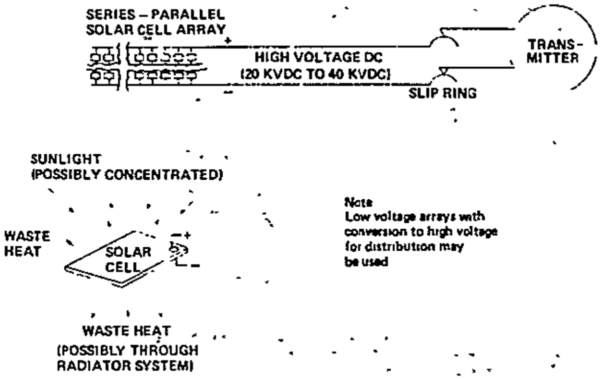

Fig. 3-5. Silicon Photovoltaic System

The solar cells employed in this concept are the "conventional" silicon type, except they are power economics dictates that they be only approximately one-half as thick as are currently used.

3.7 GALLIUM ARSENIDE PHOTOVOLTAIC (CONCEPT 6)

A photovoltaic, or solar, cell directly converts solar energy to electric power. Performance may be augmented, within certain limits, by concentrating solar energy upon the cell and/or by providing cooling.

Series strings of cells may be used to build to the 20,000 vdc (or 40,000 vdc), nominal, required for the microwave transmitter. Lower voltage arrays may be required if low orbit operation is required (such as for self-powered transfer) (Fig. 3-6).

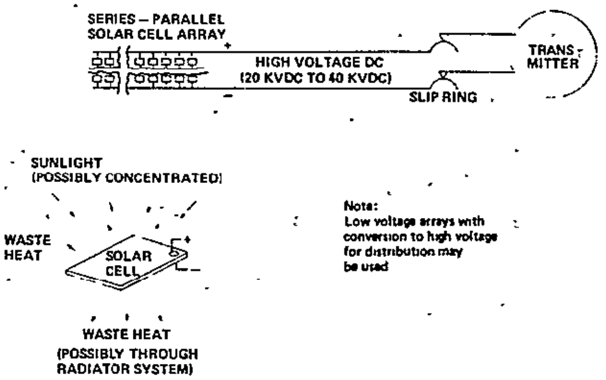

Fig. 3-6. Gallium Arsenide Photovoltaic System

The cells employed in this concept are the gallium aluminum arsenide/gallium arsenide type. This multilayer "heterojunction" cell has the apparent potential for high efficiency at elevated temperatures; it is also more radiation resistant.

3.8 NUCLEAR THERMIONIC (CONCEPT 7)

The energy source in this system is nuclear; a molten salt breeder reactor (MSBR) is used. The salt mixture contains both fissile fuel, the energy source, and fertile fuel, which breeds to become fuel for subsequent use. The salt mixture is circulated out of the reactor core through a heat exchanger which transfers energy to a sodium loop. The sodium loop is used since there is insufficient salt flow for the diode emitter area.

A small secondary salt flow is continuously passed through a fuel process system. This system removes the protactinium and wastes which would "poison" the reactor by excessive neutron capture. The fuel process system introduces fertile fuel and removes bred fuel. The MSBR is an unique breeder concept in that a single liquid fuel mixture contains both fissile and fertile fuels, and that processing of solid fuel elements is not required.

The diode collectors are cooled by a liquid metal radiator loop. The low voltage DC output of the collectors is stepped-up and converted to AC by rotary converters/transformers. An AC to DC converter is used to provide the DC necessary to energize the transmitter.

The nuclear thermionic system is shown in Figure 3-7.

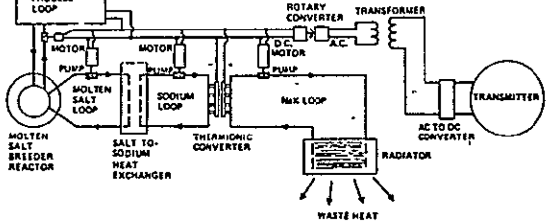

Fig. 3-7. Nuclear Thermionic System

3.9 NUCLEAR CLOSED BRAYTON CYCLE (CONCEPT 8)

The energy source in this system is nuclear; a molten salt breeder reactor (MSBR) is used. The salt mixture contains both fissile fuel, the energy source, and fertile fuel which breeds to become fuel for subsequent use. The salt mixture is circulated out of the reactor core through a heat exchanger which transfers energy to the helium loop of the Brayton turbomachines.

A small secondary salt flow is continuously passed through a fuel process system. This system removes the protactinium and wastes which would "poison" the reactor by excessive neutron capture. The fuel process system introduces fertile fuel and removes bred fuel. The MSBR is an unique breeder concept in that a single fuel mixture contains both fissile and fertile fuels, and that processing of solid fuel elements is not required.

The Brayton cycle turbomachine provides a rotating shaft output which drives the generators. Hot helium is expanded through the gas turbine, providing power to drive both the compressors and generators. The recuperator exchanges energy across the loop to increase efficiency. Waste heat is rejected through a gas-to-liquid heat exchanger to a liquid metal cooling loop; the liquid metal pumps use power drawn from the generators.

The 50,000 volt AC output of the generators is stepped-up to 382,000 volts in transformers; this high voltage facilitates on-board distribution. Step-down occurs in the rotary transformers. An AC to DC converter is used to provide the DC required to energize the transmitter.

The nuclear Brayton cycle system is shown in Figure 3-8.

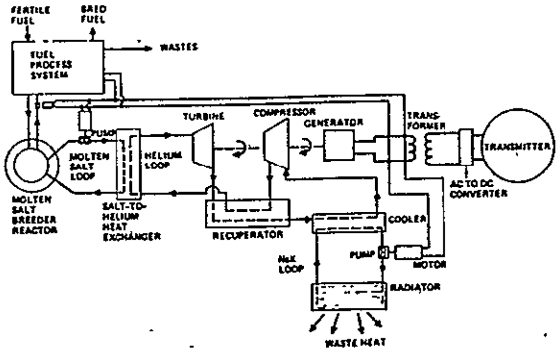

Fig. 3-8. Nuclear Thermionic System

3.10 POWER TRANSFER SYSTEM (CONCEPT 9)

In this concept one or more mirrors in geosynchronous orbit would reflect solar energy directly to Earth. Ground-based solar power plants would be augmented by this reflected energy, allowing night operation or increased output.

3.11 EMPHASIZED CONCEPTS

By the end of the initial phase of this study, it had become evident that further investigation of concepts 2, 4, 7 and 9 was inappropriate for the reasons given in Table 3-2.

Table 3-2. Evaluation of De-emphasized Systems

Concept	Reason for De-emphasis
2	More massive than Concept 1
4	No advantage over Concept 3
7	Extremely massive/not technically feasible
9	Extreme environmental impact

4.0 SUBSYSTEMS

4.1 MATERIALS

Many of the material requirements of the SPS will be satisfied by the use of aluminum, magnesium and titanium alloys. However, some subsystems contain components which operate at elevated temperatures. Selection of alloys for these SPS applications is based on the temperature range involved, as shown in Figure 4-1. The tungsten/rhenium and tantalum alloys are less well defined than the columbium and cobalt alloys.

The materials identified will be used for heat exchanger tubing (e.g., within solar cavity absorbers) and for manifolds, etc., in the radiator systems.

Note that the material strength shown in Figure 4-1 is the predicted 30-year creep rupture strength. Many SPS subsystems require long term confinement of pressurized gases or liquid at high temperatures, thus a fundamental problem is the long-term creep rupture at high temperatures.

Table 4-1 shows additional considerations in material selection, and alloys considered as option.

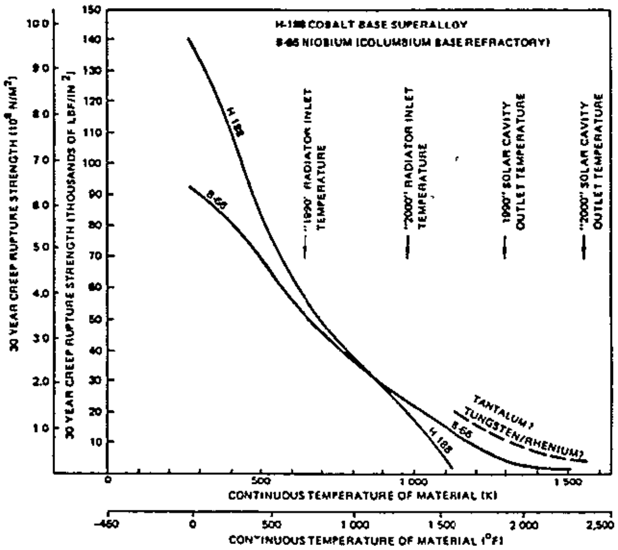

Fig. 4-1. Material Selection Approach

A trend of improvement of alloys for service above 1000K (1340°F) is shown in Figure 4-2. Iron, cobalt, columbium and nickel base systems were compared. A number of alloys having good strength properties were not considered due to their poor fabrication capabilities. While strength rupture capabilities of the nickel and cobalt base alloys have shown only a modest advance in the past 25 years, significant improvements in thermal fatigue, oxidation resistance, and stability characteristics have been achieved.

CONCLUSIONS:

1. Little or no improvement trend in the cobalt base alloys.
2. Nickel base alloys have been improving at the rate of approximately 3.4K (6.2°F) per year.

ALLOY SYSTEMS

STAINLESS STEEL
- AISI 316
- AISI 347

NICKEL BASE SUPERALLOYS
- INCONEL
- HASTELLOY X
- INCONEL X
- INCONEL 617

COBALT BASE SUPERALLOYS
- HS-25
- HA-188

REFRACTORY ALLOYS
- COLUMBIUM BASE – B-66

IRON BASE (HI TEMP)
- 19-9 DL
- A-286

Table 4-1. Material Considerations

DESIGN REQUIREMENT	IMPORTANT MATERIAL CHARACTERISTICS
SERVICE TEMPERATURE AND PRESSURE	• STRESS-RUPTURE STRENGTH
SERVICE LIFE	• METALLURGICAL STABILITY • SUBLIMATION EFFECTS ON STRESS-RUPTURE STRENGTH
SYSTEM SIZE	FABRICABILITY
ECONOMICS	• DENSITY • CHEMICAL COMPOSITION (COST & CRITICAL/STRATEGIC METAL CONTENT)

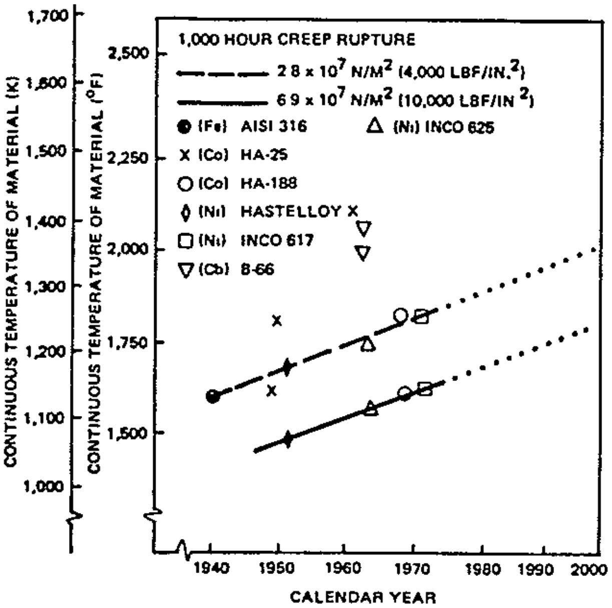

Fig. 4-2. *Material Technology Trend*

3. Introduction of a new alloy type, e.g., columbium-based B-66, can cause the most dramatic increase.

4.2 SOLAR CONCENTRATORS

4.2.1 High Concentration Ratio (Over 1000)

The solar power generating systems require large solar concentrators with low mass per unit area. Concentration ratios of one thousand or more are required. Highest optical efficiency would be obtained with a rigid paraboloid; yet the structure required to provide accurate form despite thermal and gravity loads, aging and assembly inaccuracies is estimated to have a mass of at least 2.0 kg/m^2 (0.41 lbm/ft^2). The baselined concentrator consists of a large number of individually steerable plastic film mirrors mounted on a relatively light framework. Active mirror control maintains focusing despite the disturbing forces mentioned above. Total concentrator mass for this type of system is estimated to be 0.29 kg/m^2 (0.059 lbm/ft^2).

The faceted concentrator is shown in Figure 4-3.

Figure 4-4 shows a typical reflective facet. Metallized plastic film (baseline is aluminized Kapton) is tensioned to form a plane surface. The support system consists of three edge members with bridles tensioned by springs. The inherent flat facet is fitted with a two-axis servo drive which causes the sunlight reflected by the facet to enter the aperture of the cavity absorber.

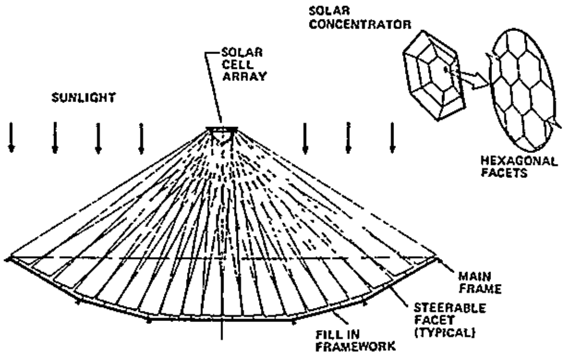

Fig. 4-3. Faceted Concentrator (Individual Steerable Facets Direct Solar Impages Onto Solar Array or Into Cavity Absorber)

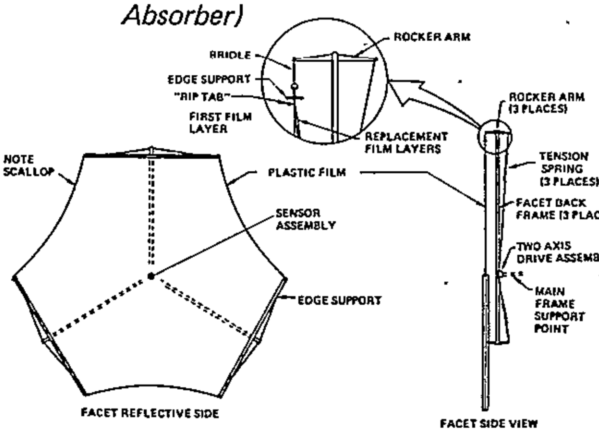

Fig. 4-4. Typical Reflective Facet

The number of facets used influences the achievable solar concentration. The most efficient concentrator would of course be a paraboloid, consisting, in effect, of an infinite number of very small reflectors. With reflectors of a finite size the image of each reflector also increases in size. Since the sun has an apparent width of 0.53°, the light reflected by the facets must spread at least at this angle. A total angle of one degree was used in this analysis. Perfect reflectivity was assumed.

Computer analysis of the multiple facet high concentration ratio solar concentrator are complete. Figure 4-5 identifies the variables in this analysis.

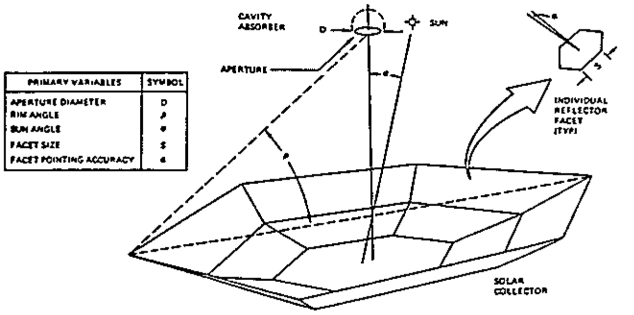

PRIMARY VARIABLES	SYMBOL
APERTURE DIAMETER	D
RIM ANGLE	ρ
SUN ANGLE	θ
FACET SIZE	s
FACET POINTING ACCURACY	ϵ

Fig. 4-5. Variables in Solar Concentrator Analysis

The computer program breaks down each hexagonal mirror (facet) into 96 triangular elements. Tests are made for shadowing and blockage by elements of other mirrors. The relationship of the reflection of each element to the cavity absorber aperture is determined.

Figure 4-6 shows the influence of geometric concentration ratio (ratio of projected concentrator area to aperture area) and facet count on the achieved concentration ratio (ratio of average flux through aperture to the ambient solar flux).

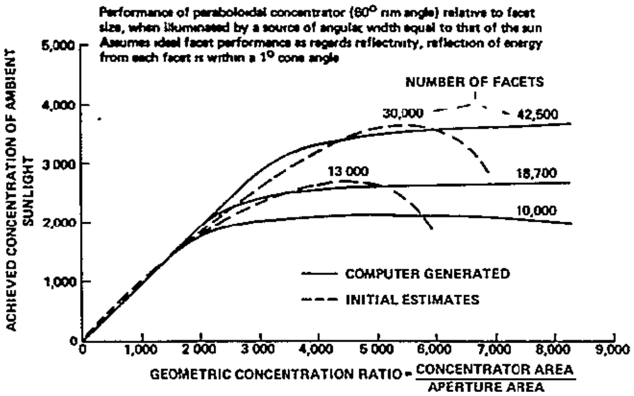

Fig. 4-6. Solar Concentrator Performance

Dashed lines in Figure 4-6 indicate the performance predictions made nearly two years ago by hand calculator.

The performance data in Figure 4-6 does not include the effects of facet reflectivity (typically 0.88 for thin Kapton films with first surface oxidized aluminum) or gaps between the facets (perhaps 2% of their area).

Figure 4-7 shows the influence on a reference solar concentrator of the sun being off-axis (not on the perpendicular to the center of the concentrator dish) and of non-specular reflectivity from the plastic film reflectors. The sun can be off-axis either through SPS attitude control errors, or when flying "perpendicular to the orbit plane" at other than the equinoxes. Only a perfect mirror would yield a perfectly specular (parallel ray) reflection. Plastic film mirrors tend to produce scatter of the reflected rays.

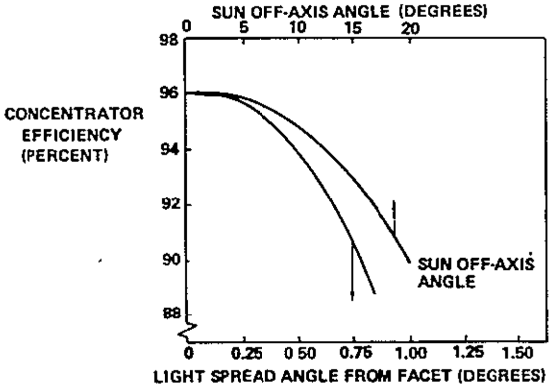

Fig. 4-7. Influences on Concentrator Efficiency (Solar Off-Axis Locations and Light Spread From Reflector Facets)

Figure 4-8 shows plastic film reflectivity data obtained by Boeing in a study for ERDA*. Testing was accomplished with a parallel beam (laser) light source. Masks of various diameters were used to assess the reflectivity versus cone angle. The cone angles shown do not include the 0.5° spread angle resulting from the angular width of the sun. The performance in Figure 4-6 includes the 0.5° solar width, and is for a light spread of 1° from the film. Kapton was baselined since some previous data (from project ABLE) indicated that Mylar was far more susceptible to radiation degradation.

The rim angle yielding maximum efficiency (96.8%) was 40°. The 30° angle was kept as the baseline since it provides 96.0% efficiency with shorter cavity support arms.

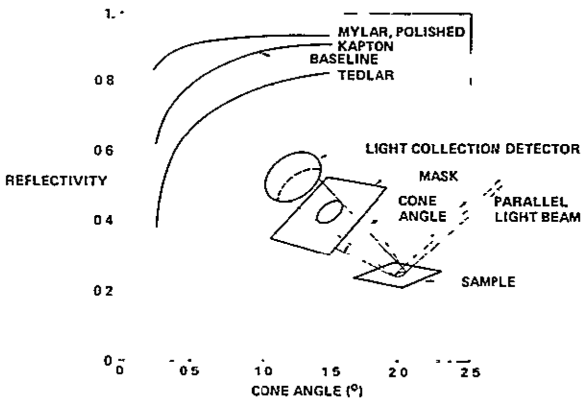

Fig. 4-8. Reflectivity Performance of Plastic Films

Solar Reflector Susceptibility to Degradation in the Geosynchronous Environment—Damage to the solar concentrators by meteoroid particles has been assessed. The optical characteristics of the concentrators will be impaired by the scouring effect of small particles and by penetration of larger particles. All particles striking the concentrators will damage an area far greater than the cross section of the particle. The damage will consist of penetration, cratering and spallation. For the purpose of this assessment the particle specific gravity was assumed to be 0.05, and the diameter of the area damaged to be twenty times the particle diameter.

---

*Contract E-(04-3)-IIII, "Central Receiver Solar Thermal Power System."

This latter figure may appear conservative but spall zones of this ratio of damage to particle diameter were encountered on the Apollo windows. Although there is a difference in materials, it is possible that the material chosen for the concentrators may become embrittled with age and suffer a similar type of damage to the Apollo windows.

To estimate the damage rate an omnidirectional meteoroid flux model was used. The model provides the cumulative flux corresponding to meteoroid mass, which was reduced to yield a total damaged area per unit area and time, using the criteria given previously. The estimated damage is 2.05 x 10^{-6} meter^2 per meter^2-day (2.05 x 10^{-6} foot^2 per foot^2-day).

This is a maximum figure since it assumes no two hits in the same place. Since this represents only 2.25% area damage in 30 years, meteoroids appear to pose no threat to the optical qualities of the solar concentrator.

However, the specular reflectance of metallized films may be significantly degraded by the proton flux. A possible explanation for this damage may be as follows: low energy protons are stopped within the metal layer and form hydrogen after gathering an electron. Hydrogen accumulation causes small "bubbles" to form in the metal, so that the surface is no longer planar. Some tests at relatively high exposure rates (to shorten the test period) were run by Boeing in connection with project ABLE (orbital reflectors for ground illumination). At a flux corresponding to 900 times the geosynchronous proton flux, reflectivity decreased to only 0.59 from an original value of 0.92 in a period of 3.25 days, which may correspond to only eight years of orbital exposure. There was some indication of a dose rate effect, so that the actual correspondence period may be much longer. However, it is evident that radiation damage may be quite severe for conventional metallized films.

On the other hand, the ECHO satellites flew in intense regions of the Van Allen radiation belts with apparently little degradation.

4.2.2 Low Concentration Ratio (Under 10)

Individual cell concentrators were investigated. A promising concentrator type is the "compound parabolic concentrator" (CPC) of Dr. Roland Winston of the Enrico Fermi Institude (1). In a three dimensional (as opposed to linear form) such concentrators have relatively little surface area compared to their solar capture area. They can accept sunlight at rather large off-axis angles. Figure 4-9, from (1) shows the basic geometric construction.

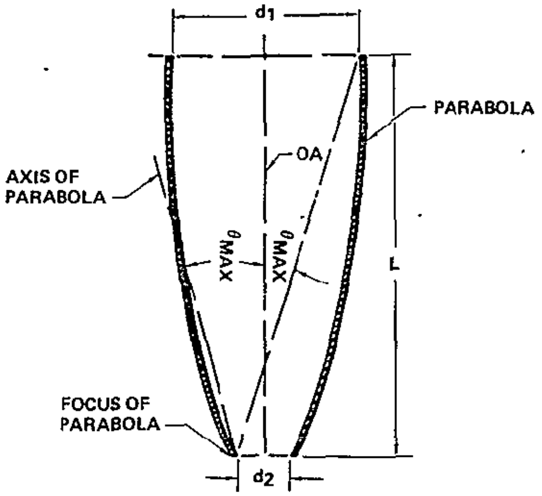

Fig. 4-9. Compound Parabolic Concentrator

The dashed line inclined to the left through angle θ is the axis of the parabola which forms the right hand surface. The left hand parabolic surface has as its axis a line inclined to the right by the angle θ; hence the term "compound parabolic." All rays are captured which are within θ of the central axis. Reflections are generally accomplished with shallow grazing angles which yield high reflectivity. Of course when the Sun is off axis a CPC will lose a small amount of output due to the inclination of its inlet aperture.

Due to the relatively small grazing angles involved a reflectivity factor of 90% was assumed. Off axis capability (θ_{max}) was related to solar concentration ratio (C) geometric) by:

$$C = \frac{1}{\sin^2 \theta_{max}} \qquad (1)$$

Derivation of optimum values of C to yield minimum power cost is defined in Section 5.

4.3 STRUCTURE

In the SPS, large electric currents have to be carried considerable distance. In order to minimize mass, members carrying these currents must also be primary structure and carry physical loads. Typical of these members are the truss beams connecting the solar concentrators to the solar absorbers. Ideal cross sections were derived to provide a minimum sum of beam mass and generator penalty.

A family of curves was derived for beams configured as shown in Figure 4-10. The spacing between the tubes, the tube diameters and thicknesses was varied, and mass per beam length plotted against beam length for given load. The dotted line is an estimate of the locus of minimum mass. However, since the tubes of the beam are designed to carry current and heat loss (I^2R) has to be dissipated, there is a minimum cross section of the beam capable of carrying both the current and the applied load. This is indicated in Figure 4-10 for a typical SPS truss.

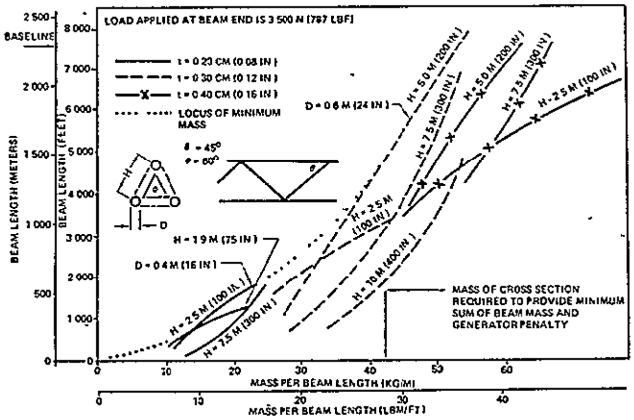

Fig. 4-10. Derivation of Ideal Beam Dimensions

Typical primary structure (trusses) of the SPS consists of three tubes equispaced as shown in Figure 4-11. The tubes are supported by diagonals which are hinged together. Since the tubes carry the primary satellite power the diagonals are insulated as shown. Prior to assembly in low earth orbit the diagonals are folded together tightly. On assembly the diagonals are unfolded and tubes 25.4M (83.3 ft.) long are inserted into the clamps at the ends of the diagonals. The sections of tube are welded together and to the clamps where they butt, and the snatch clamps are secured to the tubes.

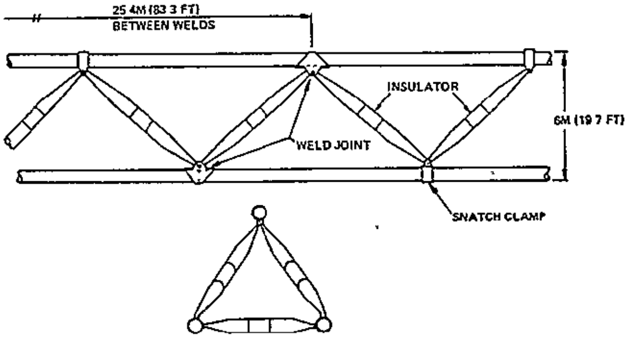

Fig 4-11. Typical Power Satellite Conducting · Primary Structure (Example, Size Varies)

4.4 CAVITY SOLAR ABSORBER

Solar heat flux from the solar concentrator is reflected into the cavity absorber. The cavity is a spherical structure with an aperture for receiving solar radiation as shown by Figure 4-12. (A cylindrical absorber is used for the thermionic SPS.)

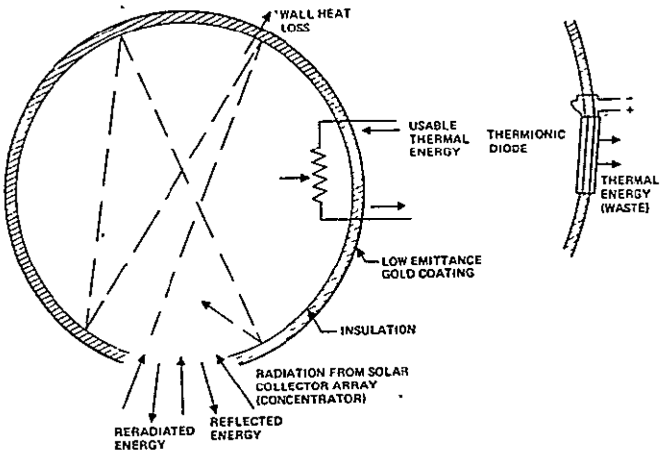

Fig. 4-12. Cavity Solar Absorber

Solar energy flux into a cavity absorber is for the most part absorbed into the walls. This is because multiple reflections must in general take place before reflection back out of the aperture can occur. Once absorbed, the energy is available for removal by the energy converter (Brayton cycle or thermionics). The hot walls radiate thermal energy back and forth between them; some of this energy escapes through the aperture. Insulation and a low emissivity exterior coating are used to limit energy loss through the walls.

Thermal energy loss by radiation is influenced by the emissivity of the surface and the fourth power of its absolute temperature. Thermal engine efficiency requires high cavity temperatures, therefore reradiation must be controlled if cavity efficiency is to be high. The loss by reradiation is a function of the cavity aperture area. All energy passing through the walls must eventually be reradiated from the cavity exterior. Therefore, a low emissivity coating (gold is baselined) is used. To provide a low exterior temperature, thermal insulation is provided.

The cavity interior insulation selected was "Multi-Foil," developed by the Thermo Electron Corporation, which consists of a number of layers of thin refractory metal foils spaced in vacuum by oxide particles. The oxide is selected on the basis of low thermal conductivity and foil compatibility. Multifoil provides a very high thermal impedance with minimum mass.

4.5 CONCENTRATOR/ABSORBER OPTIMIZATION

An optimization was conducted to find the values of primary solar concentrator and cavity absorber parameters which would (in combination) yield the minimum total mass for a given power removed from cavity at a given temperature. The optimization was conducted with the ISAIAH (Integrated Sensitivity and Interactions Analysis, Heuristic) program using a model as depicted in Figure 4-13.

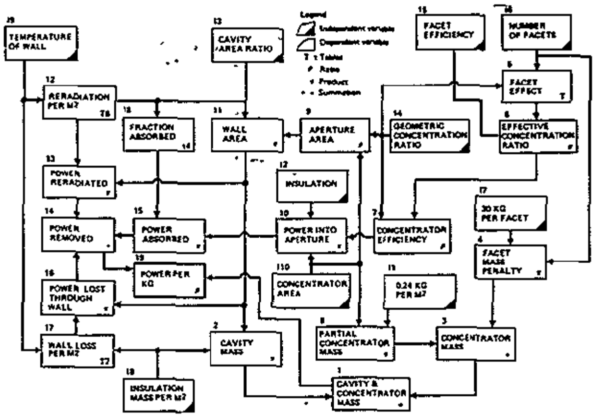

Fig. 4-13. Model for Concentrator/Absorber Optimization

The parameter to be optimized is number 19 "Power per kilogram"' The legend explains the types of parameters used; for example, parameter 17 is a table expressing the power loss per square meter of cavity wall as a function of wall temperature and the mass per square meter of insulation added to the wall. Parameter 14, the "power removed" is that which is available to do useful work. Parameter 1 is the total mass of the solar concentrator and the cavity absorber. Parameter 12, the reradiation per square meter of aperture area is based on an effective wall interior emissivity of 0.9. The solar concentrator performance determination uses the data shown in Figure 4-7. Parameters I3, I4, I6 and I8 were automatically varied to obtain minimum values of parameter 19 over a range of values of parameter I9.

Optimization results are given in Figure 4-14 for a concentrator area at 1.5 x 10^7 m^2 (1.61 x 10^8 ft^2). The power removed per unit mass is seen to decrease with increasing wall temperature. The optimum value for the geometric concentration ratio (GCR) increases with wall temperature. The GCR optimum is 2260 for the 1620K (2456° (2456°F) of the Brayton system and 2450 for the 1800K (2780°F) of the thermionic system.

Not shown in Figure 4-14 are optimum values for the number of reflector facets per concentrator. For the Brayton system the number is 16,800; for the thermionic, 17,500.

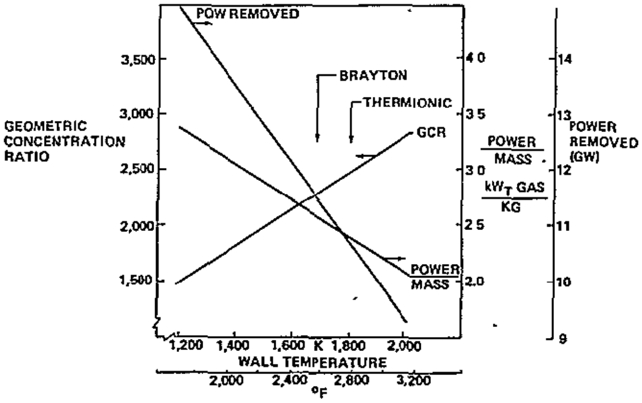

Fig. 4-14. Characteristics of Mass-Optimized Concentrator/Absorber Combinations

4.6 THERMIONICS

4.6.1 Background

This section was provided by the Thermo Electron Corporation (TECO):

Chronologically, improvements in thermionic energy conversion, as measured by the barrier index (collector work function plus inter-electrode plasma voltage losses), occurred first with the addition of small amounts of oxygen into the diodes, and subsequently with the use of tungsten oxide collectors. Currently, a number of other semi-conducting oxides are showing even better potential for thermionic loss reductions. In Figure 4-15, we see these losses correlated to thermionic efficiency and emitter temperature. For an emitter temperature of 1800K and a barrier index of 2.1, the thermal-to-electrical conversion efficiency is approximately 15 percent. Laboratory converters are being constructed that, for short generating periods, have demonstrated barrier indices as low as 1.9. From the historical development, and the

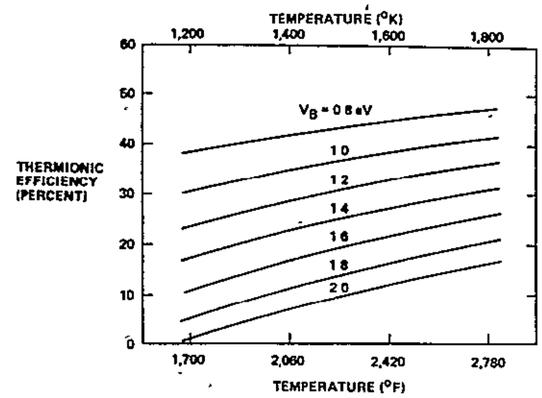

Fig. 4-15. Thermionic Efficiency Versus Emitter Temperature

current status of thermionic conversion, it is projected that the plasma arc drop will be sufficiently reduced to lower the barrier index to 1.8 by the year 1985 and to 1.6 by 1995. Such reductions represent gains in efficiency to 21 percent and 24 percent, respectively. Since silicon solar cells, presently about 13 percent efficient, can theoretically attain only 22 percent efficiency, and practically may never exceed 18 percent, these projected gains for thermionic converters are quite significant in their potential application to the SPS.

4.6.2 Converter Characteristics

The proper choice of operating conditions, materials, and design configuration is important in providing thermionic converters that are efficient, low in mass, and reliable for long periods of operation. High performance, stable output has, in fact, been maintained in a converter for over 40,000 hours, at which time, although the converter was still fully operational, the program was terminated. One mode of failure in a converter occurs when a monolayer of the emitter is evaporated onto a different material collector, thereby altering its properties. This evaporation limits the useful emitter materials and their operating temperatures unless similar materials are used for both emitter and collector. Although tungsten would provide the lowest vapor pressure emitter material, its availability is limited. Boeing has specified that Thermo Electron investigate the potential of molybdenum. If operated at 1800K (2780°F) for 30 years, molybdenum would dispense 0.6 mm (0.024 inch) of material onto the collector (Ref. 1). However, efficient radiation cooling of the collector requires a high collector temperature and, therefore, precludes the use of very low work function collector materials (to prohibit excessive electron back emission from collector to emitter). Consequently, molybdenum is found to be an attractive collector material as well, and emitter evaporation will therefore not affect the efficiency of the converter. To reduce weight and cost, nickel was chosen for the collector structure and radiator material. Deposition of molybdenum on the nickel electrode during converter operation will quickly produce a molybdenum coated collector for essentially the entire lifetime of the converter. Constant and uniform close spacing of the electrodes should be maintained because of the straight-line deposition from emitter to collector. Laboratory converters are usually fitted with cesium reservoirs to provide cesium vapor in order to reduce electrode surface work functions, as well as to provide space charge neutralization in the interelectrode region. The effect of cesium on molybdenum electrodes is shown in Figure 4-16 where T is the electrode temperature and T_R the reservoir temperature of cesium.

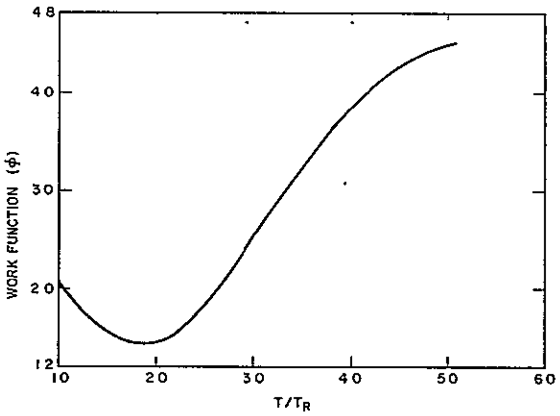

Fig. 4-16. Molybdenum Work Function Plot

Determination of the output characteristics of a converter is detailed in Ref. 2. Mathematically the efficiency, η, is related to the output power density, P, and the heat supply rate, q, by

$$\eta = \frac{SP}{q} \qquad (1)$$

where S is the active area of the planar emitter and collector. The output power density is a function of converter current, J, and voltage

$$P = J(V - V_a) \qquad (2)$$

where V is the output voltage of the electrodes and V_a the voltage drop across the electrical leads connecting the converter to the load. The heat supply rate can be expressed as

$$q = q_{EC} - q_{CE} + q_R + q_k + q_a - \frac{q_d}{2} \qquad (3)$$

The emitter electron cooling rate is

$$q_{EC} = \frac{SJ_{EC}}{e} (\psi_m - \mu_E + 2kT_E) \qquad (4)$$

where ψ_m is the maximum value of the interelectrode motive, μ_E the Fermi energy of the emitter and S the electrode area. The emitter electron heating rate is

$$q_{CE} = \frac{SJ_{CE}}{e} (\psi_m - \mu_E + 2kT_C) \qquad (5)$$

The thermal radiation is

$$q_R = S\sigma\epsilon \, (T_E^4 - T_C^4) \qquad (6)$$

The heat conduction by structural components and cesium vapor is .

$$q_k = g_k \, (T_E - T_C) \qquad (7)$$

where g_k is the associated thermal conductance. The heat conduction of the leads is

$$q_a = k_a \frac{S_a}{l_a} (T_E - T_C) \qquad (8)$$

where k_a is the lead thermal conductivity, and S_a and l_a refer to the lead cross-sectional area and length, respectively. The Joulean heat loss in the leads is

$$1/2 \, q_d = 1/2 \, SJV_a = 1/2 \, S^2 J^2 \rho_a \frac{l_a}{S_a} \qquad (9)$$

where ρ_a is the electrical resistivity of the leads.

Equations 1 through 9 were computerized, and conversion efficiencies and cesium plasma losses, V_d, determined for operational thermionic converters. The results for the pertinent range of emitter temperatures analyzed are shown in Figure 4-17. At the suggested 1800 K (2780°F) upper temperature limit for molybdenum, the power output is slightly above 8 W/cm^2 (51.6 W/inch^2).

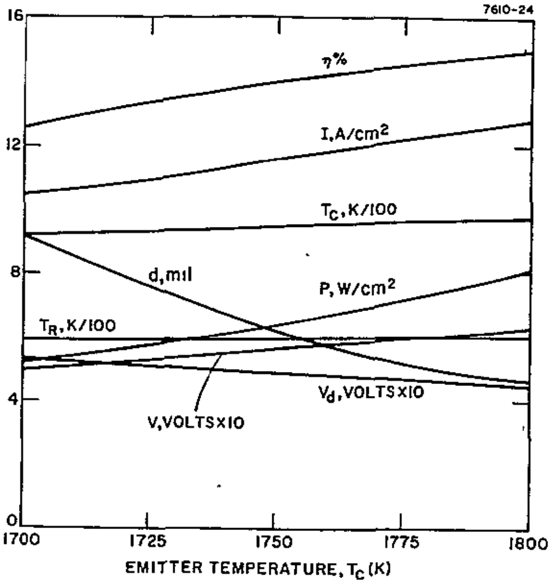

Fig. 4-17. Thermionic Diode Characteristics as a Function of Emitter Temperature for a Molybdenum Emitter and a Nickel (Molybdenum Coated) Collector

These computational methods were also applied to predicting future converter performance. Because of the high collector temperature required for effective radiative cooling in space, improvements in converter performance will not occur by reducing collector work functions, since performance degrading back electron emission would be increased. Major advances can be made only by reducing the cesium plasma losses. Figure 4-18 presents the increases in power output and efficiency realizable with plasma loss reductions of 0.2 and 0.3 volts from those existing at present. Based on past performance improvements, the lower of these reductions should be attained before 1985, while the higher reduction is expected by 1995. Accordingly, power outputs are expected to reach 12 W/cm^2 (77.4 W/inch^2), with an efficiency of 24 percent.

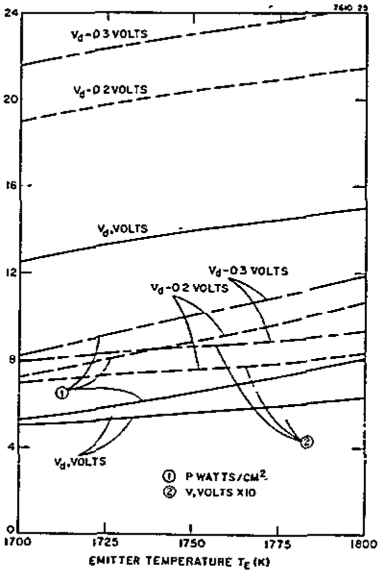

Fig. 4-18. Increase in Efficiency and Output Voltage with Decreasing Plasma Drop for Constant I of 1290 A

Methods to produce such lower plasma losses are being developed currently and include the potential use of new electrode materials; e.g., hexaborides and other semiconductors, which require lower interelectrode cesium densities, pulsed triodes using rare gases for ion production and close-spaced diodes with reduced space charge effects.

4.6.3 Radiator

Design of a passive radiation cooling system for space thermionic energy converters is one of the most important tasks of this study. For electric power production, P, with a solar heat conversion efficiency, η, the heat flux rejected, q_o, is given by

$$q_o = P\left(\frac{1}{\eta} - 1\right) \qquad (10)$$

We assume that this heat flux can be radiated into space from a surface of area A_s at uniform temperature T_s and emissivity ϵ

$$A_s \simeq \frac{P}{\sigma \epsilon T_s^4}\left(\frac{1}{\eta} - 1\right) \qquad (11)$$

where σ is the Stefan-Boltzmann constant. Figure 4-19 shows the dependence of A_s on converter efficiency and collector temperature for a nominal electric output of 4 GW, a radiator temperature 90 percent that of the collector, and a radiator emissivity of 0.9. A 24 percent electrically efficient converter with a collector at 1000 K (1340°F) requires 3.8×10^5 m^2 (4.09×10^6 ft^2) of surface area for radiation cooling.

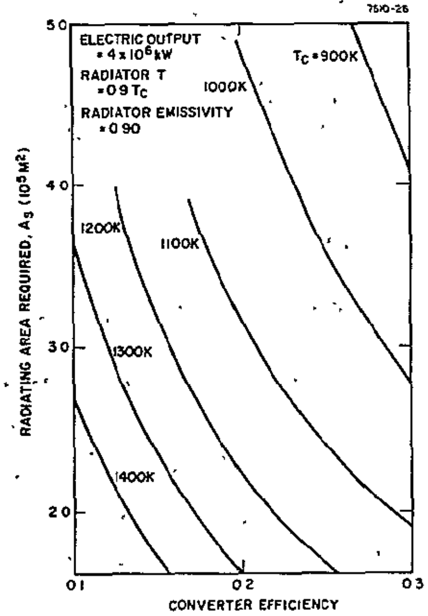

Fig. 4-19. Heat Rejection as a Function of Converter Efficiency (Modified From Ref. 8)

According to our previous calculations, the anticipated power density at this efficiency is 12 W/cm^2 (77.4 W/in^2). For the geometrical tolerances required in a converter, the practical size for the electrodes is expected to be 100 cm^2 (15.5 inch^2) per converter with an output, therefore, of 1200 W. Such dimensions will require approximately 3.4 million converters to generate 4 GW of electrical power. Consequently, the required radiating area per converter is 0.1 m^2 (1.076 ft^2).

Since the collector material is made of nickel, it would be advantageous to have an integral radiator assembly made of similar material. Although the emissivity of nickel is low, that of oxidized nickel at 900 K (1160°F) is an attractive 0.9. Consequently, the radiating nickel surface would be oxidized to enhance emissivity.

The simplest method for radiator design would be to project solid cooling fins, in the form of a cup, away from the circular edge of the collector out into space. These cups would be hexagonal so that radiators could be fitted into a "honeycomb" arrangement. The equivalent emissivity, ϵ_{eq}, for heat loss, q_o, from a cylindrical cavity is given by (Ref. 3).

$$\epsilon_{eq} = \frac{q_o}{\sigma T_s^4 A_C} \qquad (12)$$

and is not appreciably enhanced when high emissivity, ϵ, material is used, as seen from the numerical values presented in Table 4-2 where A_C is the area of the collector, L/D, on which q_o depends, is the length-to-diameter ratio of the cylinder.

Table 4-2. Equivalent Emissivity.

L/D	ϵ = 0.9	0.75	0.5
0.25	0.9434	0.8491	0.6569
0.5	0.9648	0.8948	0.7424
1.0	0.9720	0.9229	0.8084
2.0	0.9746	0.9308	0.8331

Any small increase in effective emissivity from a cavity radiator would be more than offset by the greater system mass required. These results, therefore, suggest a flat radiator coplanar with the collector. The heat that needs to be rejected by a 24 percent efficient converter is 3800 W of which only 510 W will be radiated away by the collector surface. Consequently, 3290 W must be transported by the cooling fins. Considering a thin fin with a maximum area of contact between the collector and fin of 20 cm^2 (3.06 in^2), the associated temperature gradient at that boundary for the thermal conductivity of nickel at 0.55 W/cm-C (see Figure 4-20) is

$$\frac{dT}{dx} = \frac{q_{fins}}{kA} = \frac{3290}{(0.55)(20)} = 299 \text{ C/cm} \quad (13),$$

which results in an extremely nonuniform temperature of the fin surface (i.e., poor fin efficiency) and, therefore, would require too massive a radiator system.

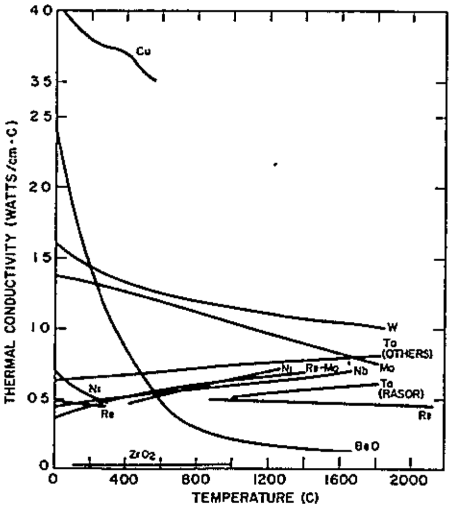

Fig. 4-20. Thermal Conductivity Data

The alternative approach is to employ a heat-pipe concept to provide a uniform radiator temperature and, thereby, achieve uniform heat rejection temperature and high fin efficiency. A number of configurations were considered; the one judged best is shown in cross section on Figure 4-21. Sizing of the emitter is determined by loss of material from thermal vaporization over its thirty-year lifetime, minimization of resistive power losses, and weight considerations; sizing of the collector depends on resistive and weight considerations. Figure 4-22 presents an isometric cutaway view of this design showing the main features of the converter.

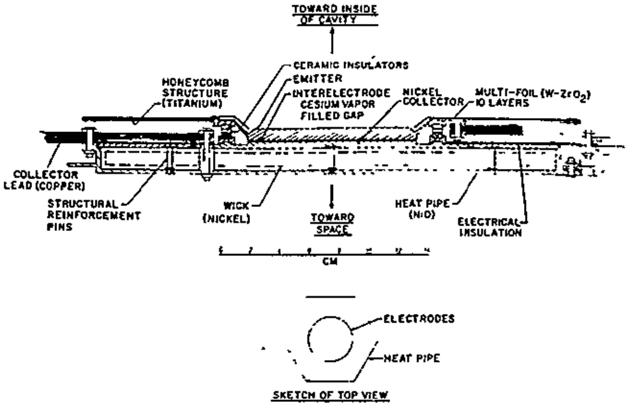

Fig. 4-21. SPS Thermionic Converter Design

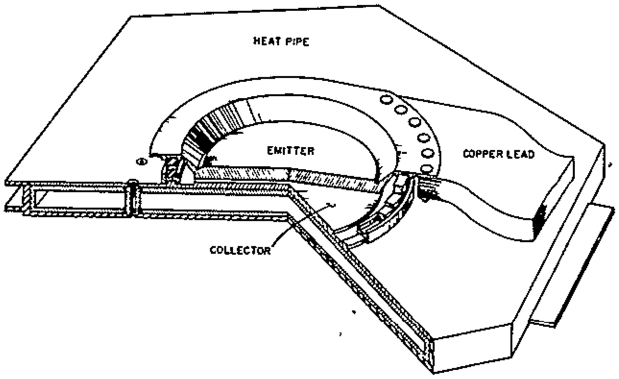

Fig. 4-22. Isometric Cutaway of SPS Thermionic Converter

In designing the heat pipe, four working fluids were analyzed; mercury, cesium, potassium, and sodium. Following the methods outlined in Ref. 4, the figure of merit, F, was calculated for each at a working temperature of 900 K (1160°F)

$$F = \frac{\rho_l \sigma_l L}{\mu_l} \quad (14)$$

where ρ_l is the liquid density, σ_l the surface tension, L the heat of vaporization, and μ_l the viscosity. The results shown in Table 4-3 indicate

Table 4-3. Heat Pipe Figure of Merit

	F
Mercury	1.317 (10^5)
Cesium	2.097 (10^5)
Potassium	7.954 (10^5)
Sodium	2.247 (10^6)

sodium as the best fluid. In the absence of oxygen this element is compatible with a structure made of nickel. The heat transfer of sodium at the limiting sonic velocity flow

$$q_s \sim 0.474\, L\, (\rho_v P_v)^{1/2} \qquad (15)$$

where ρ_v is the vapor density, and P_v its pressure, was found to be more than sufficient at 3.07 kW/cm^2 (19.80 kW/in^2).

Sizing of the wick was determined by equating the maximum capillary head

$$\Delta p_c = \frac{2\sigma_l}{\gamma_l} \qquad (16)$$

to the pressure drop in the liquid

$$\Delta p_l = \frac{\mu_l}{\rho_l L}\, q_o\, \frac{l_{eff}}{A_W K} \qquad (17)$$

where γ_l = 3.18 cm (10^{-3}) (for a mesh size of 400), q_o is the required heat transfer, l_{eff} is effective path length, A_W is the area of wick required, and K is determined from the Blake Koseny equation

$$K = \frac{d_W^2\,(1 - E)^3}{66.6\,E^2} \qquad (18)$$

where E is the volume fraction of solid phase of the wick (0.314), and d_W is the wick's wire diameter (0.025 mm). Solving equations 16 and 17 for A_W provides the required wick areas shown in Table 4-4.

Table 4-4. Heat Pipe Wick Dimensions

Fluid	A_W (cm^2)	t (cm)
Cesium	85.4	2.3
Potassium	22.5	0.6
Sodium	80.3	0.2

Also presented in this table is the wick thickness, t, which is determined from the wick area and circumference of the collector. Solium is seen to be the optimum working fluid.

Design of the heat pipe nickel housing was based on minimizing the mass for the total radiating area required (Figure 4-19) and taking into account the structural strength necessary to contain the heated sodium vapor. Because of the large mass penalty which exists if such a structure must tolerate atmospheric pressure loading, it was decided to include a pinch-off port in the heat pipe to allow equalization of pressure during assembly and launch. Once in orbit the heat pipes are charged with the required amount of sodium, and the opening is pinched off. Under this mode of assembly the heat pipe internal pressure is approximately 0.89N/cm^2 (1.29 psi). A wall thickness of 1 mm (0.0254 in) was judged sufficient to tolerate this loading. Thin-plate analyses indicated that maximum deflection for a 1 mm thick wall was 0.7 cm (1.78 in). To reduce such distortion, small, light struts were included, as shown in Figure 4-21.

Although the electrodes are circular in design, the heat pipe has been configured hexagonally in order to optimize the use of the satellite's surface area.

A thin, ten-layer, covering of MULTI-FOIL thermal insulation (Figure 4-23) protects both the electrical busbars, as well as the heat pipe from direct solar radiation. MULTI-FOIL insulation, developed at Thermo Electron Corporation, consists of a number of layers of thin refractory metal foils spaced in a vacuum by oxide particles. The oxide is selected on the basis of low thermal conductivity and foil compatibility, and the particles are optimized with regard to size and coating

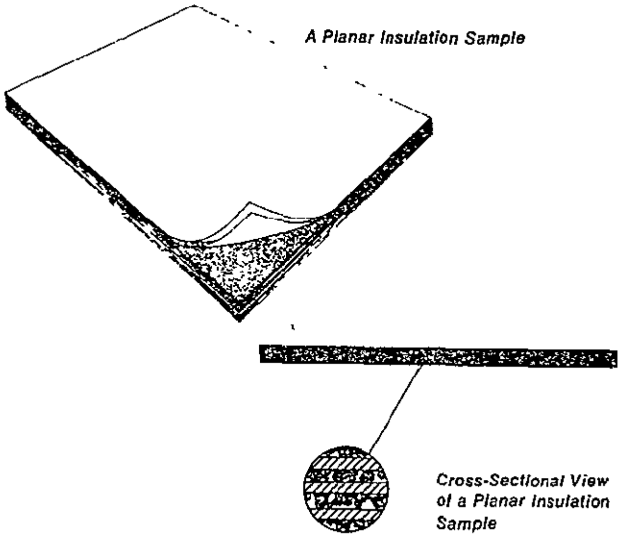

Fig. 4-23 Multifoil Thermal Insulation

density to minimize thermal transport. Consequently, this MULTI-FOIL provides an ultrahigh impedance to thermal transport, with minimum mass (Figure 4-24). For the design shown in Figure 4-21, ten layers of 1 mil-thick tungsten foil separated by ZrO_2 particles were considered adequate. As can be seen in Figure 4-25, the layers provide substantial insulation capability. The total thickness of such insulation is 1.2 mm (0.03 in.) with a mass of only 0.25 gm per cm^2 (0.51 lbm/ft^2), or approximately 230 gm per converter. Heat transfer through the 900 K (1160°F) temperature differential between the incident radiation (T_1 = 1800 K) (3140°F) and the heat pipe (T_o = 900 K) (1160°F) is (Ref. 5).

$$q_{MF} = \frac{1.06(10^{-12})\,(T_1^4 - T_o^4)}{0.778N + 1.11(10^{-2})N^2} = 1.2\,W/cm^2 \qquad (19)$$

where N is the number of MULTI-FOIL layers and T is in degrees Kelvin. This additional heat flow can be radiated out by the heat pipe.

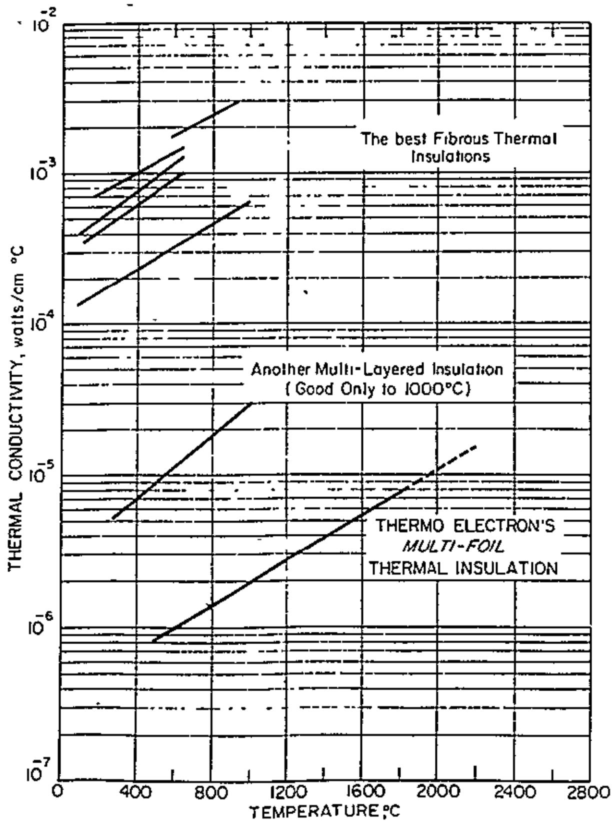

Fig. 4-24. Thermal Conductivity Comparison

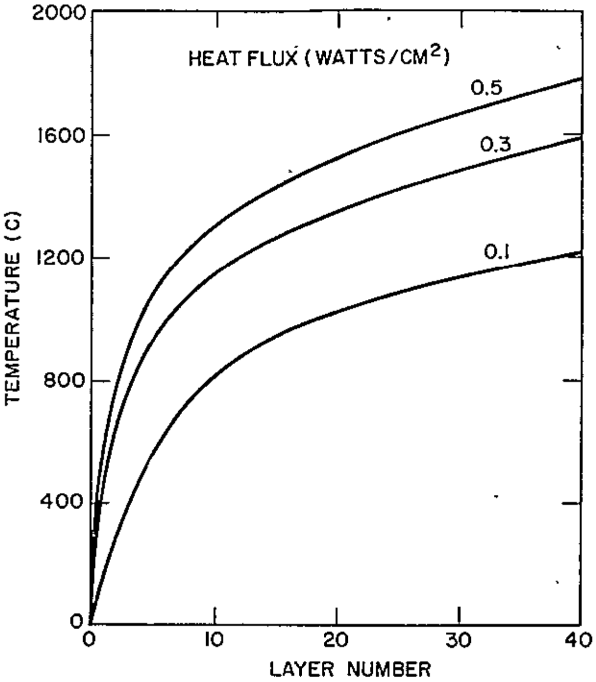

Fig. 4-25. Multifoil Thermal Insulation Temperature Profile for Brush-Coated ThO_2 on Tungsten

4.6.4 Busbar Design

In determining resistive power losses both the converter electrodes and interconnecting leads must be considered. The least losses result if currents are minimized and voltages maximized; i.e., if the thermionic converters are connected in series. At high temperatures, however, electrical insulation of the leads becomes a problem. In the design, shown in Figure 4-21, the temperature of the electrical insulation never need exceed 1000 K, because of a thin metallic (molybdenum) thermally insulating heat choke between the hot emitter and interconverter lead. The design of this choke is determined by optimizing Equation 1 with respect to S_a/l_a which yields (see Ref. 2) the best ratio for

$$\frac{q_a}{q_d} = \frac{1}{\eta} - \frac{1}{2} \sim \frac{1}{\eta} \qquad (20)$$

or

$$k\eta\,(\Delta T) \sim I^2 \rho \left(\frac{I_a}{S_a}\right)^2 \qquad (21)$$

For k_{Mo} ~ 1 W/cm-K (Figure 10), ΔT = 800 K, η = 0.24, $\rho_{Mo} = 3(10^{-5})\ \Omega$ - cm (Figure 4-26), and I = 1290 A in equation 21

$$\frac{l_a}{S_a} \doteq 2.0\ \frac{1}{cm}, \qquad (22)$$

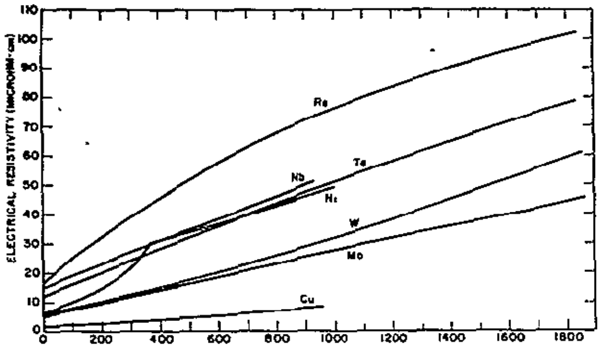

Fig. 4-26. Electrical Resistivity of Metals

which for the electrode area of 100 cm^2 results in a choke thickness, t

$$t = 1.4\ (10^{-2})\ l_a\ . \qquad (23)$$

For a lead length of 1.5 cm the thickness will be 0.02 cm.

The fundamental satellite power unit will consist of a string of 161 converters connected in series (Ref. 6). In line with Boeing's design of a 20-m square panel this unit will form three horizontal rows approximately 18-m in width, as shown in Figure 4-27, leaving a 1-m wide strip on either side for the tapered busbars connecting these converter strings. Twenty-one such units, positioned vertically as shown, would cover the 20-m square panel.

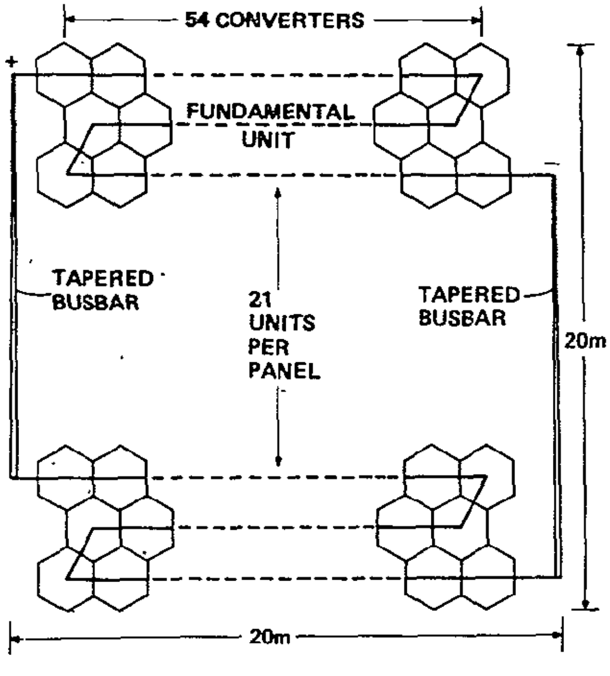

Fig. 4-27 SPS Electrical Panel Design

Maximum output voltage, anticipated for the year 1995, would not exceed 150 V which is sufficiently low to prevent electrical insulation problems at the maximum busbar temperature of 1000 K. Furthermore, operation in this electrical configuration will limit the current through any converter to 1290 A.

For the converter design shown in Figure 4-21, the cross-sectional dimensions of the leads connecting converters are 0.7 cm thick x 15 cm wide. Solid multiple-strand copper leads were compared to sodium filled 0.1-cm thick stainless steel leads with respect to their resistance-to-weight ratio. These ratios were 6.1 (10^{-9}) Ω/gm and 2.9 (10^{-7}) Ω/gm, respectively. Clearly copper is the better lead material.

The busbar resistance per converter was calculated by summing the individual contributions of the electrodes and leads.

$$\text{R/converter} = \left(\rho\ \frac{l_a}{S_a}\right)_{\text{lead}} + \left(\rho\ \frac{l_a}{S_a}\right)_{\text{collector}} + \left(\rho\ \frac{l_a}{S_a}\right)_{\text{emitter}} + \left(\rho\ \frac{l_a}{S_a}\right)_{\text{heat choke}}$$

$$= 1.0\,(10^{-4})\ \Omega \qquad (24)$$

By flashing copper on the molybdenum emitters and then fusion brazing on the copper leads, contact resistive losses can be minimized and, therefore, have been neglected in this analysis. Based on the foregoing resistance calculation, the voltage loss per converter with 1290 A current is 0.13 V which represents a 14 percent loss in power for the expected 0.93 V output per converter in 1995. In summary, a panel will deliver the following output:

I panel = 1290 x 21 = 27090 A
V panel = 161 x 0.93 x 0.86 = 129 V
P panel = I panel x V panel = 3.5 MW

Assuming one converter fails, the maximum power loss is 5 percent of the panel output or, for a 4 GW module, 0.004 percent of its output. If, however, converter failure occurs from an internal electrical short, only the output of a single converter is lost to the panel.

4.6.5 Weight Analysis

One of the most important characteristics of the SSPS that needs to be estimated at the earliest date is its total mass. This section of the analyses presents the masses of the various components of the design in Figure 4-21.

The converter emitter consists of a circular 100 cm^2 molybdenum flat plate which is 5 mm thick, so that it can withstand the 1.2 mm loss of material (0.6 mm from each face) during the desired 30-year lifetime, and retain a reasonable electric conductivity. The complementary collector has similar dimensions. Cesium is permanently introduced into the interelectrode cavity at the beginning of operation. Any small loss of this element during the operating lifetime of the collector can be replaced with cesium-graphite pockets in the collector. The total weight of the electrodes is 950 gm per converter or for a 1033 W net power output, 0.92 kg per kW_e. In Table 4-5, the sodium-filled heat pipe is estimated to have the following mass for a 1 mm-thick outer casing:

Table 4-5. Mass of Heat Pipe Components

Nickel Casing	0.85 kg
Nickel Wick	1.53 kg
Sodium	0.29 kg
Total	2.67 kg

or for the approximate 0.1 m^2 heat pipe radiating surface area, 26.7 kg per m^2. The mass of ten layers of 1 mil-thick MULTI-FOIL insulation is a negligible 0.25 kg per m^2. The masses for the rotary converters and for the solar concentrators plus frame and support arms has been calculated by Boeing to be 0.4 kg per kW_e and 0.3 kg per kW_T, respectively (Ref. 7).

The mass of each of the 15-cm wide, 7-mm thick, 15.2-cm long copper leads connecting the converters, as shown in Figure 4-21, is approximately 1.42 kg, or .84 kg per converter, which means 2.75 kg per kW_e. Table 4-6 summarizes these masses, and relates them all to electrical power output. The masses of the busbars connecting the fundamental 161 converter units to each other and the panels to the rotary converters have not been estimated.

Table 4-6. Mass of Converter Assembly

	Mass per Converter	Mass per Net kW_e
Converter Electrodes	0.97 kg	0.92 kg
Heat Pipe Radiator	2.67	2.59
MULTI-FOIL Insulation	0.023	0.024
Copper Leads	2.84	2.75
Total	6.48	6 28

4.6.6 Conclusions

The major results of this study are:

1) Planar molybdenum-nickel thermionic energy converters with 5 mm-thick electrodes can be operated at emitter temperatures of 1800 K and be expected to provide electrical efficiencies of 21 and 24 percent, respectively, by the years 1985 and 1995.

2) The converter design judged best has electrodes 100 cm^2 in area and a gross output of 1200 W in 1955 and 1290 A and 0.93 V. Resistive power losses through the electrodes and interconverter leads will reduce the gross power 14 percent for a net output of 1032 W per converter.

3) The panel design judged best to minimize busbar resistive power loss consists of 3381 converters in twenty-one 161-series strings. Net power output from such a panel is 3.5 MW. Copper interconverter leads were found superior to sodium-filled stainless steel. The requirements of busbars connecting the modules to the rotary converters were not considered. Such leads should be tapered to carry a maximum of 27,090 A per panel. The mass of these busbars could be substantially reduced by connecting, say, two converter strings (i.e., 322 converters) in a panel in series, thereby doubling the output voltage to 258 V and reducing the maximum current by one-half to 13,545 A. The ability of electrical insulation to withstand this higher voltage at 1000 K must be investigated. For the 161-converter unit, a failure in operation of one converter causes a maximum loss in power of 5 percent of the panel output, or 0.004 percent from a 4 GW module. The reliability of operation over a 30-year period would be increased by connecting all converters in parallel as well as series. Such a configuration would, however, substantially increase the mass of the leads.

4) A simple solid radiator system is insufficient to reject the required 3.8 kW of heat from each converter. Hexagonally shaped, sodium-filled fin heat pipes with reinforced 1 mm-thick nickel casing are adequate. In order to reduce mass requirements, these heat pipes must be open to the atmosphere during satellite launch, and subsequently filled with sodium and sealed in orbit. The NiO heat-radiating surface per converter is 0.1 m^2 in area.

5) MULTI-FOIL thermal insulation is excellent for shielding the electrical leads and heat pipes from the intracavity solar flux. The mass of such insulation is negligible with respect to the masses of other converter components.

6) The total mass per converter, comprised of the emitter and collector, the heat pipe radiator, thermal insulation, and copper leads is 6.48 kg, or 6.28 kg per kW_e net electrical output power. Dominant, and approximately equal, contributions come from the heat pipe and the leads at 2.67 kg and 2.84 kg, respectively. Complete parallel, as well as series, converter electrical connections, to enhance operational reliability, would substantially increase lead mass. More extensive analyses may indicate that the 1-mm casing thickness of the heat pipe and, consequently, its mass can be reduced.

It must be emphasized that the results of this brief study are intended to furnish sufficient data for evaluating the possibility of using thermionic energy conversion in Satellite Solar Power Stations. Additional analyses are necessary to provide detailed converter and heat pipe designs, determine interunit busbar configurations and masses, establish tradeoffs between operational reliability and busbar mass penalties, and identify constructional problems for on-earth or in-orbit converter, heat pipe, and panel assembly.

REFERENCES

1) R. F. Honig and D. A. Kramer, *Vapor Pressure Data for the Solid and Liquid Elements*, RCA Laboratories Report PTR-2720, April 21, 1969.

2) G. N. Hatsopoulos and E. P. Gyftopoulos, *Thermionic Energy Conversion—Vol I: Processes and Devices*, The MIT Press, Cambridge (1973).

3) E. M. Sparrow, L. V. Albers and E. R. G. Eckert, "Thermal Radiation Characteristics of Cylindrical Enclosures," ASME, *Journal of Heat Transfer*, 61-SA-23 (1961).

4) P. D. Dunn and D. A. Reay, *Heat Pipes*, Pergamon Press (1976).

F. N. Huffman, *Preliminary Design Review Document. Application of MULTI-FOIL Insulation to the Brayton Isotope Power System and Conceptual Design of MULTI-FOIL Insulation for the Flight System*, P-399625, Thermo Electron Corporation, June 11, 1976.

5) D. L. Gregory, Private Communication, October 25, 1976.

6) D. L. Gregory, *Space-Based Power Conversion and Power Relay Systems Study*, Fourth Monthly Progress Report, NAS8-31628, Boeing Aerospace Company, November 14, 1975.

7) D. L. Gregory, *Space-Based Power Conversion and Power Relay Systems: Preliminary Analysis of Alternate Systems*, Final Performance Review, NAS-31628, Boeing Aerospace Company, April 14, 1976.

4.7 SOLAR CELLS

4.7.1 Requirements

The challenges imposed on solar cells by the SPS concept include:

1) The cells must be light, i.e., thin. Current practice in spacecraft arrays is the use of cells having a thickness of 250 μM to 500 μM (10 mils to 20 mils). SPS studies have focused on cells of 100 μM (4 mils), or thinner.

2) The cells must be radiation resistant. Electrons and low energy protons trapped by the Earth's magnetic field tend to cause a steady deterioration. High energy protons associated with solar flares occur aperiodically and may cause additional damage. Cell damage is manifested by a reduction in cell efficiency. Cell radiation protection is usually provided in front (the sun side) by cover glasses; backside protection is by the cell substrate (mounting system). Thin solar cells are usually less radiation resistant than thicker

cells. Providing thick cover glass for radiation protection of course conflicts with (1).

3) The cells must be efficient, since the SPS area required is inversely proportional to the cell efficiency. Thin cells tend to be less efficient than thick cells. A good temperature coefficient is also to be desired, i.e., the efficiency should not fall off rapidly as cell temperature is increased.

4) The cells (and the completed array of cells, substrate, connections, etc.) must be low in cost. Today's array costs are far too high for the SPS.

These requirements are seen to be interactive.

The requirements are also somewhat dependent on the configuration of the SPS. High solar concentration ratios decrease the cell area, reducing the array costs and allowing thicker cover glass to be used without a mass increase (since reducing cell area also reduces cover glass area). However, higher concentration ratios tend to increase the cell temperature, hence a good temperature coefficient is required to keep efficiency high.

4.7.2 Cell Performance Prediction

4.7.2.1 Efficiency

Cell performance to be available in the initial SPS operating period was obtained by projection of the historical trend in efficiency improvement. This historical trend was researched back to 1957. Performances used were generally those of cells which could be purchased, not merely performances quoted in Photovoltaic Specialists Conferences or in press releases. Projection of the trend from 1957 to 1976 into the future resulted in the performances shown in Figure 4-28.

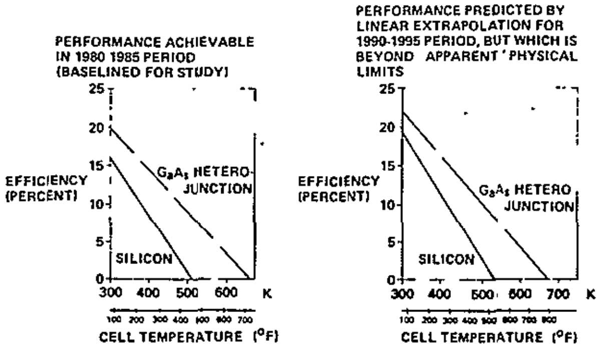

Fig. 4-28. Solar Cell Performance Predictions

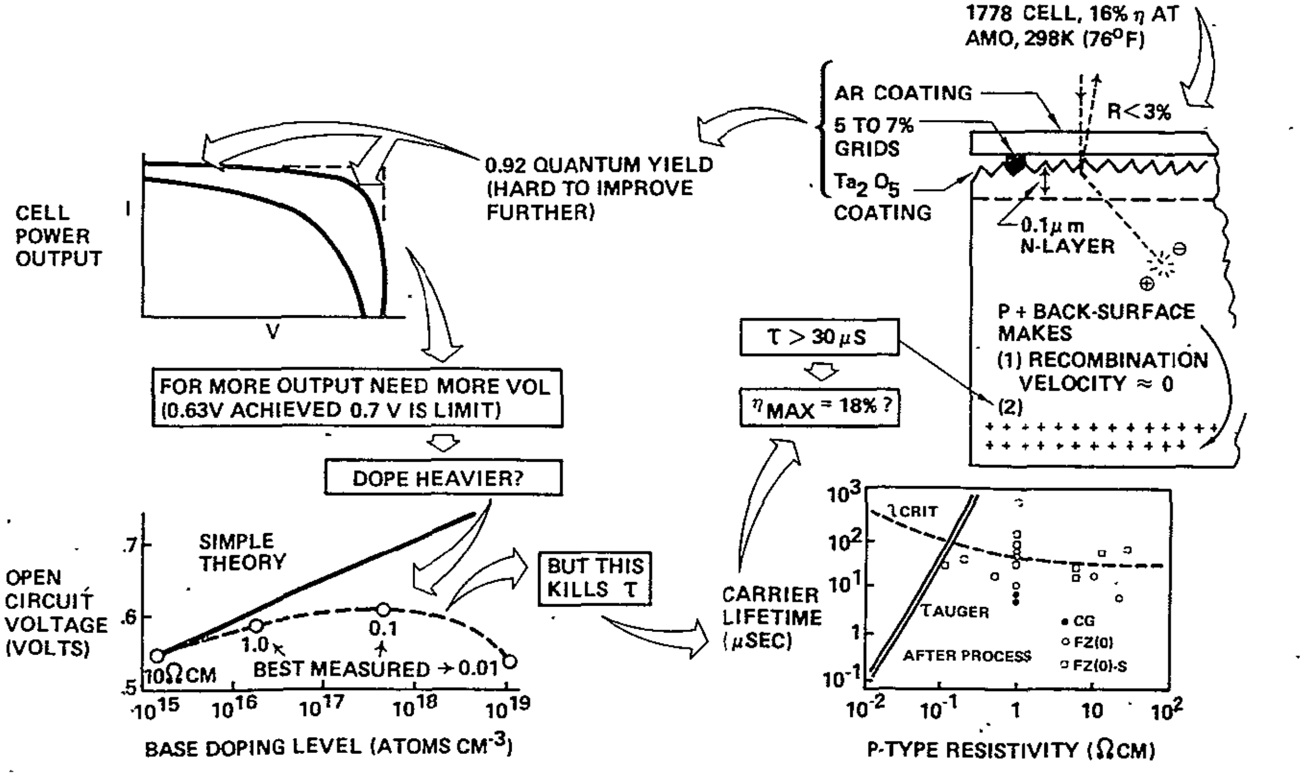

Fig. 4-29. Fundamental Limitations May Enforce Performance Plateau

Note that Figure 4-28 also provides temperature effects on the cells. The baseline cell thickness for Figure 4-28 is 100 μM (4 mils); this thickness was baselined for this study.

The performances for the 1990-1995 time period may exceed physical limitations, at least as regards silicon. Some reasons for this expectation are given in Figure 4-29 and are explained below.

The 1976 laboratory-model silicon solar cell, which could be in production in 1978, incorporates the following efficiency-enhancing features illustrated on the right:

- P^+ back-surface field reduced back-surface recombination velocity to zero, and contributed to a bulk minority-carrier lifetime of 30 microseconds.
- Textured silicon surface reduces reflection loss, and deflects light so that infra-red rays follow an oblique path through the silicon, increasing the probability of absorption of infra-red photons.
- Ta_2O_5 anti-reflecting coating matches the index of refraction of silicon to vacuum so that the reflection loss from the solar-cell and cover assembly is only about 3 percent.
- The shallow junction-(0.1 μm deep) improves conversion of ultraviolet photons.

Figure 4-30 gives the baseline silicon cell radiation resistance. Note the importance of consideration of solar flare protons. Gallium arsenide heterojunction cell radiation resistance data is limited; a survey indicates that such cells may be approximately three times more radiation resistant than silicon cells.

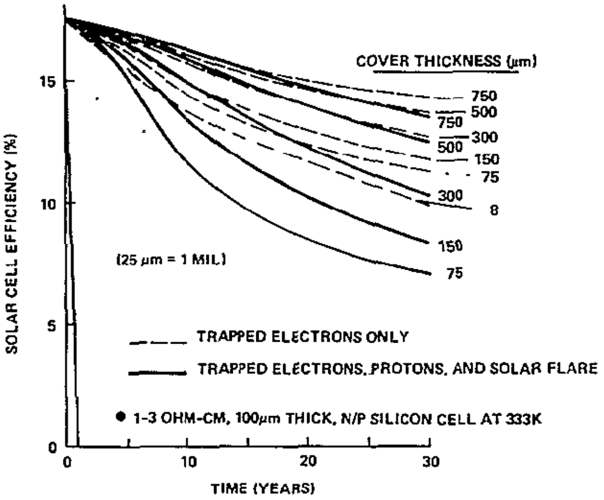

Fig. 4-30. Silicon Cell Radiation Resistance

4.7.2.2 Cell Costs

For this study cell costing was based on a learning curve process; an 80% learning curve was baselined. (Each time the production volume doubles the cell costs are reduced by 20%.) The 80% learning curve was selected as best representing the "industry opinion" of what is the proper learning factor. The general aerospace product factor is nearer 90%.

Figure 4-31 shows the effect of an 80% learning factor on solar *array* costs. The array consists of the cells, covers, substrate, interconnections, etc., and as such represents a "ready to operate" solar blanket. Note that the unit of the abcissa is millions of square meters. The buy quantity required for 60 10 GW ground output satellites would be approximately 6000 million square meters with a concentration ratio of one.

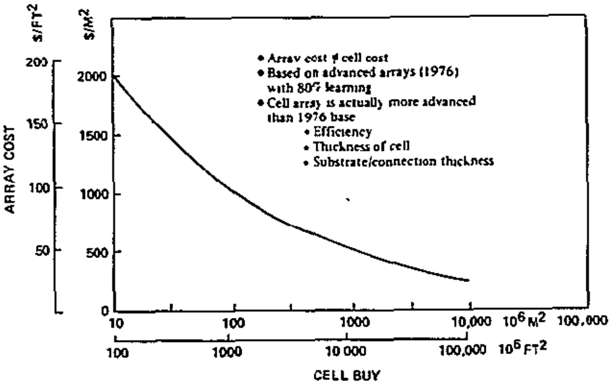

Fig. 4-31. Solar Array Buy Size Influences Cost

GaAs heterojunction cells are new and no production volume has been accumulated. Industry estimates of the cost of such cells relative to silicon range as high as 100. However, a comparison of the manufacturing steps involved and material costs indicated that GaAs heterojunction arrays should be baselined as costing twice as much per unit area as silicon arrays for equal production volumes.

These features, along with an optimized current-collecting grid configuration and improved junction processing, result in a 92 percent quantum yield and excellent fill factor. Significant further improvements in these areas are unlikely, leaving the output voltage of the cell as the remaining principal factor for improvement.

The highest open-circuit voltage obtained has been 0.63 volts. A 0.7 volt output at open circuit should be possible, and simple theory suggests that it can be obtained by increasing the base doping level. However, increased doping decreases bulk resistivity, and according to Fischer and Pschunder, puts the photovoltaic process into the Auger regime where carrier lifetime is reduced, decreasing quantum yield.

If the cell open circuit voltage can be raised to 0.664 volts from the 0.59 volts now obtained in the nonreflecting cells, and no other efficiency-influencing factors are degraded, then an 18 percent solar-cell efficiency is possible. Further improvement in silicon cells would require such phenomena as multiple charge-carrier generation by blue and violet photons, for which there is as yet no theoretical basis.

4.7.2.3 Radiation

Although the geosynchronous orbit location of SPS is high enough to escape the intense particle flux of the lower belt, trapped particles (primarily electrons) are still present. Solar flare particles can penetrate the geomagnetic field. Approximately three flare cycles can occur in the 30 year life of an SPS.

If all solar arrays were of the roll-up type, flare prediction could be used to indicate when roll-up was to be used. However, since all satellites would be affected almost simultaneously, this would not seem to be appropriate for SPS ("all the lights would go out").

Cell degradation versus time in orbit is shown for a range of cover thickness. By comparing the dashed and solid lines the effects of flares can be seen.

Radiation resistance of solar cells from protons and electrons as a function of solar cell and coverglass thickness will be predicted up to 1990. *In the last 9 years the solar cell degradation resistance has not changed, however the solar cell output at beginning-of-life has increased so that now more power is available from cells after irradiation than was available several years ago.*

4.8 TURBOMACHINES AND ASSOCIATED HEAT EXCHANGERS

4.8.1 Brayton Cycle

Principal elements of the closed Brayton cycle system are shown in Figure 4-32 in schematic form. The maximum gas temperature occurs just as the flow exits the heat exchanger tubing in the cavity heat absorber. The flow is then routed to

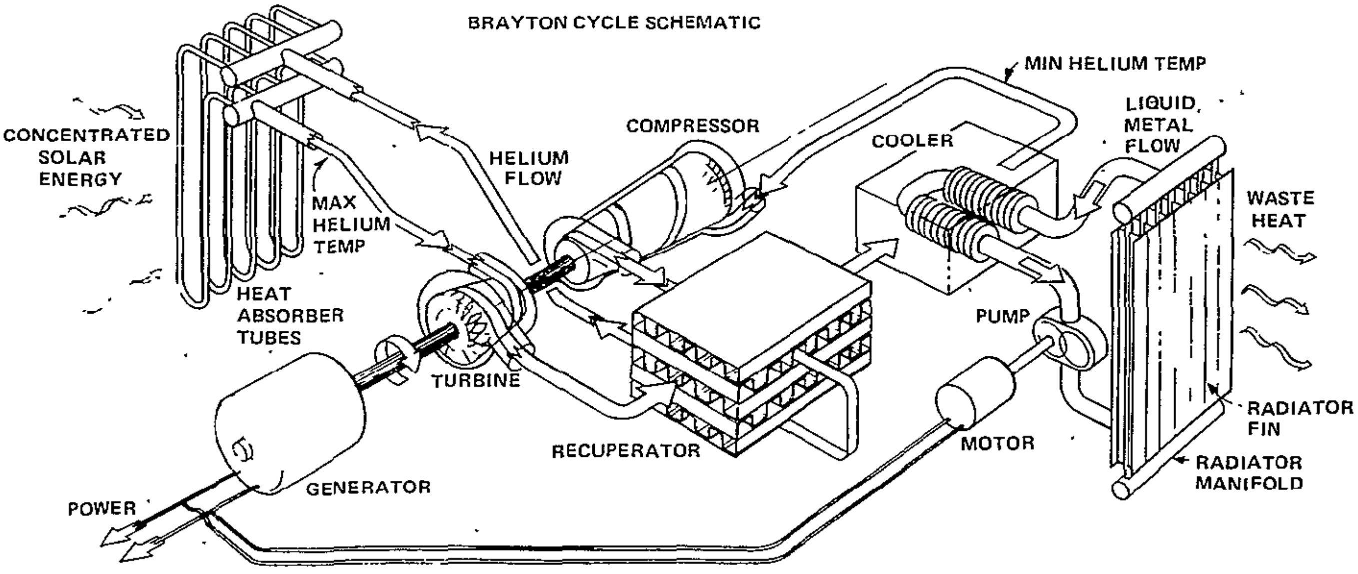

Fig. 4-32. Closed Brayton Cycle Schematic

the turbine where it expands, consequently undergoing a temperature reduction. The power thus produced turns the compressor (which moves the gas around the loop) and the generator which produces the electrical power. After leaving the turbine considerable energy remains in the gas; some energy is transferred to the "cold side" gas flow in the recuperator (a gas-to-gas plate/fin heat exchanger). The minimum gas temperature occurs in the cooler (a gas-to-liquid metal heat exchanger). Here cool liquid metal (NaK) from the radiator system absorbs heat energy from the gas. With the gas at minimum temperature it is ready for compression (the lower the gas temperature the lower the energy required to achieve a given temperature rise). After compression the gas flows through the recuperator, picking up the thermal energy from the "hot side" at the cycle, and again enters the cavity heat exchanger. Maximum gas pressure occurs at the compressor outlet.

4.8.2 Brayton Cycle Design Equations

Figure 4-33 is an approximate temperature-entropy (T-S) diagram for the closed Brayton cycle. The temperature (T) and pressure state points around the cycle are identified by the following subscripts:

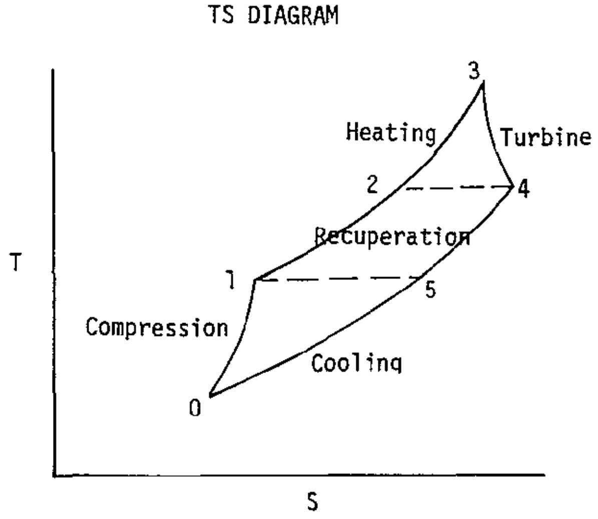

Fig 4-33. Cycle State Diagram

0 Compressor inlet (cooler outlet)
1 Compressor outlet (recuperator cold side inlet)
2 Recuperator cold side outlet (cavity heat absorber inlet)
3 Cavity heat absorber outlet (turbine inlet)
4 Turbine outlet (recuperator hot side inlet)
5 Cooler inlet (recuperator hot side outlet)

Thus T_3 is the maximum gas temperature in the cycle. Other state points associated with the cooler are:

T_{L1} Cooler liquid (NaK) side
T_{L2} Cooler liquid (NaK) side

Additional definitions:

P_1	Compressor discharge pressure
P_{r_c}	Compressor pressure ratio
P_{r_t}	Turbine pressure ratio
β	Pressure loss parameter = P_{r_t}/P_{r_c}
$\Delta P/P_t$	Closed loop total fractional pressure drop $\cong (1-\beta)$
E_R	Recuperator Effectiveness = $\frac{T_2 - T_1}{T_4 - T_1} = \frac{T_4 - T_5}{T_4 - T_1}$
E_C	Cooler gas side effectiveness = $\frac{T_5 - T_0}{T_5 - T_{L1}}$
E_1	Cooler liquid side effectiveness = $\frac{T_{L2} - T_{L1}}{T_5 - T_{L1}}$
$\wp_C$	Capacity ratio = E_1/E_C
$\Delta P/P_{REC}$	Total recuperator pressure drop for both sides
$\Delta P/P_{CLR}$	Cooler pressure drop = 0.32 x $\Delta P/P_{REC}$
η_{misc}	Miscellaneous efficiency losses, including bearing losses (approx. 2%)
η_c	Compressor efficiency
η_t	Turbine efficiency
F	Total pressure drop around gas loop

Some fundamental relationships for the closed Brayton cycle are given below:

DESIGN EQUATIONS

$$T_1 = \left(\frac{P_{rc}^{0.4} - 1}{\eta_c}\right) + 1$$

$$T_2 = T_1 + E_R (T_4 - T_1)$$

$$T_4 = T_3 \left\{1 - \eta_T \left[1 - \left(\frac{F}{P_{rc}}\right)^{0.4}\right]\right\}$$

$$T_5 = T_4 - E_R\,(T_4 - T_1)$$

$$T_{L1} = T_5 - \frac{T_5 - T_o}{E_c}$$

$$T_{L2} = E_L\,(T_5 - T_{L1}) + T_{L1}$$

Engine Efficiency =

$$\eta_{misc} = \frac{\dfrac{P_{rc}^{0.4} - 1}{\eta_c} + \dfrac{T_4 - T_1 \quad (1 - E_R)}{T_o}}{\dfrac{\eta_T\left[1 - \left(\dfrac{1 + F}{P_{rc}}\right)^{0.4}\right]}{\dfrac{T_o}{T_3}} + \dfrac{(T_4 - T_1)\,(1 - E_R)}{T_o}}$$

4.8.3 Brayton System Parametrics

4.8.3.1 Working Fluid Selection

Parametric descriptions of the Brayton turbomachine set, the recuperator and the cooler were prepared by the Garrett Corporation. They determined that the working fluid should be a Zenon-Helium gas.

The first baseline system included the selection of a Xenon-Helium gas mixture working fluid with a molecular weight of 8 instead of Helium. This selection was based on the heat exchanger specific weight being equal with the turbocompressor variations as shown. The Xenon-Helium turbocompressor incorporates a lighter and shorter rotor which is more amenable to use of hydrostatic gas bearings. Longer turbine blading will result in increased efficiency potential. Figure 4-34 shows the layout of the first baseline system.

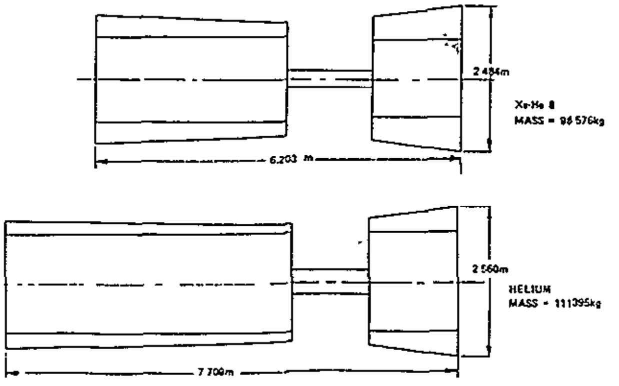

Fig. 4-34. Xenon-Helium Mixture Results in Lighter and Smaller Turbomachine

4.8.3.2 Parametrics

A baseline design was first prepared. Then the effects of changes in significant parameters were calculated. These effects are called influence coefficients.

Specific weight influence coefficients were generated for the turbocompressor, recuperator and cooler components. These influence coefficients were developed for both metallic (ASTAR 811C) and ceramic turbine structures.

The metallic turbocompressor specific weight increases with turbine inlet temperature as shown in Figure 4-35 because of the additional material required to contain the high pressure working fluid at the increased temperature. The recuperator, cooler and ceramic turbocompressor specific weights decrease with increased T_3 due to the reduction in cycle volumetric flow. Note that the silicon carbide turbine material has a constant design stress of 10,000 psi (68.95 MN/m^2) at temperatures up to 3000°F (1922°K).

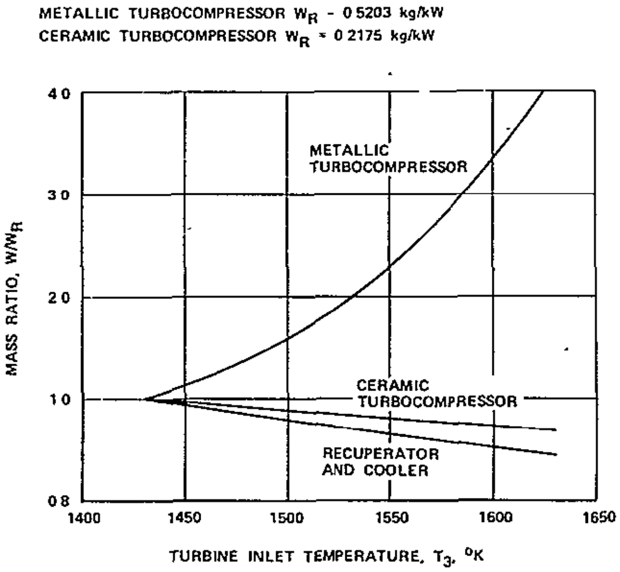

Fig. 4-35. Specific Mass Variation With Temperature (Example Influence Coefficient)

The density of silicon carbide is approximately 20 percent of the ASTAR 811C material baselined for the metallic turbine structure.

Tables 4-7 through 4-25 contain the influence coefficients used in the study.

Table 4-7. Influence of Cycle Max. Temperature

T_3	1330°K	1430°K	1530°K	1630°K
W/W_{ref}	1.0666	1.000	0.9419	0 8903

Table 4-8. Influence of Cycle Temperature Ratio on Recuperator/Cooler Mass

T_o/T_3	0.30	0.325	0.350	0.375	0 400
$(W/W_r)_{REC}$	0.7327	0.8523	1.0000	1.1895	1.4411
$(W/W_r)_{CLR}$	0.7563	0 8671	1.0000	1.1645	1.3736

Table 4-9. Influence of Recuperator Effectiveness on Recuperator/Cooler Mass

E_R	0.96	0.94	0.92	0.90
$(W/W_r)_{REC}$	1.5662	1.0000	0.7257	0.5653
$(W/W_r)_{CLR}$	1.0523	1.0000	0.9647	0.9374

Table 4-10. Influence of the Beta Factor on Recuperator/Cooler Mass

β	0 96	0.95	0.94	0.93
$(W/W_r)_{REC}$	0.9766	1.0000	1.0263	1.0552
$(W/W_r)_{CLR}$	0.9817	1.0000	1.0205	1.0432

Table 4-11. Influence of the Turbine Efficiency on Recuperator/Cooler Mass

η_t	0.930	0 915	0.900
$(W/W_r)_{REC}$	1.0000	1.0572	1.1144
$(W/W_r)_{CLR}$	1.0000	1.0483	1.0967

Table 4-12. Influence of the Compressor Efficiency on Recuperator/Cooler Mass

η_c	0.875	0 860	0.845
$(W/W_r)_{REC}$	1.0000	1.0411	1.0821
$(W/W_r)_{CLR}$	1.0000	1.0354	1 0708

Table 4-13. Influence of Recuperator Pressure Drop on Recuperator/Cooler Mass

$(\Delta P/P)_{REC}$	0.0375	0 0300	0.025	0.0214
$(W/W_r)_{REC}$	0.9228	1.0000	1.0710	1.1362
$(W/W_r)_{CLR}$	0.9804	1.0000	1.0162	1.0303

NOTE: · $(\Delta P/P)_{CLR}$ = 0 32 × $\Delta P/P_{REC}$

$(1-\beta) \cong \Delta P/P_{REC} + \Delta P/P_{CLR} + \Delta P/P_{ABSORBER}$

$+ \Delta P/P_{DUCTS}$

Table 4-14. Influence of Cycle Maximum Pressure on Recuperator/Cooler Mass

P_1	3800 kN/m²	4150 kN/m²	4500 kN/m²	4850 kN/m²	5200 kN/m²
$(W/W_r)_{REC}$	1.1358	1.0624	1.0000	0.9479	0.9024
$(W/W_r)_{CLR}$	1.0297	1.0142	1 0000	0 9871	0.9748

Table 4-15. Influence of Cooler Effectiveness on Cooler Mass

E_c	0.89	0 92	0.94
$(W/W_r)_{CLR}$	0.6269	1.0000	1.9639

Table 4-16. Influence of the Ratio of Liquid and Gas Side Cooler Effectiveness on Cooler Mass

ϕ_c	0.89	0.92	0.95
$(W/W_r)_{CLR}$	0 7055	0.8230	1 0000

Table 4-17. Influence of Cycle Maximum Temperature on Turbocompressor Mass

T_3	1330°K	1430°K	1530°K	1630°K
$(W/W_r)_{T\text{-}C_M}$	0.6203	1.0000	1.9784	4.1623
$(W/W_r)_{T\text{-}C_C}$	1.0369	1.0000	0.9668	0.9366

Table 4-18. Influence of Beta Factor on Turbocompressor Mass

β	0.96	0.95	0.94	0.92
$(W/W)_{T\text{-}C}$	0.9841	1 0000	1.0183	1.0385

Table 4-19. Influence of Beta Factor on Turbocompressor Mass

T_o/T_3	0.300	0.325	0 350	0.375	0.40
$(W/W)_{T\text{-}C}$	0.7453	0.8617	1.0000	1.1703	1 38

Table 4-20. Influence of Compressor Efficiency on Turbocompressor Mass

η_c	0.875	0.860	0.845
$(W/W_r)_{T\text{-}C}$	1.0000	1.0371	1.0741

Table 4-21. Influence of Turbine Efficiency on Turbocompressor Mass

η_t	0.930	0.915	0.900
$(W/W_r)_{T\text{-}C}$	1.0000	1.0495	1.0990

Table 4-22. Influence of Recuperator Effectiveness on Turbocompressor Mass

E_R	0.96	0.94	0.92	0.90
$(W/W_r)_{T\text{-}C}$	1.0606	1.0000	0.9584	0.9256

Table 4-23. Influence of Compressor Outlet Pressure on Turbocompressor Mass

P_1	3800 kN/m^2	4150 kN/m^2	4500 kN/m^2	4850 kN/m^2	5200 kN/m^2
$(W/W_r)_{T\text{-}C}$	1.1818	1.0833	1.0000	0.9286	0.8667

Table 4-24. Influence of Cycle Pressure Ratio on Recuperator, Cooler and Turbocompressor Mass

P_{r_c}	1.65	1.75	1.822	1.95	2.05	2.15
$(W/W_r)_{REC}$	1.1534	1.0513	1.0000	0.9373	0.9056	0.8847
$(W/W_r)_{CLR}$	1.1386	1.0468	1.0000	0.9382	0.9058	0.8812
$(W/W_r)_{T\text{-}C}$	1.1567	1.0545	1.0000	0.9290	0.8893	0.8593

Table 4-25. Reference Masses for Recuperator, Cooler and Metallic and Ceramic Turbomachines

$(W_r)_{REC}$ = 455,122 lbs = 206,443 kg = 0.6881 kg/kW
$(W_r)_{CLR}$ = 184,825 lbs = 83,837 kg = 0.2795 kg/kW
$(W_r)_{T\text{-}C_M}$ = 344,100 lbs = 156,083 kg = 0.5203 kg/kW
$(W_r)_{T\text{-}C_C}$ = 143,871 lbs = 65,260 kg = 0.2175 kg/kW

NOTE: $(W_r)_{T\text{-}C_M}$ is the mass of the turbocompressor with ASTAR 811-C turbine structure.

$(W_r)T\text{-}C_C$ is the mass of the turbocompressor with Silicon Carbide turbine structure. Silicon carbide has the following properties:

Design stress = 10,000 psi for large structures up to 3000°F.
Density = 0.119 #/in^3.

When all influence coefficients are at their nominal values the value of the factor influenced is 1.000. For example, in Table 4-24 when the cycle pressure ratio is 1.822 (the nominal value) the mass of the recuperator is equal to the reference mass (206,443 kg = 455,122 lbm per Table 4-25). Decreasing the cycle pressure ratio to 1.75 increases the recuperator mass by 5.13%. Thus, to find the mass of any system wherein the influence coefficients are not 1.00, the values are obtained from Tables 4-7 through 4-24. They are then multiplied together to obtain a factor which is in turn multiplied by the reference masses in Table 4-25 to obtain the mass of the system under consideration.

The above data were part of the total thermal engine SPS model used to optimize (obtain minimum total mass) the system. This process is described in section 5.0.

4.9 NUCLEAR REACTORS

4.9.1 Necessity for Breeder as SPS Reactor

Figure 4-36 gives estimates of the energy resources which probably exist within the United States.

Source	x 10^{18}Btu
Natural gas	0.7
Oil	1.5
Coal	30.0
U-235 (Burner reactors only)	4.3
U-238 (Breeder reactors only)	615.0

Fig. 4-36. United States Energy Resources

Importation of uranium is scheduled to begin before 1980. The programs in this study extend beyond the year 2040. Hence it is evident why only breeder reactors should be considered for SPS.

4.9.2 Breeder Reactor Program Concept

Reactor modules would be assembled and fueled in low orbit. Sixteen modules were baselined for a 10 GWe ground output nuclear SPS. Only two to four modules need be energized to provide the electric power necessary for the thrusters needed for a 100 day transfer to geosynchronous orbit (assuming 50% thruster efficiency). Thus when "self powering" away from low orbit, and still relatively near the atmosphere, only a relatively small quantity of fission products will be produced.

4.9.2.1 Example Program Concept (Molten Salt Breeder Reactor—MSBR)

In operation, a MSBR breeds U(233) from thorium. In a reactor module designed primarily for power production the fuel doubling time would be approximately six years. By placing design emphasis on breeding, this time could be reduced. Bred fuels are available for later SPS's. The basic fertile fuel which is carried up is thorium. All SPS's produce radioactive wastes. These could be accumulated at the SPS's, or accelerated to a remote location by a rocket disposal system. Geosynchronous orbital velocity and altitude provides an advantageous starting condition for such a system.

The breeder reactor program concept is shown in Figure 4-37.

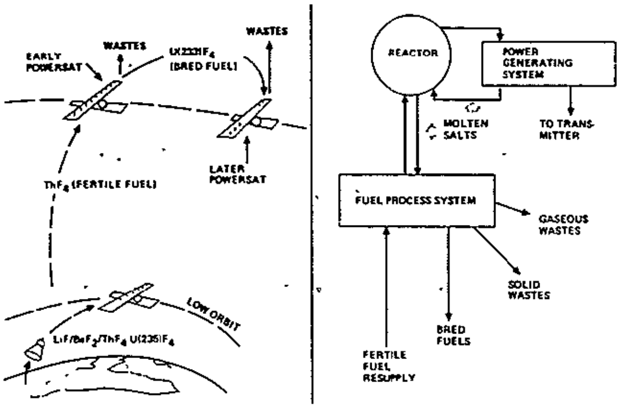

Fig. 4-37. Breeder Reactor Program Concept

4.9.3 Reactor Selection

In addition to being a breeder, the SPS reactor should have these characteristics:

1) Compatible with energy converter system.
2) Fuel reprocessing should be capable of being accomplished nearly automatically.
3) Core temperature should be approximately that achievable in the solar systems (at least 1500K (2240°F)).
4) 30-year useful life (with refueling as required).
5) Developable by 1991.

Approximately 15 reactors were investigated. Those having the greatest likelihood of achieving the above characteristics are given in Table 4-26.

Note that only the RPBR has the promise of achieving very high temperatures in combination with automatic fuel processing. The other reactor types have material compatibility problems. The problem here is that while it may be possible to buffer the walls of a reactor by an inert gas, or otherwise cool them, the hot reactor material must come in contact with components of the heat exchanger which interfaces the reactor to the power cycle (Brayton, Rankine, etc.). This is true for all known potential systems with the possible exception of magnetohydrodynamic (MHD) power generation where buffering of the MHD duct may be possible, or the rotating particle bed reactor (RPBR). Buffered nuclear MHD power generation is considered to be very advanced technology within limited possiblity of achievement by 1991, however the RPBR may be achievable in the required time period. Reactor types investigated as

Table 4-26. Emphasized Reactor Types

Reactor type	Fuel type	Breeding system	Fuel processing	Potential core life (year)	Material for heat exchanger	Maximum core temp (K/°F)
Molten salt breeder (MSBR)	Liquid UF LiF BeF$_2$ ThF$_4$ UF$_4$	In core with automatic separation loop	Liquid automatic loop	30 years with continuous reprocess	Hastelloy N	1030/ 1394
Very high temperature gas-cooled reactor (VHTR)	Enriched uranium (fissile), thorium (fertile)	Molten salt blanket or in core	Physical changeout of core elements	1 year before reload	Directs helium flow through graphite moderator and fuel elements of core	1280/ 2764
Uranium hexafluoride (UF$_6$)	UF$_6$	Either ThF$_4$ blanket or molten salt blanket	Gaseous automatic loop	30 years with continuous reprocess	Monel	900/ 1160
Rotating particle bed (RPBR)	UC$_2$ ZrC$_2$	Breeding blanket	Separate automatic loop	30 years with continuous reprocess	No heat exchanger-helium passes through particle bed	Perhaps 2000/ 3140

promising for satellite power are given in Table 6. Of these the RPBR is considered as the most practical for 1991 technology availability. The very high temperature gas cooled reactor (VHTR) has a high core temperature but suffers from poor reactor life and the difficulties associated with refueling of a solid core reactor. One additional possibility is the transparent partition (light bulb) reactor wherein energy is transported through transparent tubes (e.g., quartz) into an opaque gas (e.g., seeded helium). The study focus was therefore shifted to the RPBR, since this reactor in effect "side steps" the material compatibility problem.

The RPBR has been also studied for space nuclear propulsion. The fuel consists of uranium carbide-zirconium carbide particles which are retained by centrifugal force in a rotating drum, which is a porous metal cylinder through which the working fluid (helium) circulates into the particle bed. The gas flows radially inward through the particle. Finally the heated gas passes out axially along the drum. Primary questions for the RPBR are how low a pressure drop can be achieved across the bed, since this influences the Brayton cycle efficiency, and whether the helium mass flow is sufficient to cool the drum.

A fluidized bed reactor utilizes nuclear fuel consisting of small spherical or granular particles slightly suspended by a gas stream. Such reactors permit continuous fuel recycling and can be designed to heat gases to higher temperatures than would be possible for reactors using solid fuel elements. Since the fuel is in the form of small particles (typically 0.5 mm) the temperature differential between the center and edge of the particle is small compared to the temperature differentials inherent in a standard high temperature reactor core; this permits the working fluid gas to be heated to a temperature approaching the maximum operating temperature of the nuclear fuel.

In addition to the high temperature capability of such reactors, the potential of such reactors for breeding with continuous fuel recycle is of considerable interest both for terrestrial and space applications. For example, ERDA is currently supporting work at Georgia Tech[1] on the design and analysis of the Fluidized Carbon Coated Particles Reactor (FCCPR) and its associated fuel cycle to reduce the potential for nuclear proliferation. This particular project is designing a nuclear electric power station in the few hundred MWe range for export to third world countries and includes reactor physics and fuel cycle characteristics of a sustainer reactor (breeding ratio about 1.0) and advanced conversion technologies; evaluation of the safety of the system including handling and transportation of the wastes, economic assessment, assessment of problems areas, and a development plan.

Fluidized bed reactors operate by suspending the fuel particles in the gas stream, but not entraining the particles in the gas. Figure 4-38 illustrates the basic principles.

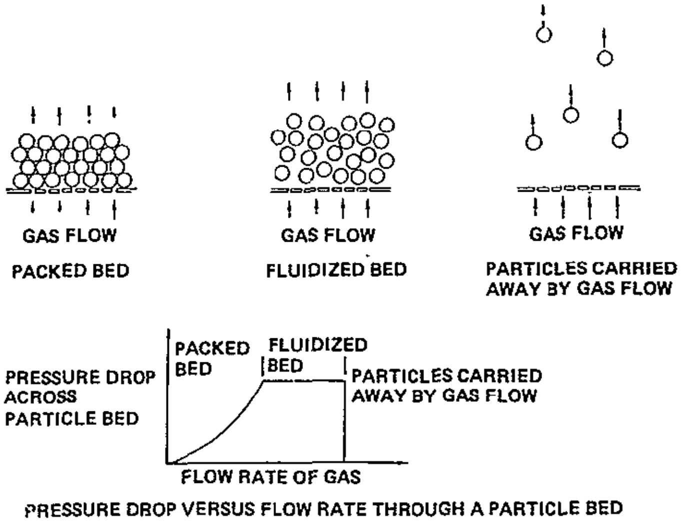

Fig. 4-38. Particle Bed Reactor Concept

If a gas is blown upward through a packed bed of particles, then at low flow rates the particles will remain packed and the gas will simply flow through the bed of particles and out through the upper surface. When the flow rate is increased beyond the minimum flow rate required for fluidization, the particles are no longer packed but are buoyed upward to form an expanded bed of agitated particles which behave as a liquid. This is an important difference between a fluidized bed and a packed bed—a packed bed does not behave as a liquid whereas a fluidized bed does, since the individual particles in a fluidized bed behave similarly to molecules in a liquid, interacting with nearby particles through collisions rather than by resting upon the nearest particles. The pressure drop across a fluidized bed is equal to the weight of the bed divided by the area of the supporting surface.

If the flow rate is increased still further the particles will be blown completely out of the bed. Since the drag force on the particle is proportional to its area while its mass is proportional to its volume, small particles are subject to a greater aerodynamic drag per unit mass than large particles. A particle will leave the bed only when the aerodynamic drag exceeds the "weight" of the particular particle. In space the gravitational force is simulated by centrifugal acceleration.

The proposed working fluid for the reactor and Brayton cycle is a helium-xenon mixture with an average molecular weight of 8. Since naturally occurring xenon has an atomic mass of 131.3 and helium has an atomic mass of 4, the atom percent of xenon in the mixture is 3.14%. Xenon occurs naturally as a mixture of 9 stable isotopes as listed below.

Isotope	% Abundance	Thermal Neutron Cross Section (barns)
Xe-124	0.096	100 ± 20
Xe-126	0.090	1.5 ± 1
Xe-128	1.92	0.43 ± 0.1
Xe-129	26.44	21 ± 7
Xe-130	4.08	0.34 ± 0.08
Xe-131	21.18	110 ± 20
Xe-132	26.89	0.53 ± 0.1
Xe-134	10.44	0.23 ± 0.02
Xe-136	8.87	0.28 ± 0.03

The average cross section of natural xenon is 24.5 barns, as compared with less than 0.007 barns for helium. The average cross section of the helium-xenon mixture (M = 8) is 0.78 barns. This is close to the 0.534 barns cross section of sodium and the 0.66 barn cross section of water, thus the average thermal neutron absorption cross section for the helium-xenon mixture is close to that of other conventional reactor coolants. Since the helium-xenon mixture is a gas, its atom density at projected reactor operating temperatures is only about 1% that of liquid water or sodium, so its macroscopic cross section will be about 100 times less. Thus, the relatively high microscopic cross sections of some of the xenon isotopes are not expected to present any problem as far as the neutronics of the reactor is concerned.

Work to date on rotating fluidized bed reactors has been concerned with non-breeders only, and no nuclear calculations for fluidized bed breeders are available. However, the critical mass of such a breeder can be estimated from earlier studies of gas core breeders. A typical UF_6 breeder reactor configuration[4] has a critical mass of 250 Kg. This is lower than the 1109 Kg for the Clinch River LMFBR or the 1468 Kg for the MSBR because of the absence of structural materials within the core. Since critical mass calculations have not been performed for rotating particle-fueled breeders, reactor parameters will be calculated for critical masses in the range of 250 to 2000 kg. Promising uranium-bearing fuels are:

Fuel	Density (gm/cc)	Melting Point (°K)
UC_2	11.28	2620
UO_2	10.96	2770
UN	14.31	2900

The mass density of uranium in these fuels is 10.2 for UC_2, 9.64 for UO_2, and 13.5 for UN.

For the case of UO_2 particles with an 80% void fraction, the inner diameter of the cylindrical reactor vessel is calculated assuming its length equal to the diameter and a fluidized bed thickness of 5% of the diameter. The results are:

Critical Mass (Kg)	Reactor Inner Diameter (m)
250	0.94
500	1.18
1000	1.49
2000	1.88

The pressure drop per unit thickness of a rotating fluidized bed is given by[5,6]

$$\frac{\Delta P}{\Delta X} = \frac{180 \mu V \,(1-\epsilon)^2}{D_p^{\,2} \;\; \epsilon^3} = (\rho_p - \rho_g)(1-\epsilon) R_c \omega^2$$

where:

ΔP	=	pressure drop across the bed	N/m^2
ΔX	=	thickness of fluidized bed	m
μ	=	Viscosity of gas	Kg/m sec
V	=	velocity of gas through bed	m/sec
D_p	=	particle diameter	m
ϵ	=	void fraction of fluidized bed	
ρ_p	=	mass density of particle material	Kg/m^3
ρ_g	=	mass density of gas	Kg/m^3
R_c	=	radius of chamber (bed radius)	m
ω	=	rotational velocity of bed	rad/sec

The minimum rotational velocity required to contain the particles in the bed is

$$\omega = \left(\frac{\Delta P}{\Delta X . R_c \rho_p (1-\epsilon)}\right)^{1/2}$$

Reynolds' number for <u>*minimum*</u> fluidization is given by

$$Re_{mf} = [(33.7)^2 + 0.0408\,Ga]^{1/2} - 33.7$$

where $Ga = \dfrac{D_p{}^3 \rho_g(\rho_p - \rho_p)\, a'}{\mu^2} = D_p{}^3\, a$

$$Re = \frac{\dot{m} D_p}{A\mu} = D_p V \frac{\rho_g}{\mu} = D_p V X$$

$\dot{m}$ = fluid mass flow rate
a' = radial acceleration for minimum fluidization condition
A = area of fluidized bed = $2\pi R_c L$
L = length of bed

Therefore, the maximum radial acceleration under which the bed remains fluidized is

$$a' = \frac{VX(D_p VX + 67.4)}{0.0408\, D_p{}^2 Y}$$

In addition

$$\Delta p_s = \left[\frac{150(1-\epsilon)}{Re} + 1.75\right] \frac{\Delta X\, \dot{m}^2 (1-\epsilon)}{A^2 D_p \epsilon^2 \rho_g (32.17)}$$

for a settled bed.

The velocity of the gas through the bed is found from

$$V = \dot{m}/\rho_g A$$

where $\dot{m}$ is the mass flow rate and A is the area of the bed, equal to $2\pi R_c L$, where L is the length of the chamber. The mass flow rate of the H_e/X_e mixture is

$$\dot{m} = \frac{Q}{0.79\, C_p T_e}$$

where Q is the reactor power output, C_p is the heat capacity of the gas mixture, and T is the reactor exit temperature. C_p = 2600 J/Kg°K. The viscosity of the mixture is found from[7]

$$\mu_f = 0.2137 \times 10^{-4} \left(\frac{T}{273}\right)^E$$

with $E = 0.65548 - 0.18338 \times 10^{-4}\, T + 0.59797 \times 10^{-8}\, T^2$

Consider, for example, the following case:

D_p = 0.0005 m (500 microns)
ρ_p = 10960 Kg/m^3 (UO_2)
T = 2000°K
P = 4136856 N/m^2 (600 psi)
ϵ = 0.8
R_c = 0.745 m (for 1000 Kg critical mass)
Q = 10^9 W (1000 MWt)
ρ_g = 1.99 Kg/m^3
$\dot{m}$ = 243.4 Kg/sec
A = $2\pi R_c(2R_c) = 6.97$ m^2
V = $\dot{m}/\rho_g A = 17.55$ m/sec
μ = 7.6855×10^{-5} Kg/m sec
ΔX = $0.1\, R_c = 0.074$ m
ΔP = 6386.2 N/m^2 (0.92 psi)
ω = 7.75 rad/sec (78.9 rpm)
a = $\omega^2 R_c = 50.95$ m/sec^2
y = 3.247×10^{12}
x = 25893
a' = 4042.3 m/sec^2 (minimum fluidization condition)
ω' = 73.66 rad/sec (minimum fluidization condition)
R_e = 227.2 m (minimum fluidization condition)
ΔP_s = 11345 N/m^2 (1.65 psi)

The operating range for the reactor is between the minimum fluidization condition ω' and ω. Particles are lost if the rotational speed is less than ω, and the bed is not fluidized if the rotational speed exceeds ω'. The pressure drop across the bed remains about 1 psi.

The temperature difference between the center of the fuel particle and its surface is calculated from

$$\Delta T_p = \frac{q''R_p^2}{6k_p}$$

when q''' is the internal heat generation rate in W/m^3 and k_p is the thermal conductivity. In the case of UO_2 particles with a k_p of only 0.29 J/m^oKsec this temperature difference is 346°K for a 1000 MWt reactor with a 1000 Kg critical mass. For uranium carbide particles this temperature difference drops to 42°K.

The heat transfer coefficient for the particle bed is calculated from[2]

$$Nu \cdot \epsilon = 2.06\ Re^{0.425} Pr^{1/3}$$

where $Nu = h\ D_p/k_g$. With $\epsilon = 0.4$ and Pr close to unity, h has a value of about 60,000 $W/m^{2\,o}K$. 500 micron UO_2 particles have a surface area of 1.09 m^2/Kg. For a critical mass of uranium fuel of 1000 Kg, the total mass loading of UO_2 particles in the reactor is 1137 Kg, with a total surface area of 1239 m^2. The difference in temperature between the particle surface and the bulk gas is then

$$\Delta T_{pg} = \frac{Q}{h(\text{area})} = 13.5^oK$$

for a 1000 MWt reactor. For $\epsilon = 0.8$, this becomes 27°K. Thus, adding the temperature difference between the particle surface and center, the temperature drop from the center of the particle to the bulk gas is

	$\epsilon = 0.4$	$\epsilon = 0.8$
Uranium Dioxide	360°K	373°K
Uranium Carbide	56°K	69°K

Thus, exit gas temperatures in the range of 2000°K should be possible without danger of particles melting.

Derivation of SPS configurations to utilize the above reactor concepts is given in section 5.0.

REFERENCES

1) "Fluidized Carbon Coated Particles Reactor Concept," ERDA Contract No. E-(40-1)-5273, Georgia Institute of Technology, Amt. $40,000, Duration Oct. 1, 1976-Dec. 31, 1976.

2) "Rotating Fluidized Bed Reactor for Space Nuclear Propulsion," Brookhaven National Laboratory Report BNL 50362, September 1972.

3) "Engineering Study of Cooloid Fueled Nuclear Rocket," Aerospace Research Laboratories Report No. 69-0234, prepared by Westinghouse Astronuclear Laboratory, December 1969.

4) "Analysis of UF_6 Breeder Reactor Power Plants," J. R. Williams, J. D. Clement and J. H. Rust, Georgia Tech, NASA Grant NSG-7067, November 1974.

5) "Fluidization and Fluid Particle Systems," Zenz and Othmer, Reinhold Publishing Corp., New York, 1960.

6) "Two Component Vortex Flow Studies, With Implications for the Colloid Core Nuclear Rocket Concept," L. A. Anderson, S. Hasinger and B. N. Turman, AIAA Paper No. 71-637.

7) Ted Mock, Garrett Corporation, private communication.

8) Wen, C. Y. and Yu, Y. H., "Mechanics of Fluidization," *Chem. Eng. Progr. Symp. Ser.*, No. 67, Vol. 62, 100, (1966).

4.10 RADIATORS

4.10.1 Meteoroid Environment

The fluid-loop thermal radiator design must consider meteoroid armoring requirements. Armoring places significant design constraints and mass penalties on the radiator.

The average total meteoroid environment (average sporadic plus a derived stream) was derived using the flux-mass model described in Reference (1). The flux-mass environment is shown in Figure 4-39. A mass density of 0.5 gm/cm^3 (.018 lbm/in^3) was used for all meteoroid particle sizes.

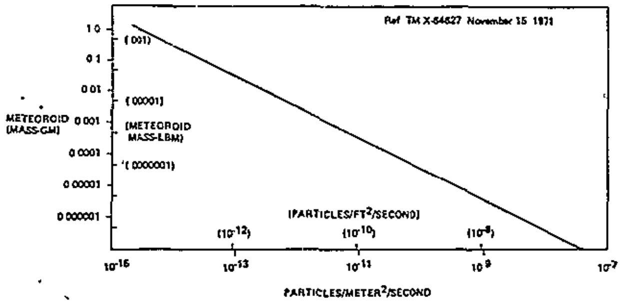

Fig. 4-39. Sporadic and Stream Average Total Meteroid Environment (Ommdirectional)

The meteoroid flux-mass environment shown in Figure 4-39 was calculated on the assumption that the distribution of meteoroid orbital directions with respect to the Earth is uniform. Actually, the majority of meteoroid orbits are close to the ecliptic plane as shown in Figure 4-40.

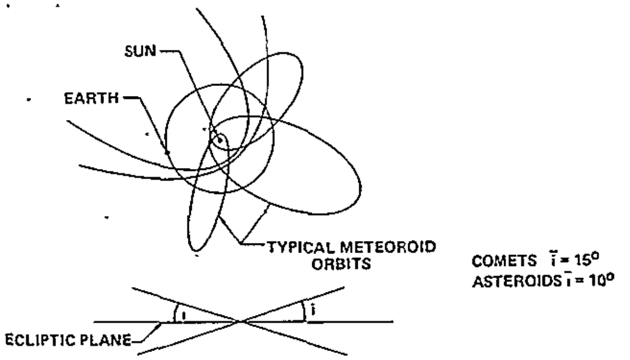

Fig. 4-40. Meteoroid Motion

The graph on the left of Figure 4-41 shows the observed meteoroid flux with respect to the ecliptic, and that on the right presents the distribution with respect to solar longitude, in the plane of the ecliptic. These figures were obtained from Reference (2).

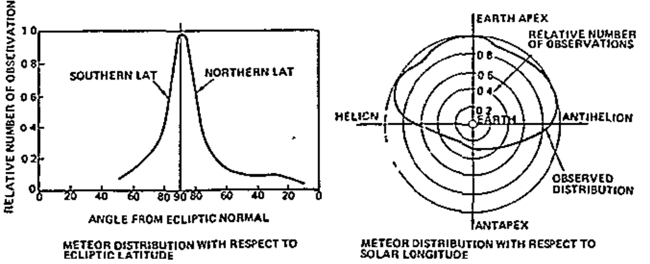

METEOR DISTRIBUTION WITH RESPECT TO ECLIPTIC LATITUDE

METEOR DISTRIBUTION WITH RESPECT TO SOLAR LONGITUDE

Fig. 4-41. Resultant Interaction With Object in Earth's Orbit

Both these distributions are apparent flux densities as observed from Earth; however, they clearly indicate the anisotropic distribution of meteoroids in space.

It is possible to preferentially orient the SPS radiators to take advantage of this anisotropic distribution of meteoroids in space.

Figure 4-42 shows that as the SPS orbits the Earth and the Earth orbits the Sun, the SPS is always pointing towards the Sun. The smaller figure shows the radiator oriented to be in the plane of the ecliptic and edgewise to the main meteoroid flux.

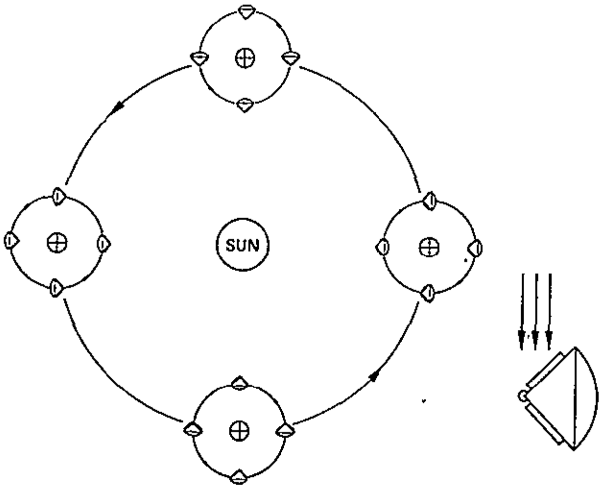

Fig. 4-42. SPS Radiators Can be Preferentially Oriented

Figure 4-42 showed the radiator placed in the plane of the ecliptic. Figure 4-43 shows the flux concentrated at a low angle to the ecliptic plane. This angular concentration extends around the leading edge of the radiator from helion to antihelion, as was shown in Figure 4-41. Thus, the radiator sees the meteoroid flux impinging in a concentration at an angle of approximately 15° to its plane of motion.

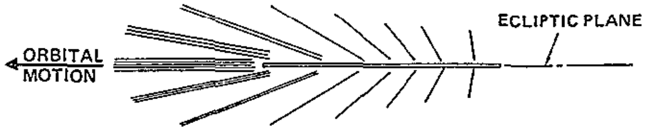

Fig. 4-43. Flux Seen by Radiator

The radiator consists of thousands of small tubes spaced at 50 mm (2 inches) to 75 mm (3 inches) apart, depending upon design. These tubes are most vulnerable to meteoroid damage since penetration would allow escape of coolant. Protection of the tubes by some form of barrier, therefore, is extremely important. To facilitate the design of a minimum weight barrier, a refined flux-mass model was derived taking into account the orientation of the flux concentration.

The refined flux-mass model, taking into account the directional flux concentration, is shown in Table 4-27. It was derived from the graphs in Figure 4-41. The left hand graph was divided into 10° wide increments or strips. The first column of the table is the mean angle of each strip. The second column is the relative number of observations represented by each strip. The third column is the percentage of the total number of observations; i.e., of the total flux, represented by each angular strip. Column four transforms the directional flux to the flux normal to the radiator plane; i.e., the ecliptic plane. It is the flux of column three multiplied by the sine of the appropriate angle. Column five is column four multiplied by the omnidirectional flux for meteoroid particles .001 gm (.0000022 lbm) or greater. Each line represents the proportion of the total flux contributed by each angular strip to the total flux normal to the ecliptic plane. Since the radiator tubes are spaced, the weighted flux of column five must be modified by a view factor to account for particles which are included in the flux, but which pass harmlessly between the tubes. These view factors are different for each angle. They are tabulated in column six for tubes spaced at 50 mm (2 inches) and in column eight for tubes spaced at 75 mm (3 inches). The final derived flux is the weighted flux multiplied by the view factor.

4.10.2 Tube/Fin Radiator

4.10.2.1 Panel Design Analysis and Modeling

The tube/fin radiator panel consists of a multitude of small diameter tubes joined to headers or manifolds at each end. The tubes are spaced 50 mm (2 inches) to 75 mm (3 inches) apart and are connected to each other by fins. Heated fluid (gas or liquid) is pumped through the tubes and waste heat radiated from the fins.

It is a provisional requirement that 70% of the system must still be operative after a 30-year life without repair or replacement. Applying this philosophy to the radiator, it means that no more than 30% of the tubes must be penetrated and that the damaged tubes must be isolated to prevent loss of coolant. The radiator must be divided into subpanels such that in combination with a barrier against an appropriate particle size, a minimum weight is achieved. A suitable size of subpanel for transportation into orbit in one piece is 20 m x 20 m (65.6 ft. x 65.6 ft.). This will require subdividing

Table 4-27. Derived Directional Meteroid Flux

Angle from θ° ecliptic	Relative number of observations	% of total flux	Aspect factor	Weighted hits/ m2/sec (hits/ft2/sec) ·001 gm (27 ^{5} lbm	View factor 50 mm tube	Hits/tube/m2/sec [/ft2/sec] 50 mm (2 ") tube spacing	View factor 75 mm(3") tube spacing	Hits/tube/m2/sec (/ft2/sec) 75 mm (3) tube spacing
N 5	895	467	041	4 92 x 10^{13} (4 57 x 10^{-14})	1 0	4 92 x 10^{13} (4 57 x 10^{14})	1 0	4 92 x 10^{-13} (4 57 x 10^{14})
15	362	189	049	5 88 x 10^{13} (5 46 x 10^{14})	73	4 29 x 10^{13} (3 98 x 10^{14})	6	3 53 x 10^{13} (3 28 x 10^{14})
25	176	092	039	4 68 x 10^{13} (4 35 x 10^{14})	49	2 29 x 10^{13} (2 13 x 10^{14})	36	1 68 x 10^{13} (1 56 x 10^{14})
35	.114	059	034	4 08 x 10^{13} (3 79 x 10^{14}	37	1 51 x 10^{13} (1 40 x 10^{-14})	26	1 06 x 10^{13} (9 8 x 10^{15})
45	090	047	033	3 96 x 10^{13} (3 68 x 10^{14})	31	1 23 x 10^{13} (1 14 x 10^{14})	22	8 71 x 10^{14} (8 09 x 10^{15})
55	095	049	.040	4 8 x 10^{13} (4 46 x 10^{14})	28	1 34 x 10^{13} (1 24 x 10^{14})	19	9 12 x 10^{14} (8 47 x 10^{15})
65	096	049	044	5 28 x 10^{13} (4 9 x 10^{14})	25	1 32 x 10^{13} (1 23 x 10^{14})	17	8 98 x 10^{14} (8 34 x 10^{15})
75	067	035	034	4 08 x 10^{13} (3 79 x 10^{-14})	24	9 79 x 10^{-14} (9 1 x 10^{15})	.16	6 53 x 10^{-14} (6 07 x 10^{15})
85	.024	.012	012	1 44 x 10^{13} (1 34 x 10^{14})	23	3 31 x 10^{14} (3.07 x 10^{15})	15	2 16 x 10^{14} 2.01 x 10^{15}
			Total	3 91 x 10^{-12} (3 63 x 10^{13}	Total	1 82 x 10^{12} (1 69 x 10^{13})	Total	1 47 x 10^{12} (1 37 x 10^{13})
S 5	767	657	048	5 76 x 10^{13} (5 35 x 10^{14})	1 0	5 76 x 10^{13} (5 35 x 10^{14})	1 0	5 76 x 10^{13} (5 35 x 10^{14})
15	281	204	053	6 36 x 10^{13} (5 91 x 10^{-14})	.73	4 64 x 10^{13} (4 31 x 10^{14})	.6	3 82 x 10^{13} (3 55 x 10^{-14})
25	176	128	054	6 48 x 10^{13} (6 02 x 10^{14})	.49	3 17 x 10^{13} (2 95 x 10^{14})	36	2 33 x 10^{-13} (2 16 x 10^{14})
35	109	079	.045	5 4 x 10^{13} (5 02 x 10^{14})	37	2 0 x 10^{13} (1 66 x 10^{14})	26	1 4 x 10^{13} (1 3 x 10^{14})
45	043	.031	022	2 64 x 10^{13} (2 45 x 10^{-14})	.31	8 18 x 10^{14} (7 6 x 10^{15})	22	5 81 x 10^{14} (5 4 x 10^{15})
			Total	2 66 x 10^{12} (2 47 x 10^{-13})	Total	1 64 x 10^{12} (1 52 x 10^{-13})	Total	1 39 x 10^{-12} (1 29 x 10^{13})

into smaller or mini-panels to achieve a radiator degradation of not more than 30% in 30 years. Using the total derived flux, from Table 4-27, for a particle of .001 gm (.0000022 lbm) or greater, the subpanels will require subdividing into 5 mini-panels for the 50 mm (2 inches) tube spacing and 4 mini-panels for the 75 mm (3 inches) tube spacing. As shown in Figure 4-44, each mini-panel will require an inlet and outlet valve for isolation in the event of tube penetration.

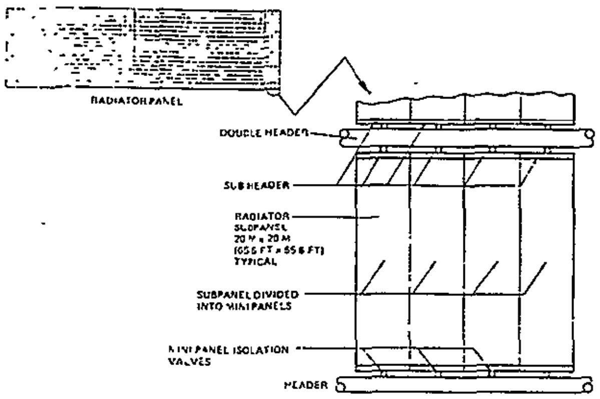

Fig. 4-44. Meteroid Shielding Philosophy

A computer analysis was conducted of radiator panel configurations designed to withstand the predicted meteoroid environment. Three basic configurations were studied. Figure 4-45 shows a section view and the thermal analysis nodal networks for each configuration.

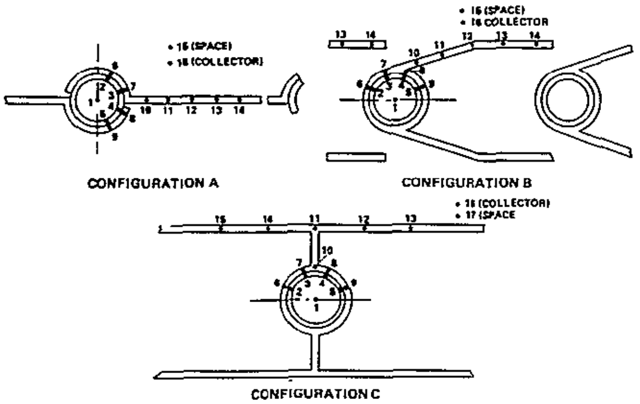

Fig. 4-45. Radiator Configurations

Configuration A relies on increased armor thickness around each tube for meteoroid protection; whereas Configurations B and C utilize fin structure as a bumper to fragment the meteoroids.

Forty-five parameter runs were conducted for each configuration to evaluate the optimum combination of tube pitch, tube diameter, and fin thickness.

Figure 4-46 was used in determining the dimensions of Configurations B and C of Figure 4-45. The first barrier is the radiator fin and the second is the armor around the tube. The main meteoroid flux is at a shallow angle to the radiator and increases the effective distance between the first and second barriers. Figure 4-46, taken from Reference (3) enables a minimum weight two-sheet aluminum barrier to be chosen for protection against a certain meteoroid particle.

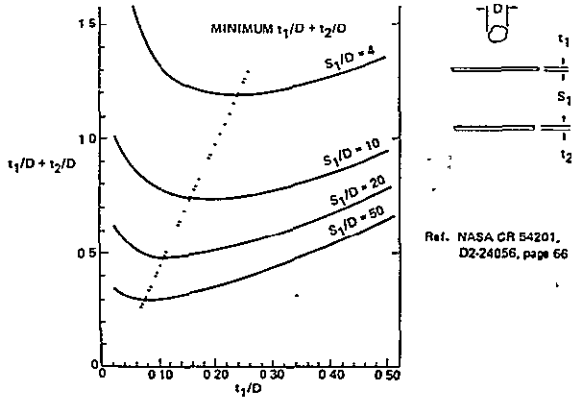

Ref. NASA CR 54201, D2-24056, page 66

Fig. 4-46. Minimum Weight Two-Sheet Aluminum Barrier

A segment of radiator structure (Figure 4-47) was divided into a nodal network and a steady-state energy balance was calculated at each node by a digital computer program. The Beta Computer Program solves steady-state and transient thermal problems when radiative, convective, and conductive thermal paths are defined.

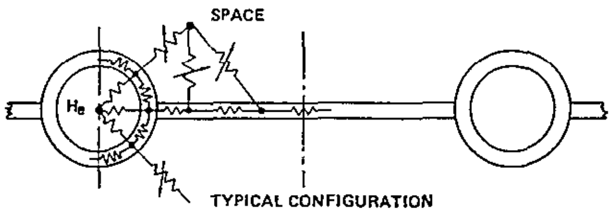

PARAMETER VARIABLES

- HELIUM FILM COEFFICIENT
- THERMAL CONDUCTIVITY
- FIN THICKNESS
- TUBE DIAMETER
- TUBE SPACING
- EMISSIVITY
- TUBE LENGTH

Fig. 4-47. Beta Program Solves Thermal Network Modeling of Radiator Structure

The heat rejection of a unit area of radiator surface was calculated as a function of radiator fluid temperature and the results were then integrated along a tube length to determine the drop in fluid temperature (Figure 4-48). A summation of the results for a single tube enabled the calculation of total radiator performance.

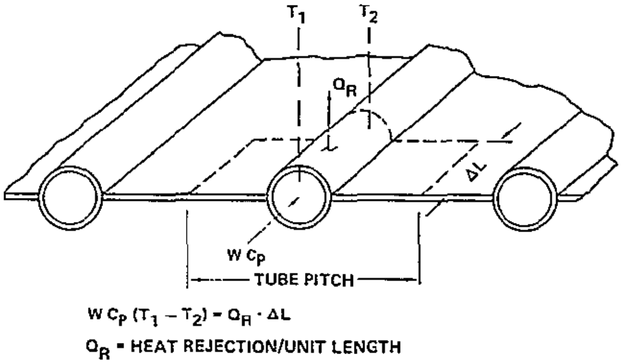

Fig. 4-48. Radiator Thermal Model

A comparison was made of radiator performance when tube pitch, tube diameter, and fin thickness were systematically varied to achieve an optimum configuration.

Two radiator concepts (Figure 4-49) were baselined as a result of an optimization exercise which selected the ratio of radiator temperature to Brayton cycle turbine inlet temperature. For minimum system weight this ratio is approximately 0.35. For Type A the maximum turbine inlet temperatures with superalloys (e.g., columbium) is 1300 K (1880°F); for Type B a turbine inlet temperature of 1750 K (2690°F) is baselined for refractory metals or ceramics. The above turbine inlet temperatures were used in a preliminary cycle design to evaluate radiator concepts.

	1990 superalloy (A)	2000 (B)
T_{in} K/°F	657/723	986/1315
T_{out} K/°F	459/366	702/804
$\bar{T}_{gas}$ K/°F	535/503	813/1003
T_{rad} K/°F	481/406	732/858
Q/A kW/m²/btu/ft² sec	2 73/0 240	14 6/1 29
P_{in} N/m²/lb/in²	$3\,4 \times 10^6/500$	$3\,4 \times 10^6/500$
ΔP	0 015	0 015
Total radiating area m²/ft²	$10\,9 \times 10^6/1\,17 \times 10^8$	$2\,5 \times 10^6/2\,67 \times 10^7$
Projected area of each of eight panels m²/ft²	$6\,8 \times 10^5/7.32 \times 10^6$	$1\,56 \times 10^5/1\,68 \times 10^6$

Fig. 4-49. Baseline Radiators

Many early studies were based on the use of helium as a radiator fluid because a trade study comparing helium with NaK showed helium provided a lighter system. Hence, the results shown in Figures 4-50 to 4-53 are based on helium as the working fluid.

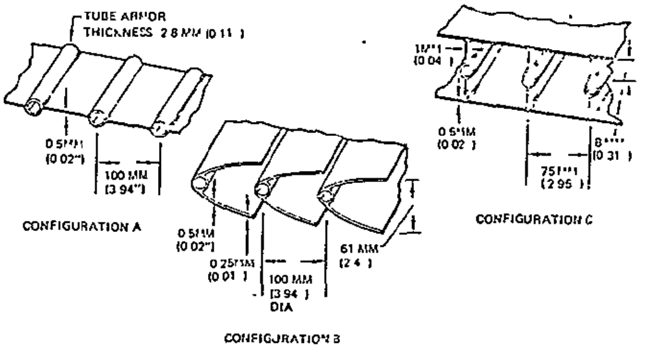

NOTE TUBE DIAMETER IS 12 7 MM (0 5"), WALL THICKNESS 0 13MM (0 005)

Fig. 4-50. Optimum Radiator Panel Dimensions — Low Temperature Helium Radiator

However, it appears that substantial advantages in the Brayton cycle turbomachinery loop resulted if heat were transferred from the Brayton gas loop to a radiator NaK loop. NaK radiator fluid was consequently used as baseline.

Optimum configurations of three types of radiator are shown in Figure 4-50. All take advantage of the anisotropic meteoroid flux and preferential panel orientation. Configuration A uses solid armor around the tubes and radiates heat from both sides of the fin. Configurations B and C use meteoroid bumpers, the outer sheet breaks up the meteoroids so that dispersion occurs before the tube is reached. Each candidate was designed to provide protection against particles of at least .001 gm (.0000022 lbm). Tubes were sized by the 30-year creep rupture strength with a minimum factor of safety of 2.0. For equivalent thermal and meteoroid protection, Configuration C yields the lightest radiator.

Figure 4-51 shows radiator heat rejection on an area basis. It is relatively insensitive to tube diameter.

Figure 4-52 shows the specific heat rejection (kW/kg or BTU/hr lbm) of radiator tube/fin panels with various tube diameters.

Table 4-27 shows optimum dimensional and performance data for the three configurations analyzed. Configuration 3 provided the best performance with year "A" materials and fluid temperatures.

Configuration 4 shows material and dimensional modifications providing optimum performance with "B" type radiator requirements.

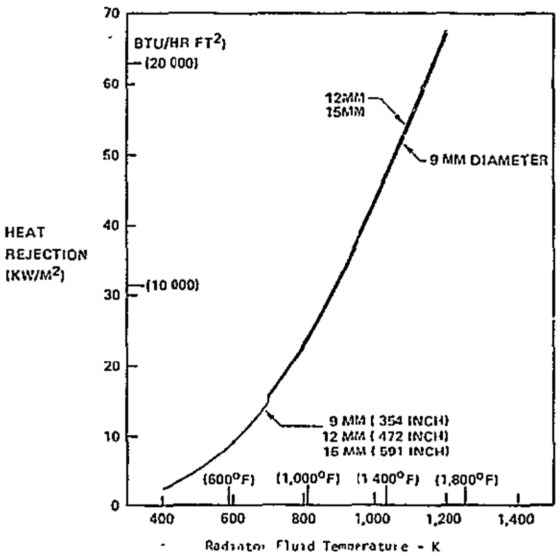

Fig. 4-51. Radiator Heat Rejection Helium Fluid

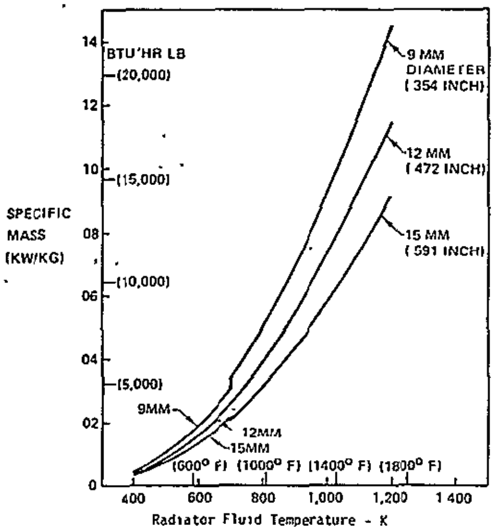

Fig. 4-52. Radiator Panel Mass Helium Fluid

Table 4-27. Optimum Configurations, Helium Radiator Fluid

Configuration	Average fluid temp K (°F)	Fin material	Tube material	Tube diameter mm(inches)	Fin thickness mm(inches)	Tube pitch mm(inches)	Heat rejection kw/m2 (Btu/hr ft^2)	Heat rejection kw/kg (Btu/hr lb)
 1	535 (503)	Aluminum 6061	Haynes 188	12.5 (.50)	.5 (.02)	100 (4.0)	5.55 (1759)	1.12 (1742)
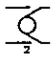 2	535 (503)	Aluminum 6061	Haynes 188	12.5 (.50)	.5 (.02)	75 (3.0)	4.33 (1373)	1.04 (1610)
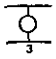 3	535 (503)	Aluminum 6061	Haynes 188	12.5 (.50)	.5 (.02)	75 (3.0)	5.95 (1889)	1.26 (1952)
 4	850 (1070)	Beryllium	Columbium 866	12.5 (.50)	.5 (.02)	50 (2.0)	25.6 (8127)	5.82 (9012)

Figure 4-53 shows that a much greater portion of the total radiator mass is allocated to the panels with the low temperature "A" radiator system. This results from the substantially greater radiating area required with the low temperature system since heat rejection is proportional to the fourth power of the absolute surface temperature.

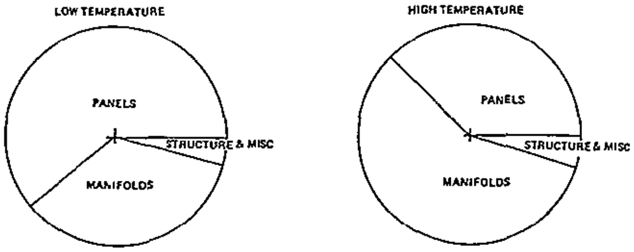

Fig. 4-53. Radiator Mass Distribution (Helium)

Table 4-28 shows the relative mass of radiators designed for the year 1990 and year 2000 powersats.

Table 4-28. Masses of High and Low Temperature Helium Radiators

Item	Low temperature		High temperature	
	10^6 kg	10^6 lbm	10^6 kg	10^6 lbm
Panels	24.7	54.4	7.0	15.4
Manifolds	13.3	29.3	10.6	23.4
Structures, miscellaneous	1.7	3.7	0.9	2.0
Total	39.7	87.4	18.5	40.8

Substantial reduction in radiator surface area and panel mass results with "B" (high temperature) components due to the higher operating temperature.

A lesser mass reduction occurs in the manifolds of the high temperature configuration, because, although the headers are shorter, greater wall thickness is necessary due to lower allowable stresses.

A trade study was conducted to compare a gaseous helium radiator concept with a liquid NaK radiator. The use of liquid NaK will require an additional gas-liquid heat exchanger and a circulating pump.

Figure 4-54 shows flow diagrams for the two systems. Pressure drop in the helium loop will be reduced with the NaK system with a resultant improvement in engine efficiency and the denser fluid allows smaller headers.

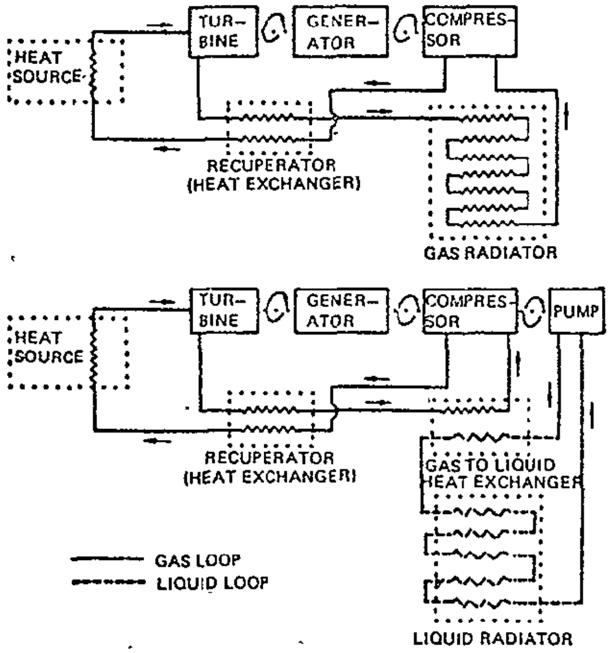

Fig. 4-54. Use of Liquid Radiator With Brayton Cycle Requires Additional Heat Exchanger

All liquid radiator working fluid candidates for the inlet temperature range of interest of 657K to 986K (723°F to 1315°F) are alkali metals. Selection was based on compatibility with the tubing material, stability over the temperature range and the fusion point. A near-eutectic of sodium and potassium (NaK) was selected; the boiling point is 1057K (1443°F), the fusion point is 262K (+12°F). Compatibility with columbium for exposure times up to three years has been demonstrated. Liquids provide high transfer rates and, due to their density, small header dimensions relative to helium. However, a separate gas-to-liquid heat exchanger is required for the Brayton cycle variants, and pump power and weight must be considered. Use of a separate gas-to-liquid heat exchanger can significantly reduce the pressure drop in the gas cycle. Table 4-29 shows masses for helium and NaK radiators (high temperature variant) which reject heat appropriate to the generation of 16 GW by a helium Brayton cycle.

Table 4-29. Masses of Gas and Liquid Radiators

Item	Helium		NaK	
	10^6 kg	10^6 lbm	10^6 kg	10^6 lbm
Panels	7.0	15.4	5.5	12.1
Manifolds	10.6	23.4	4.0	8.8
Structure miscellaneous	0.9	2.0	0.8	1.8
Working fluid	–	–	7.6	16.8
Gas to liquid heat exchanger	–	–	8.5	18.7
Pumps + pump power penalty	–	–	3.0	6.6
Brayton cycle efficiency factor	2.5	5.5	–	–
Totals	21.0	46.3	29.4	64.8

Each of these systems was optimized for minimum total weight. One factor contributing to the higher mass of the NaK system is the temperature drop across the gas-to-liquid heat exchanger of 30K (54°F) which reduces the radiator effectiveness. The "Brayton cycle efficiency factor" is the mass of solar concentrator and absorber system necessary to counter the efficiency loss resulting from the higher pressure drops in the gas system.

The optimum radiator panel configuration for the baseline Brayton cycle is shown in Figure 4-55. Liquid NaK is circulated through thin wall Haynes 188 alloy tubing.

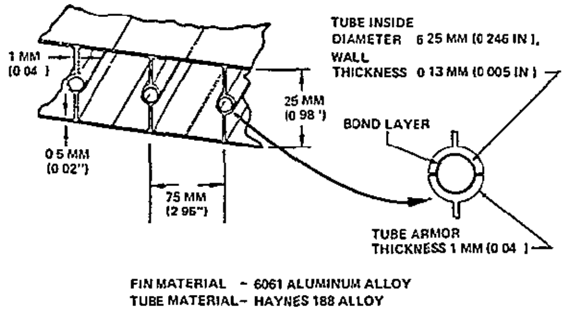

Fig. 4-55. Optimum Radiator Panel Dimensions Low Temperature NaK Radiator

Aluminum radiating fins are bonded to the tubing and provide a bumper for protection against meteoroids. Segmented construction is used to minimize thermal stresses.

4.10.3 Radiator Configuration

Various configurations were analyzed to obtain a radiator panel design of minimum mass as described in section 4.7.1.

Arrangements of these panels with different configurations of header and feeder manifolds were analyzed to provide a suitable radiator conceptual design of minimum mass.

Concept No. 1 is shown in Figure 4-56. This concept consists of input and output headers with a row of radiator panels between them. The headers are fixed in relation to each other at the feeder end and are free to expand at the other end. Due to the temperature difference between them

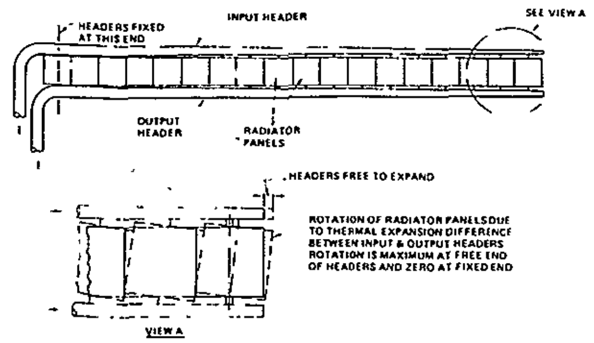

Fig. 4-56. Radiator Panel Arrangement — Concept No. 1

the headers will move laterally relative to each other and the panels will rotate as shown. This lateral movement due to temperature differential will take place during startup and shutdown and during occultation.

Figure 4-57 shows radiator panel arrangment, Concept No. 2. This concept is similar to the previous arrangment except that the headers are fed at their centers instead of at one end. The headers are fixed relative to each other at their centers with their ends free to expand. If the number of panels is the same as in the previous concept then the rotation of the end panels will be approximately half that of the previous concept, since the differential expansion of the header ends is halved.

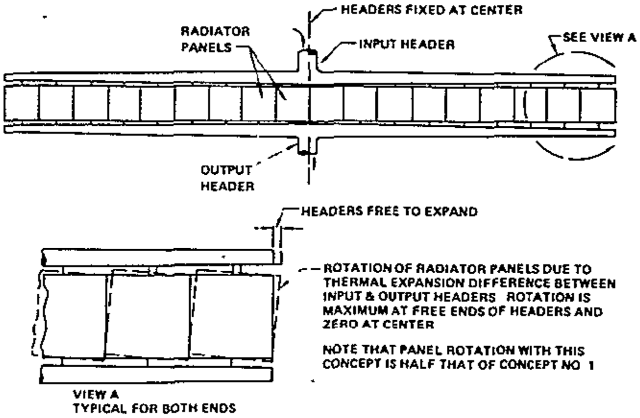

Fig. 4-57. Radiator Panel Arrangement — Concept No. 2

Figure 4-58 shows radiator panel arrangment, Concept No. 3. This concept is similar to the previous arrangment except that there are two rows of radiators between the input and output headers. As with the previous concept, the headers are fixed at their centers relative to each other and the ends are free to move.

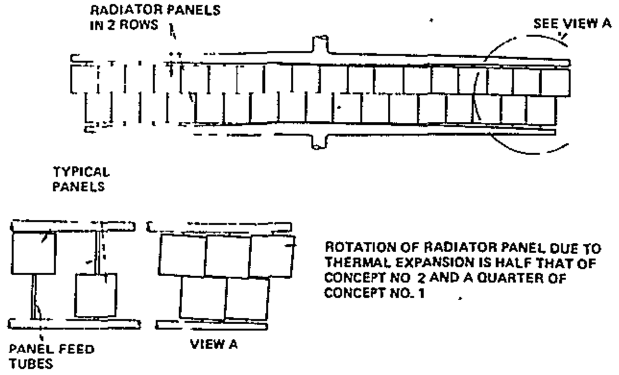

Fig. 4-58. Radiator Panel Arrangement — Concept No. 3

Since the distance between the headers is doubled the angular rotation of the panels is approximately half that of the previous arrangment, and a quarter that of Concept No. 1.

Note that, although there are two rows of panels, each panel is separately placed between the headers, alternately in the upper and lower rows. A 20m (65.6') long feed tube is required for each panel.

Figure 4-59 shows a typical arrangement of the radiator area associated with three 360 MWe turbogenerators. Each radiator section required per turbogenerator consists of 70 panels. The tapering headers are fed from the center. Input and output headers are fixed at their centers relative to each other so that movement due to thermal expansion is confined to the ends which are free. The structure which supports the radiator is designed to accommodate feeder length changes.

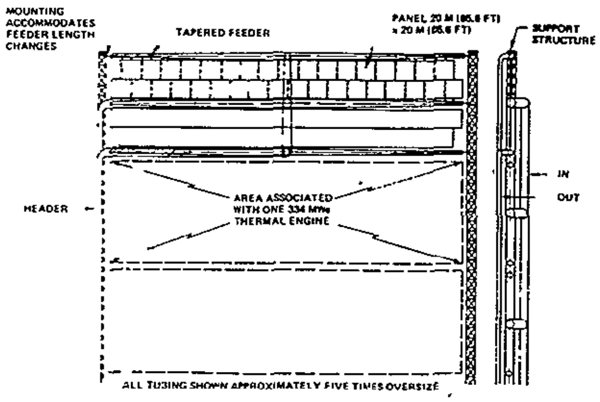

Fig 4-59. Radiator Configuration Concept

In system optimization initial runs produced parametric descriptions of power generation modules with radiators having feeders 1.6 times more massive than the panels which they feed. Consequently, radiator configurations were sought which would have lighter feeders. It was recognized that short feeders were dependent upon clustering the radiator panels as closely as possible about the heat source. Figure 4-60 shows both the original and a "halo" configuration which permits a minimum length for the feeders. In both cases the radiator lies in a single plane which is oriented "edge-on" to the predominant meteoroid flow.

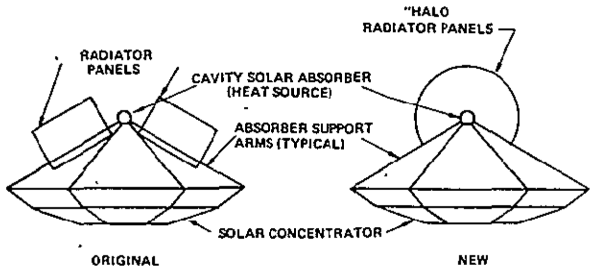

Fig. 4-60. Original and New Radiator Configurations

Figure 4-61 shows the original radiator arrangement with both supply and return feeders attached to the center of the headers. Constant supply and return feeder diameters are used up to the radiator panels where tapering headers are introduced.

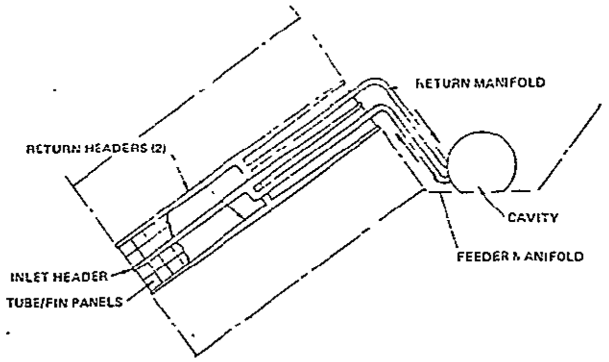

Fig. 4-61. Original Panel Arrangement Showing Typical Feeder Path to Center-Fed Headers

Figure 4-62 shows the new "halo" radiator configuration. This is similar to the original configuration in that the headers are center fed. However, the radiator sections have been clustered closely around the cavity absorber to provide the shortest possible supply and return feeders.

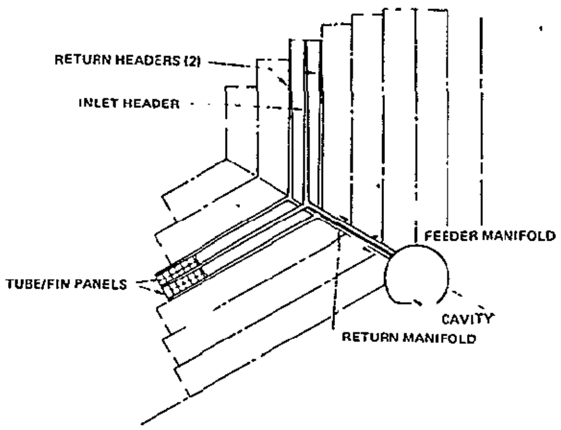

Fig. 4-62. "Halo" Radiator Configuration

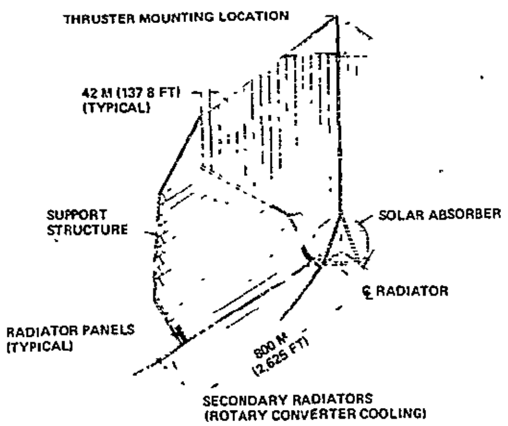

Fig. 4-63. Radiator System, Solar Thermionic SPS

Figure 4-63 shows the radiators for one module (4 GWe nominal) of the solar thermionic liquid cooled power satellite system. The radiators are configured in the "halo" design previously described. Supply and return feeders are as close to the solar absorber as possible to minimize weight. Headers are secured to structure at the solar absorber end. Expansion of the radiator elements due to temperature changes and creep is provided for by expansion joints to the peripheral structure. The secondary radiators below the absorber support trusses are for cooling the rotary converter assemblies (direct current to alternating current converters). This arrangement of the radiators is typical for other power satellite systems such as the Solar Brayton Cycle.

Figure 4-64 shows a typical radiator loop using liquid metal (NaK). This arrangement is for cooling diode collectors in the solar thermionic power satellite.

The liquid metal is carried in a multitude of small tubes contacting the diode collectors. The heated metal is pumped through feeders and headers into

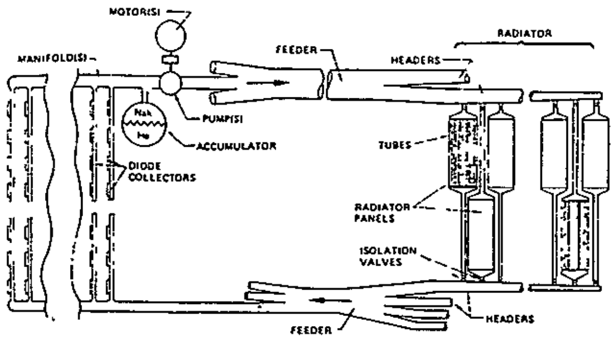

Fig. 4-64. Liquid Metal (NaK) Loop

radiator panels arranged as in Figure 4-63. The cooled liquid is passed through output headers and feeders and over the diode collectors, completing the cycle. An accumulator is used to provide a positive pressure at the pump inlet.

Isolation valves are provided at the inlet and outlet of each panel to enable any panel(s) to be cut out of the cooling loop to prevent loss of coolant in the event of leaks due to meteoroid puncture or other causes.

It has been shown that the motion of parts of the radiator such as headers and panels relative to each other has been considered in the design. The "halo" configuration of the radiator minimizes relative motion of its parts due to temperature differentials.

Another factor for consideration in the radiator design is metal creep due to stress. Figure 4-65 shows the creep (or strain) of Haynes 188 material in 30 years as a percentage of original length, plotted against the constant stress level required to produce the creep, for three different temperatures.

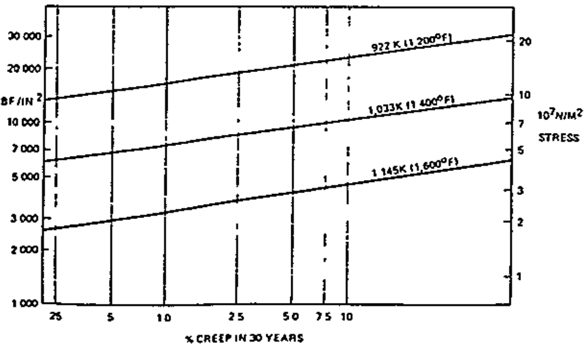

Fig. 4-65. Stress Versus Creep – Haynes 188

Note that a decrease in stress level causes a disproportionate decrease in creep; e.g., a decrease in stress from 7 to 5 x 10^7 N/M^2 at 1033K causes a decrease in the 30 year creep from 7.5 to 0.75 percent.

If the stress level for a creep of 10% in 30 years is reduced by 50% the creep becomes very small—approximately 0.1%.

The radiator headers and feeders are designed for relatively high stress such that significant creep (approximately 10%) occurs over the design life (30 years). Figure 4-66 shows a circular section of feeder or header tube. It should be noted that the circumferential stress is twice the axial stress. The wall thickness of the header or feeder is thus determined by the circumferential stress. However, Figure 4-65 showed that creep decreases at a much higher rate than stress. Thus, the axial creep will be very small compared to the circumferential creep. The graph in Figure 4-66 shows that for a 10% creep the volume of the feeder or header increases approximately 22% in 30 years.

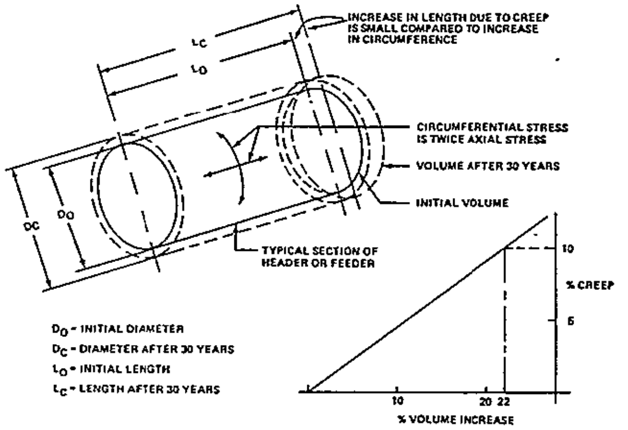

Fig. 4-66. Header or Feeder Volume Versus Creep

This large volume increase is too great for the NaK accumulator to handle. A yearly, or two-yearly, "topping-up" of the system will be required.

4.10.4 Radiator System Optimization

Figure 4-67 is a portion of the interactions diagram of a liquid metal cooled generation system. It represents a math model which is computerized to determine minimum radiator system mass. It is a portion of a large math model of the complete powersat module.

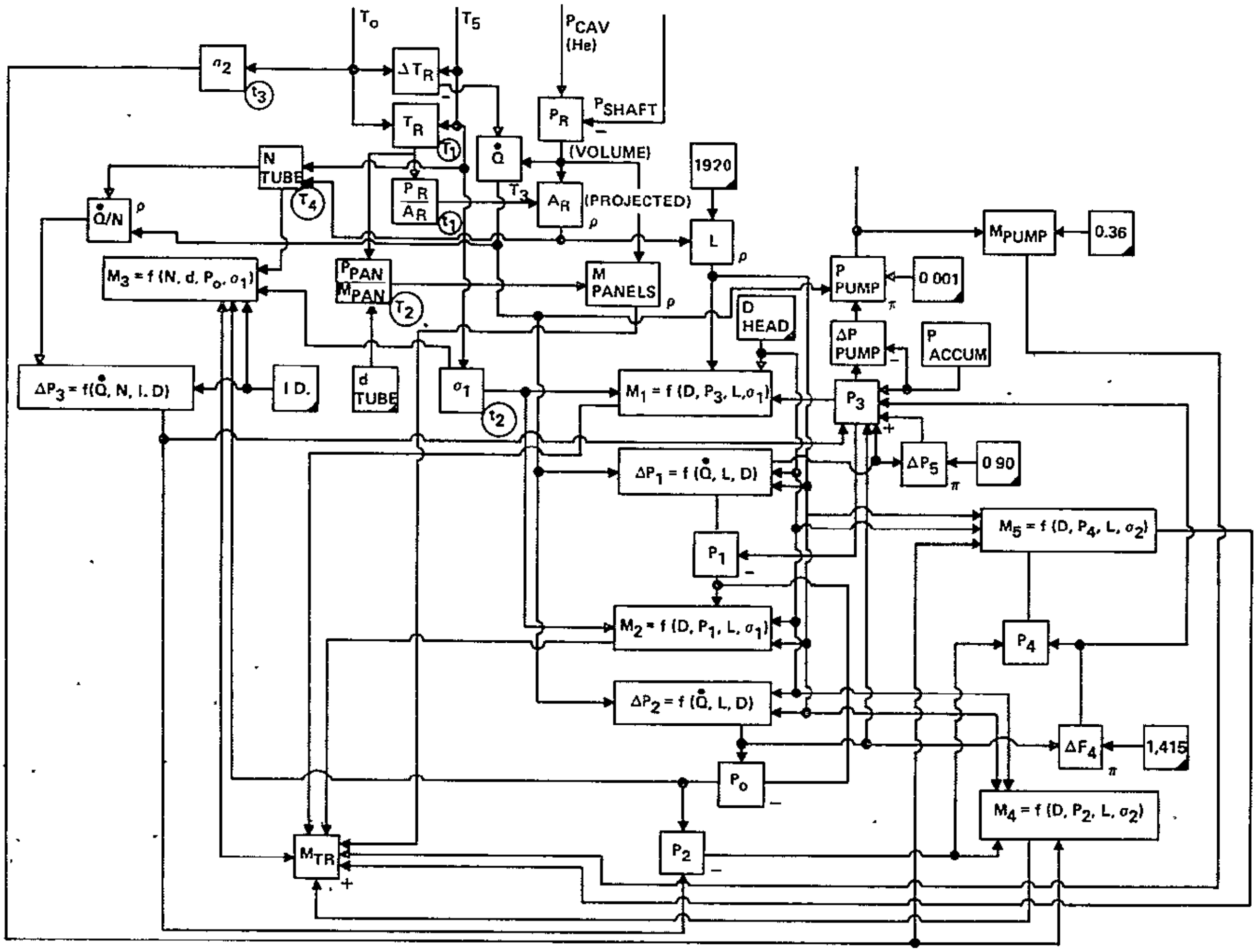

Fig. 4-67. Radiator System Modeling

Each block labeled "t" or "T" represents a parametric relationship. Longer blocks represent equations. The Greek letter rho indicates the ratio of the two inputs; the Greek letter pi indicates product. + and - indicate addition and subtraction. Blocks with the lower right hand corners shaded are independent input variables. Note that the radiator mass is the sum of the mass of all feeders, headers and radiator panels (and the NaK therein) and the associated motors and pumps. Other significant factors include the total power to be radiated and the inlet and outlet temperatures. An independent variable of prime importance is "D HEAD," the diameter of the header manifolds. As this diameter is reduced, the stress in the headers tends to reduce, the area of metal reduces, and the volume of NaK (a significant mass factor) also reduces. However, the pressure drop in the manifolds increases, so that the sum of the pressure drops around the loop ("P_3") increases, tending to increase the inlet pressure, which increases the stress in the manifolds. Higher inlet pressures require more pump power, so that the pumps and associated motors become heavier. More pump power also means more busbar power, so that more solar concentrator, cavity, etc., are required.

Figure 4-68 shows one of the parametric relationships used in the radiator modeling exercise; it was itself derived from computer analysis. It shows the effective temperature; i.e., temperature of an isothermal area equal in size to the radiator which rejects the same amount of energy. T_5 is the radiator inlet temperature; T_O is the outlet temperature.

Figure 4-69 shows total radiator system mass for the range of primary variables judged to be potentially applicable to power satellite usage. For each inlet temperature there is a temperature drop across the radiator (ΔT) which yields minimum mass. Note the drop in mass as inlet temperature is increased up to 1150K (1611°F); beyond this point the trend is less dramatic. This is because the

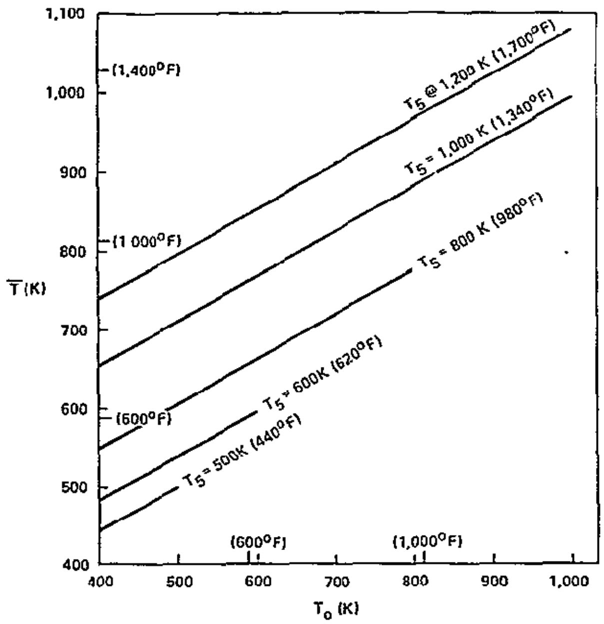

Fig. 4-68. Radiator $\overline{T}$

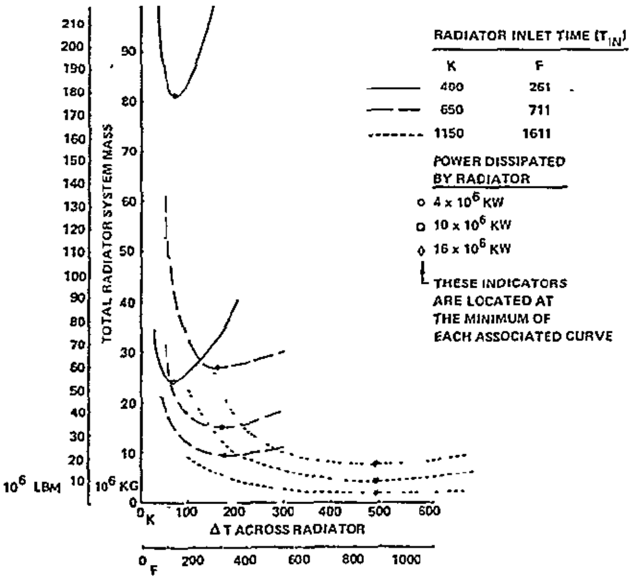

Fig. 4-69. Effect of Significant Radiator Parameters on Total Mass

model includes material strength allowables. Consequently, the wall thickness of the panel tubes and headers must increase as temperature increases to yield the 30 year creep rupture strength.

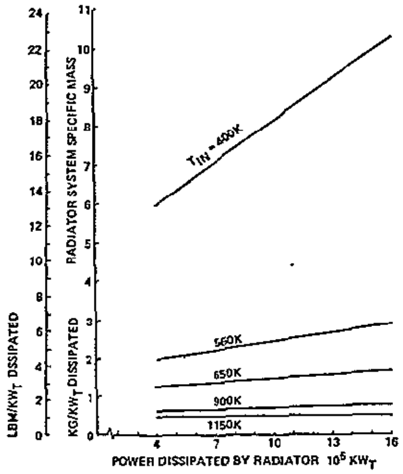

Fig. 4-70. Effect of Power Level on Radiator System Specific Mass (Optimum ΔT)

In Figure 4-70, minimum radiator specific mass is plotted versus thermal power dissipated for five inlet temperatures. The variation with power level may be explained as follows: The single source of the power to be dissipated is located at the approximate center of the radiator. If the power level of a radiator is to be increased, additional panel area must be provided around the periphery (the radiator is a single-plane structure to minimize view factor and meteoroid effects). The headers associated with this added area are obviously longer (and, consequently, more massive) than those associated with an equal area near the center. Thus, radiator specific mass is a function of the power level of the system, and becomes an important factor in the selection of ideal power satellite module size, particularly if the radiator operates at a relatively lower temperature range (and is, consequently, more area-intensive).

4.10.5 Occultation Effects

Solar occultation will occur for varying periods of up to 70 minutes (1.167 hours) duration. During these periods, the NaK radiator is subject to cool down from its normal operating temperature. A transient thermal analysis was conducted to determine whether the NaK in the radiator panel tubing will freeze. The cooling rates with and without circulation were determined. The results (Figure 4-71) indicate a high probability that freezing will occur during longer occultation periods (>38 minutes). (The NaK helium heat exchanger mass was not included which would delay the freezing time somewhat.) At the end of occultation, to thaw the radiator, it is anticipated that the collector facets can be oriented to direct reflected solar energy to the radiator surface. When the NaK has melted the facets would be redirected to the cavity aperture to start up the cycle. However, thawing the radiator is considered as potentially

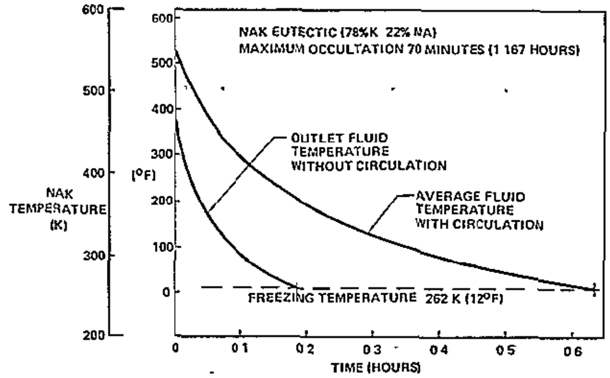

Fig. 4-71. Radiator Fluid Temperature During Occulation

causing "water hammer" and "chugging" (possibly destructive) at startup.

Since the analysis was conducted, a ternary eutectic alloy of sodium, potassium and cesium has been proposed which has a lower freezing temperature, 197K (-105°F), than NaK.

4.10.6 Heat Pipe/Fin Radiator

4.10.6.1 Panel Design Analysis and Modeling

The mass optimized tube/fin radiator with pumped manifolds has a number of inherent drawbacks:

- Vulnerability of tubes to meteoroid puncture.
- Flexing of panels due to differential expansion of input and output headers.
- Freezing of NaK in tubes during occultation.

Due to the number of panels required in the tube/fin radiator design, and transporter space limitations many thousands of welds will have to be performed in orbit. Figure 4-72 shows that 14 welds will be required for each 20m x 20m (65.6 ft x 65.6 ft) area. This includes joining the header sections together.

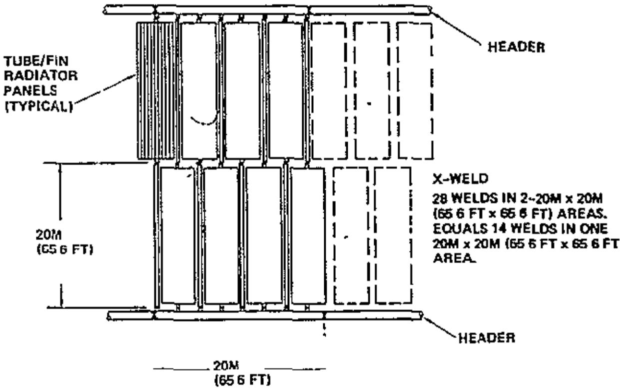

Fig. 4-72. Radiator Welds Performed in Orbit

Because of the inherent drawbacks of the tube/fin pumped manifold radiator a design analysis of a radiator employing heat pipes was performed. Extensive study of heat pipes has been conducted during the last ten years. Although terrestrial applications have been somewhat limited, heat pipe systems have been proposed for several space applications because of the capability for transporting large amounts of heat in a light system. The theory of heat pipes is fairly well established and criteria for heat pipe design are available. Some advantages of heat pipe radiators over tube/fin radiators are:

- Less vulnerable to meteoroid puncture
- Can be designed to avoid differential expansion of members
- Self starting

Each of these items is discussed in this section.

4.10.6.2 Heat Pipe Concept

The basic heat pipe is a closed container consisting of a capillary wick structure and a small amount of vaporizable fluid. The heat pipe employs a boiling-condensing cycle with the capillary wick pumping the condensate to the evaporator as shown in Figure 4-73. The vapor pressure drop between the evaporator and the condenser is very small, therefore the boiling-condensing cycle is essentially an isothermal process.

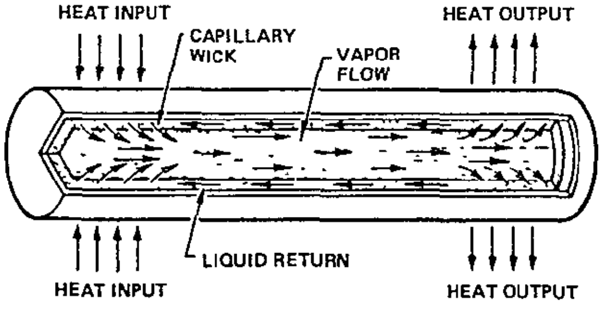

Fig. 4-73. Heat Pipe Concept

Four typical heat pipe cross section options are shown in Figure 4-74. The first is a simple thin walled round tube with a screen wick. The second

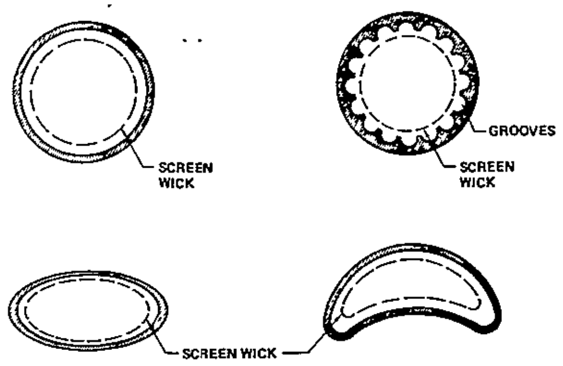

Fig. 4-74. Heat Pipe Options

(right upper) is a round tube with grooves in the wall to enhance return flow of the condensate to the evaporator. The lower two are thin walled tube types whose operation is identical to the first. Under certain design considerations they can provide improved surface contact with the heat source. For example, the lower right design could be attached to a round tube to provide good thermal contact. Both lower types require care in design to ensure that internal pressure will not distort their shape. All types are shown with screen wicks which may consist of one or more layers of screen material. However, with heat pipes employing axial grooves, screen wicks may not be necessary since the grooves serve the purpose of the wick. Screens enhance the capillary pumping pressure of the axial grooves.

The second heat pipe option shown appears to be the most attractive design. The axial grooves provide a relatively low resistance path for liquid flow from condenser to evaporator; the fine mesh screen prevents liquid entrainment at higher heat flux rates and provides small radius menisci for effective capillary pumping.

4.10.6.3 Heat Pipe Working Fluids

The heat pipe's operating temperature is dictated by the selection of its working fluid. Good working fluids should possess the following characteristics: high latent heat of vaporization, high surface tension and low viscosity. In addition, the fluid must be compatible with the heat pipe envelope and a capillary wick. Candidate working fluids for temperatures under consideration for the radiator are water, mercury, cesium, potassium, sodium and lithium.

Figures 4-75 through 4-79 show important characteristics for candidate working fluids.

Fluid	Latent heat of vaporization, cal/gm
Water	540
Mercury	69.7
Cesium	146
Potassium	496
Sodium	1,005
Lithium	4,680

Fig. 4-75. Heat Pipe Fluids: Latent Heat of Vaporization

Fluid	Surface tension n/m (lbf/ft)
Water	0.06 (0.004)
Mercury	0.4 (0.027)
Cesium	0.05 (0.003)
Potassium	0.08 (0.006)
Sodium	0.14 (0.01)
Lithium	0.3 (0.02)

Fig. 4-76. Heat Pipe Fluids: Surface Tension

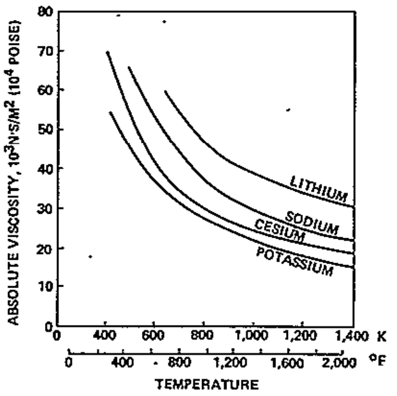

Fig. 4-77. Heat Pipe Fluids: Absolute Viscosity

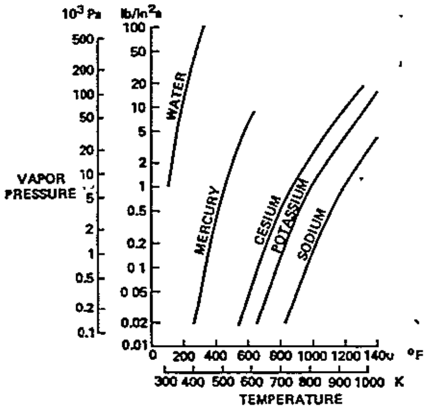

Fig. 4-78. Heat Pipe Fluids: Vapor Pressure

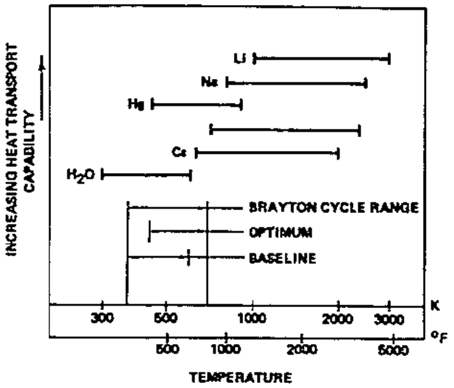

Fig. 4-79. Heat Pipe Fluids: Heat Transport Capability and Temperature Range

4.10.6.4 Heat Pipe Performance

Heat pipe performance used in the radiator system mass analysis was obtained from the design and performance data in Reference (5). A maximum internal pressure of 3 x 10^6 Pa (450 psi), including safety factor, was assumed to size the heat pipes. Diameters of 12.7 mm (0.5") and 25.4 mm (1") have been considered to date. The 12.7 mm (0.5") diameter heat pipe was, however, discarded because of its higher specific mass per QL. Diameters larger than 25.4 mm (1") have not been analyzed yet, because of the difficulty of wrapping the evaporator section of the heat pipe around the manifold. Table 4-30 gives details of the heat pipe designs used in the radiator mass analysis.

Table 4-30. Heat Pipe Data

Approximate temp range K (°F)	Working fluid	Wick type	QL Wm (W-ft)	Dia mm (in)
300 (80) to 600 (600)	Water	Axial groove	4,000	25.4
450 (350) to 900 (1,160)	Mercury	Axial groove	6,000	25.4
800 (1,000) to 2,400 (3,900)	Sodium	Axial groove	8,000	25.4

It should be noted that it may not be possible to obtain the QL in all cases if L is greater than approximately 1.5 m (4.92 ft). If the vapor flow is turbulent (Reynolds number > 3000) the Q x L relationship does not always hold. However the QL given in the table is always obtainable with L = 1 m (3.28 ft) or less.

When the radiator has been mass optimized the heat pipe can be designed to suit the conditions. Its requirements should fall within the QL range shown in Table 4-30.

4.10.6.5 Candidate Materials: Heat Pipe/Fin Radiator

The temperature range of interest for heat pipe radiators is 300K (80°F) (for solar cell cooling) to 1000K (1340°F) (for Brayton cycle cooling). Because of their light weight and relatively high thermal conductivity, candidate radiator fin materials are aluminum and beryllium. Aluminum is suitable for low temperature fins with operating temperatures to 460K (368°F); beryllium, with a melting temperature of 1555K (2340°F), would be suitable for higher temperatures.

For the heat pipes aluminum is not a suitable material since it is not compatible with water or mercury as a working fluid. Water is compatible with stainless steel, copper, nickel and titanium. Stainless steel is the most likely candidate. For mercury, non-austenitic steel, such as 304SST or 347SST can be used. Heat pipes using sodium as a transport medium may be fabricated from stainless steel, nickel or niobium.

Manifolds, headers and feeders for heat pipe radiators can be fabricated from materials suitable for the tube/fin radiators, such as Haynes 188 for temperatures up to 800K (1000°F) and B-66 for greater temperatures.

4.10.6.6 Heat Pipe Radiator Configuration

Physical limitations on the maximum length of heat pipes are imposed by the heat pipe geometry and required heat flux. Heat pipes should be made as long as possible within launch vehicle capabilities to reduce radiator complexity and the total number of panels per radiator.

Capillary pumping forces must equal the sum of the liquid and vapor pressures since the vapor must flow from the evaporator to the condenser and return in liquid form. This imposes a limitation on heat pipe length relative to vapor and liquid passage cross sectional areas. The evaporator section is approximately one fifth the length of the heat pipe and must be in contact with the heat source. In the radiator design the heat source is liquid NaK flowing in a small diameter manifold or header. Contact between the NaK and the heat pipe evaporator imposes a design problem which tends to limit the overall heat pipe length.

Figure 4-80 illustrates a significant heat pipe limitation. "DESIGN A" shows heat pipes radiating in a single plane from a heat source. This plane will be coincident with the ecliptic plane to avoid direct sunlight and to minimize damage from meteoroids. The radiating area in this design is limited by the heat pipe length "L" and is thus limited to approximately $2\pi L^2$. In "DESIGN B" a much larger radiating area is possible since dimension "X" can be made as large as required. The limit to this design will probably be when the pumping power required and the mass of the fluid and hardware outweigh the gain in radiating capability. Thus, the energy to be dissipated by heat source in "DESIGN A" is limited by heat pipe length; this is not true of "DESIGN B."

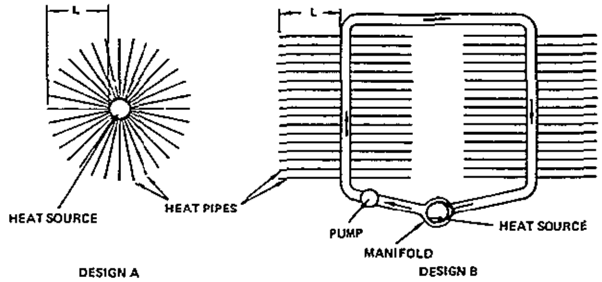

Fig. 4-80. Heat Rejection Area and Capability is Limited by Heat Pipe Length Unless Pumped Manifolds are Used

A liquid metal (NaK) heat pipe/fin radiator concept is shown in Figure 4-81. This concept is similar to the tube/fin radiator concept in that heated liquid metal is pumped from the heat source through feeders and headers into the radiator panels. The cooled liquid metal is returned through headers and feeders to the heat source completing the cycle. An accumulator provides a positive pressure at the pump inlet. The maximum area possible for the heat pipe radiator panel is 20m x 20m (65.6 ft x 65.6 ft) which is the optimum size for transportation to low Earth orbit for assembly. However, this is not necessarily the size for optimum thermal efficiency.

The panel consists of a central header for the radiator fluid (NaK). Heat pipes extend on either side of the header in the same plane as each other. The heat pipes are attached to each other through fins to enhance their heat radiating capability. The radiator panel concept is shown in Figure 4-82.

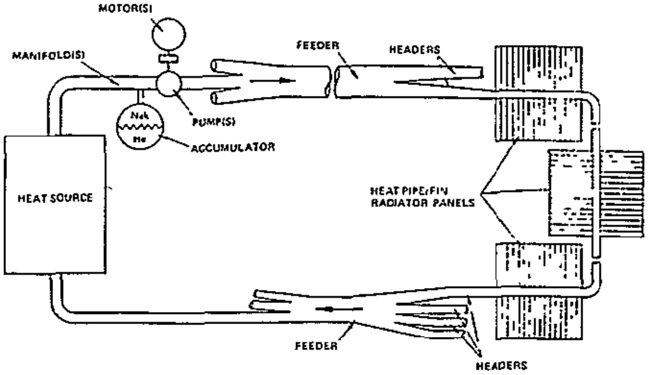

Fig. 4-81. Radiator: Pumped Manifolds/Heat Pipe/ Fin

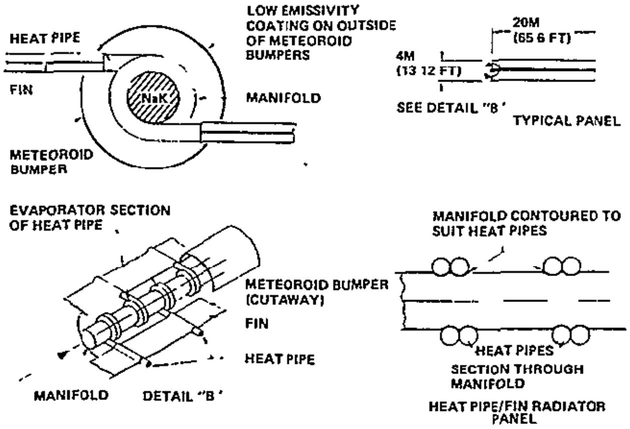

Fig. 4-82. Heat Pipe/Fin Radiator Panel Concept

4.10.6.7 Occultation Effects: Heat Pipe/Fin Radiator

During occultation the temperature of the NaK in the header will drop (flow has ceased). The heat pipe temperature will also have dropped and if properly designed the heat pipe can be made to "stop" while the header temperature is well above the NaK freezing point. The NaK will stay liquid since the header can be well insulated by a low emissivity coating on its meteoroid bumper as illustrated in Figure 4-83. After occultation ends, heat addition to the headers will bring the heat pipes back into operation. Heat pipes with the necessary stop-start characteristics may require the use of a noncondensable gas such as helium in addition to the metallic working fluid.

4.10.6.8 Mass Optimization: Heat Pipe/Fin Radiation For Brayton Systems

Heat pipe/fin panel radiators with pumped manifolds were analyzed to provide radiator system

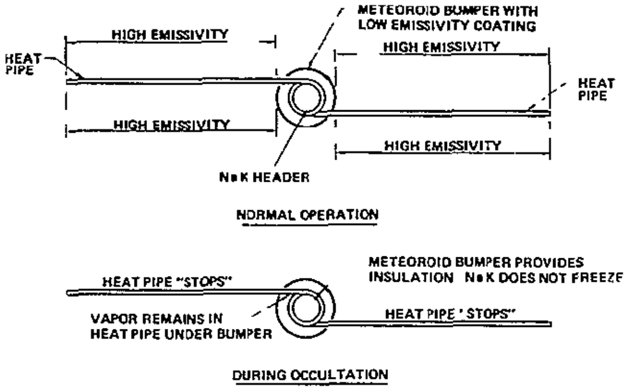

Fig. 4-83. Occultation Effects: Heat Pipe/Fin Radiator

masses for fluid inlet temperatures of 644K (700°F), 820K (1016°F) and 1000K (1340°F). Figure 4-82 shows the basic system configuration used in the analyses.

The heat pipe/fin panels shown in Figure 4-82 are each 20m x 20m (65.6 ft x 65.6 ft) with a central NaK manifold carrying thermal energy from the heat source. Analyses were first performed to determine whether one or a greater number of NaK carrying manifolds would provide minimum system mass. Factors considered were NaK mass flow, system pressure drop, manifold mass, manifold material stress allowable, pump mass and SPS mass penalty for the pump power delta. (The pump mass was assumed to be 0.36 Kg/Kw (0.79 lbm/Kw) and the SPS penalty, 4 Kg/Kw (8.82 lbm/Kw).) No penalty was assessed for additional welds required in space for increasing number of manifolds per panel. However, allowance was made for radiator fin area lost to increasing number of manifolds. Table 4-31 shows the results of the analyses (optimum systems).

Table 4-31. Number of Manifolds Per Panel to Provide Minimum Panel Mass (Constant Section Manifolds)

Fluid inlet temp K ($^{\circ}$F)	Number of manifolds (constant section)	Manifold diameter m (ft)
644 (700)	5	0.25 (0.82)
820 (1,016)	5	0.29 (0.95)
1,000 (1,340)	8	0.22 (0.72)

Analyses of the three systems was then expanded to include the heat pipes, to determine if the optimum for the number of manifolds per panel is also the optimum for heat pipe mass; i.e., would provide minimum radiator system mass. The results show that this is so. The reason for this is a basic characteristic of the heat pipe—the heat transport capability factor, $\dot{Q}L$. This factor is a function of the heat flow, $\dot{Q}$ (watts) and the effective length (L) of the heat pipe.

For the radiator with a fluid inlet temperature of 644K (700°F) each 20m x 20m (65.6 ft x 65.6 ft) panel is required to radiate 3100 Kw. $\dot{Q}L$ for a 25.4 mm (1") diameter heat pipe operating in this temperature range is approximately 6000 WM (19680 W ft). For a panel with one manifold, there are two rows of heat pipes, one on each side. The effective length of each heat pipe is approximately 7.5 m (24.6 ft); therefore $\dot{Q}$ is 0.8 Kw. The number of heat pipes required is thus 1938 per row. For a heat pipe 25.4 mm dia. it is possible to have only 787 heat pipes across a 20m panel. Thus the design with one manifold per panel is not feasible without increasing the heat pipe capability or using more panels, a considerable weight penalty.

If, however, the number of manifolds per panel is increased to 5 for the same radiator, there are 10 rows of heat pipes and the effective length of the heat pipe is approximately 1.5m (4.92 ft). Therefore $\dot{Q}$ is 4 Kw. Only 78 heat pipes per row are required, spaced 256 mm (10") apart. The heat pipes are joined together with fins 0.5 mm (.02") thick.

Radiators for each of the fluid inlet temperatures have been analyzed using the model described above to obtain minimum radiator system masses. The system masses are shown in Table 4-32.

Table 4-32. Heat Pipe/Fin Radiator Mass (Constant Section Manifolds)

Fluid inlet temperature K ($^{\circ}$F)	Radiator system mass kg (lbm)
644 (700)	104.5×10^6 (230.4×10^6)
820 (1,017)	67.1×10^6 (147.9×10^6)
1,000 (1,340)	34.1×10^6 (75.1×10^6)

The system masses for the heat pipe/fin radiators with constant section manifolds are considerably greater than for tube/fin radiators with the same fluid inlet temperatures and radiator power. Figure 4-84 compares the system masses of the two designs in graphic form.

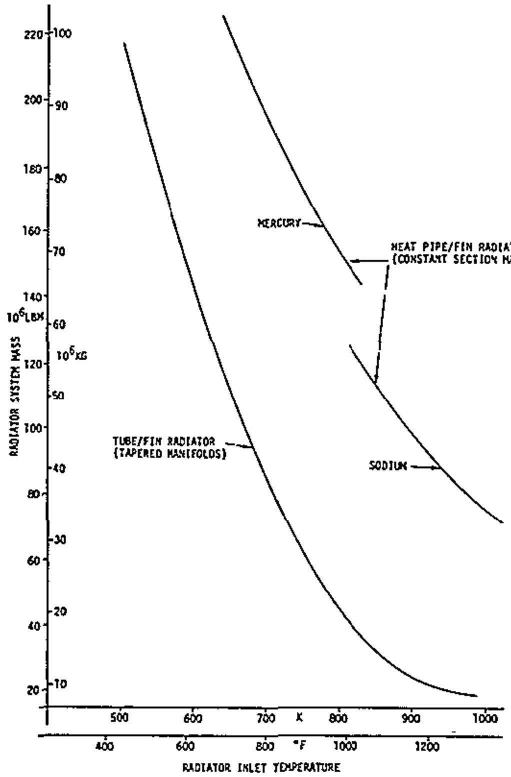

Fig. 4-84. *Radiator Mass Comparison: Heat Pipe (Constant Section Manifolds) and Tube/ Fin (Tapered Manifolds)*

Since, intuitively, it does not seem possible that heat pipes replacing tubes filled with NaK could account for such a large increase in mass, the two systems were broken down into their constituent masses. Figure 4-85 compares the heat pipe/fin radiator (constant section manifolds) with tube/fin radiator for inlet temperatures of 644K (700°F) and 900K (1160°F), and radiator power of 32 x 10^6 Kw/SPS. Each is broken down into three major mass elements: (a) manifolds and NaK and pump mass, (b) panels, and (c) pump penalty mass. It is obvious that the widest difference is in (a). Since the pump mass is comparatively small, the difference must be in the manifolds and NaK. Observation of the design of the two systems shows that the tapered headers (manifolds) of the tube/fin radiator must contribute largely to the lower mass compared to the constant section manifolds of the heat pipe fin radiator. Analyses of radiators with tapered headers as in the tube/fin radiator concept but with the tube/fin panels replaced by heat pipe/fin panels was performed. The radiator design is shown in Figure 4-86.

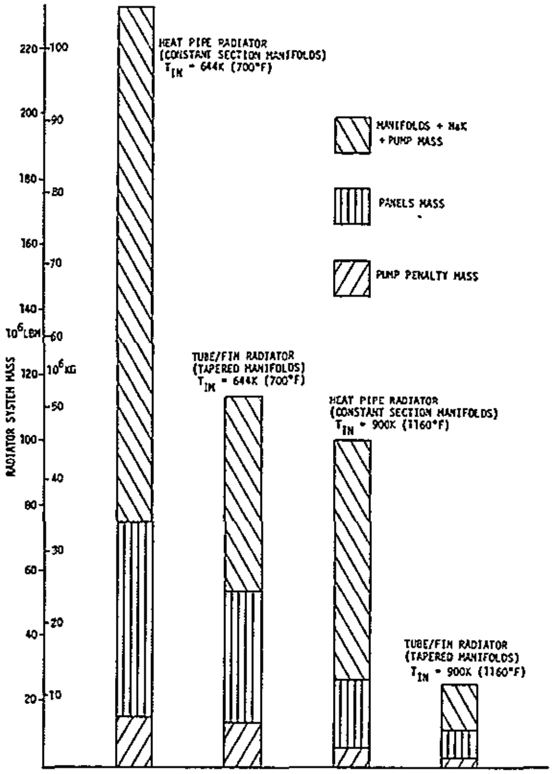

Fig. 4-85. *Effect of Manifold Taper on Radiator Mass*

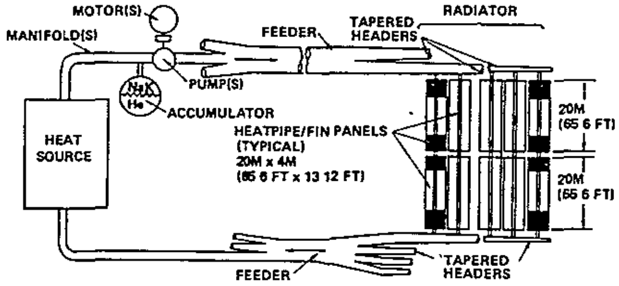

Fig. 4-86. *Heat Pipe Radiator With Tapered Manifolds*

Results of the analyses are shown in Table 4-33. It can be clearly seen that using tapered manifolds instead of constant section manifolds reduces the mass by more than 50%. Figure 4-87 is a graphical comparison of masses of heat pipe/fin radiators and tube/fin radiators, both with tapered manifolds.

Figure 4-87 shows the heat pipe/fin radiator mass estimate as a discontinuous curve. The reason for this is that the various heat pipe transport fluid has a fairly sharply defined operating temperature range. The radiator has been optimized for the appropriate transport fluid for a given inlet temperature.

Table 4-33 Heat Pipe/Fin Radiator Mass (Tapered Manifolds)

Fluid inlet temperature K (°F)	Radiator system mass kg (lbm)
644 (700	45.0×10^6 (99.2×10^6)
820 (1,017)	29.6×10^6 (65.3×10^6)
1,000 (1,340)	15.6×10^6 (34.4×10^6)

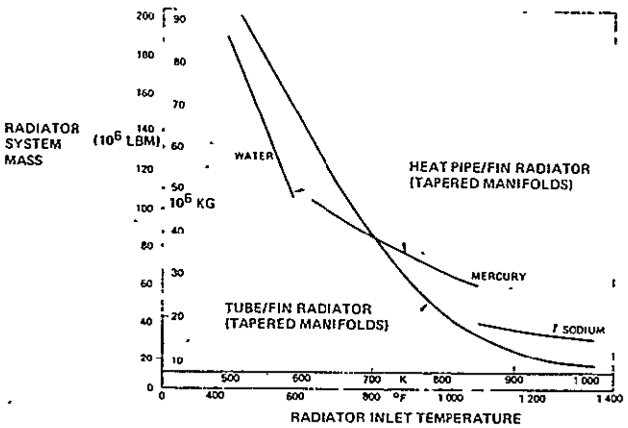

Fig. 4-87. Radiator Mass Comparison: Heat Pipe and Tube/Fin (Both With Tapered Manifolds)

From Figure 4-87 it can be seen that below an inlet temperature of 700K (800°F) the heat pipe radiator has a lower mass than the tube/fin radiator; above this temperature the reverse is true. Thus for heat pipe radiators to compare favorably in mass with tube/fin radiators they must employ tapered manifolds. This means that they will also have some of the inherent drawbacks of the tapered manifold design. Differential expansion of input and output headers will cause panels to flex. Isolation valves will be required at each panel to prevent loss of NaK in the event of a panel manifold puncture. However, the heat pipe radiator panel will be much less vulnerable to catastrophic meteoroid damage than the tube/fin radiator panel since a much smaller part of the panel is carrying NaK. Puncture of a heat pipe would only mean loss of that heat pipe (one of many in a panel); puncture of a tube in the tube/fin panel would mean loss of an entire panel.

4.10.7 Radiators For Solar Cells

Conventional solar cell cooling consists of provision of a black backside coating on the array, plus the heat rejection which occurs from the front of the cell, from and through the cover slip. Since cell efficiency is a strong function of cell temperature, other methods of cell cooling have been investigated. These are of great significance for solar concentration ratios of more than one, and are mandatory for gallium arsenide cells at very high concentration ratios (10 to 1000).

Three radiator concepts have been investigated (see Figure 4-88).

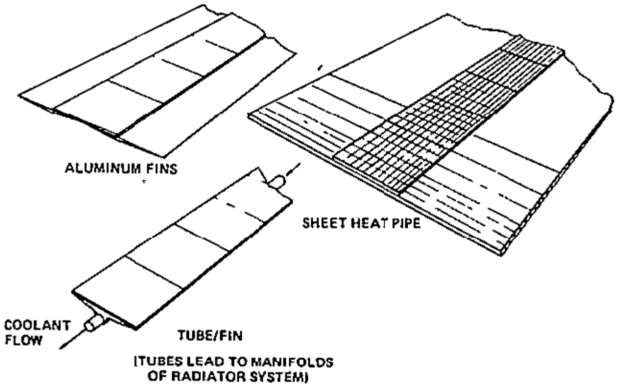

Fig. 4-88. Radiators for Solar Cells

1) Fins. Here individual cell strips, up to approximately 3 cm (1.2 inches) in width would be bonded to aluminum fins which extend beyond the cell edges in the plane of the cells. These fins could possibly be used as current conductors. With this method the cooling area can be approximately four times the cell area.

2) Sheet Heat Pipes. It appears to be possible to fabricate plastic film heat pipes in sheets with a thickness of as little as 300 μm (12 mils). The working fluid will be a hydrocarbon, or possibly water. The cells are bonded to the evaporator zone of the heat pipe. The condenser (heat rejection) region of the heat pipe extends beyond the cell area. The cooling area can be up to ten times the cell area.

3) Pumped Manifold Radiators with Heat Pipe Panels. Individual cell strips are bonded to aluminum fins which conduct heat into a coolant line. The lines from a number of cell strips are brought together into manifolds which carry the hydrocarbon or water fluid to the radiator panel area. Pumping power is parasitic on the cell output. This method can provide heat rejection areas hundreds of times greater than the cell area.

System size effects must be considered. For example, if heat pipes are to be used without pumped manifolds a maximum practical heat pipe length of ≈ 10m (33 ft) limits the radiator area to 628m^2 (2060 ft^2). At a cell and radiator temperature of 333K (140°F), the heat rejection from the radiator is only about 0.63 kW/m^2 (0.06 kW/ft^2), limiting the total heat rejection to approximately 400 kW. This would limit the module which this radiator cools to an output of under 200 kW$_e$. The associated solar collector would be only approximately 500m^2 (5380 ft^2), and at least 160,000 such modules would be required for a 20 GW ground output SPS. The solar collectors are too small to use the steerable reflector facet concept, since the facets would be under 0.5m (20 inches) on a side. The mass of the facet pointing servomechanism would contribute to an overall specific mass in the range of 2 to 3 Kg/m^2 (0.4 to 0.6 lbm/ft^2). This is in contrast to the 0.24 Kg/m^2 (0.05 lbm/ft^2) of the large steerable facet concentrators used with the Brayton concept. Thus a heat pipe radiator without pumped manifolds appears to be limited to use with low to moderate (up to ≈ 200) solar concentration ratios. Of course linear (two dimensional) solar concentrators of any length may be envisioned, so that large power levels may be handled with heat pipe radiators without manifolds. These considerations are included in the modeling effort to select a solar concentration ratio and cooling system (if any) for use with photovoltaics.

REFERENCES

1) NASA TMX-64627 "Space and Planetary Environment Guidelines for Use in Space Vehicle Development," Nov. 15, 1971.

2) McGraw Hill "Space Exploration."

3) NASA CR-54201, "Meteoroid Protection For Spacecraft Structures."

4.11 POWER DISTRIBUTION

4.11.1 The Problem

The baseline microwave power transmitter requires 16.17 GW at the interface to achieve 10 GW on the ground, as shown in Figure 4-89.

With 20,000 volts direct current to the amplitrons, the required current is 808,500 amperes. In photovoltaic systems, power is generated over the entire SPS; in thermal engine systems power generation is more localized. In both cases power distribution over distances exceeding 15 km (9.3 mi.) is required (in nuclear SPS types the generators can be located relatively near the transmitters). Also, in solar SPS types the transmitter must constantly face the receiver on Earth while the power generation system faces the sun; thus either slip rings or a rotary transformer are required to pass the power.

Item	Efficiency	Power level, GW
Ground output	—	10.00
Switching, pilot transmitter, etc.	0.99	10.10
AC step-up	0.99	10.20
DC to AC conversion	0.96	10.63
DC distribution in rectenna	0.99	10.74
RF to DC conversion (average)	0.88	12.20
Rectenna size relative to beam	0.94	12.98
Atmosphere	0.99	13.11
Phase front control	0.95	13.80
DC to RF conversion	0.88	15.68
Distribution on transmitter	0.97	16.17
	0.62	

Fig. 4-89. Microwave Power Transmission Efficiency Chain

4.11.2 Conductors

In a 5 GWe ground output powersat approximately 8 GWe at 20,000 vdc must be delivered to the antenna; twice this is required for 10 GWe ground output. If 8 GWe is moved over two conductors the current is 400,000 amperes. In Figure 4-90 minimum system mass is determined for three material temperatures. This analysis technique works for any "unit length"; one centimeter (0.4 inch) was used. The three conductor sections necessary to dissipate the I^{2}R losses for the three temperatures are shown. 500K (440°F) is probably the highest practical temperature for aluminum structure. The principle shown is to select that conductor diameter which causes the total SPS mass to be a minimum.

At the bottom of Figure 4-90 is shown the baseline structure (size based on mechanical loads alone). This structural element can carry the 382,000 volts baselined for a.c. distribution without overheating.

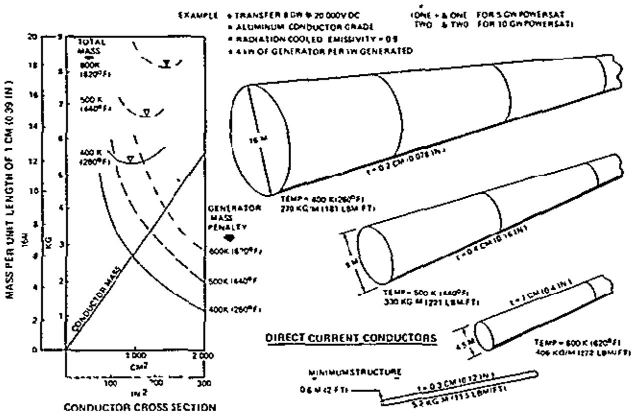

Fig. 4-90. Moving Large D.C. Currents

4.11.3 AC Versus DC Trade

Figure 4-91 shows how the total efficiencies and specific masses of the two candidates were compared. Note that the generators and transformers require cooling. This is because their inefficiencies dictate that a certain amount of heat energy will be produced (if a generator is 98% efficient it must dissipate 2% of the energy which enters it). Maximum generator and transformer operating temperatures are forecasted to be 400K to 410K (260°F to 278°F). Radiant heat dissipation at such temperatures is only approximately 1.3 kW/m^2 (0.12 kW/ft^2). Consequently the surface area of the generators and transformers are not sufficient to dissipate their waste heat, and additional radiation area is required. The specific mass of these radiators (mass per power input to generator or transformers) is included in Figure 4-91.

Note the penalty on structural mass associated with d.c. distribution, and that there is also an efficiency (I^2R) loss. A.C. distribution was selected on the basis of its slightly lower overall mass and slightly higher efficiency. Note, however, that if a higher voltage transmitter (e.g., 40,000 v.d.c.) were involved that the trade would probably switch to d.c as the preferred approach.

Item	AC System (400 to 600 Hz)				DC System			
	Volts	Specific Mass kg/kW	Specific Mass lbm/kW	Efficiency	Volts	Specific Mass kg/kW	Specific Mass lbm/kW	Efficiency
Generators	60 kV	0.150	0.330	0.980	20 kV	0.211	0.464	0.980
Cooling		0.080	0.176	–		0.080	0.176	–
Control	–	0.115	0.253	0.995	–	0.135	0.297	0.995
Step up transformers	382 kV	0.100	0.220	0.995	–	–	–	–
Cooling		0.020	0.044	–				
Transmission through frame (Penalty above basic structure)	382 kV	–	–	0.999	20 kV	0.538	1.184	0.933
Rotary step down transformer	20 kV	0.125	0.275	0.993	–	–	–	–
Cooling		0.028	0.062					
Slip ring/clutch assembly	–	–	–	–	20 kV	0.025	0.055	0.999
Cooling						0.004	0.004	
Power conversion and filter	20 kV	0.140	0.308	0.946	–	–	–	–
Cooling (maximum 1% ripple)		0.216	0.475	–				
System		0.974	2.143	0.910		0.993		0.909

1) Thermionic systems require motor to drive generator, specific mass = 0.24 kg/kW (0.53 lbm/kW). Efficiency is 0.970, to bring AC efficiency to 0.883, DC efficiency to 0.882.

2) Nuclear systems have generator systems rigidly attached to transmitter, and do not require rotary transformers or slip rings. This brings AC efficiency to 0.962 (0.933 with thermionics) and DC efficiency to 0.910 (0.883 with thermionics)

Fig. 4-91. A.C. Versus D.C. Distribution

5.0 SYSTEM OPTIMIZATION AND CONFIGURATION DESCRIPTION

5.1 SYSTEM OPTIMIZATION

5.1.1 Approach

Section 4 described significant individual subsystems and how analyses of those subsystems led to their parametric description. In this section the generation of total SPS configurations by determining optimum values for the subsystem parameters will be described. In general the optimization was for minimum SPS mass, since transportation cost is such a dominant factor in SPS (transportation of a 100,000 metric ton SPS to GEO may cost approximately $8 billion 1976 dollars). An exception to the mass optimization approach was taken with the photovoltaic configurations, wherein cell cost can be so significant; photovoltaic SPS systems were optimized for minimum cost per kW output, including the effects of transportation costs.

Many optimizations were accomplished by hand calculations or simple computer programs. However, the most significant optimization tool was the Integrated Sensitivity and Interactions Analysis, Heuristic (ISAIAH) program developed by G. R. Woodcock as an IR&D activity. ISAIAH can interact up to 100 dependent and 30 independent variables to obtain an optimum combination of values for the independent variables. Dependent variables are input as tables (one, two or three dimensional); summation product or ratio functions, or as FORTRAN expressions. ISAIAH is executed on the IBM 370; plots are outputted on request.

5.1.2 Iteration

In some cases up to three iterations were used to derivation final, optimized configurations. Initial design assumptions were used to set subsystem parameters. After system (SPS level) optimization the regions of operation of the subsystems became more closely known. This allowed more detailed definition of the subsystem for the region of interest. This process was continued, guided by the goals of producing lighter, cheaper, more practical configurations. In several cases known reserves of certain materials were not sufficient to accomplish the baselined SPS program, so that alternative materials were required, causing a configuration adjustment.

5.1.3 Alternative Systems

Table 5-1 (a repeat of Table 3-1) gives the systems to be described in this section.

Table 5-1. Alternative Power Systems

Concept	Energy Source	Energy Converter
1	Solar	Direct Radiation Cooled Thermionic
2	Solar	Liquid Cooled Thermionic
3	Solar	Closed Brayton Cycle
4	Solar	Thermionic Brayton Cascade
5	Solar	Silicon Photovoltaic
6	Solar	Gallion Arsenide Photovoltaic
7	Nuclear	Thermionic
8	Nuclear	Closed Brayton Cycle
9	Solar (Power Transfer)	Ground-Based Solar Power Plants

The basic principles of each power system are explained in Section 3.1.

5.2 SOLAR DIRECT RADIATION COOLED THERMIONIC (CONCEPT 1)

The thermionic diode subsystem as developed by Thermo Electron Corporation is described in Section 4.6. The emitter temperature of 1800 K (2780°F) was selected as being the practical upper limit (30 year life) for molybdenum. (Tungsten would have yielded higher performance, however the known reserves of tungsten are insufficient for the baselined SPS program). The next question is what radiator temperature to use. High radiator temperature allows more heat rejection per unit area (per T^4) and a resultant trend to a lighter radiator. However, a high temperature radiator reduces the temperature differential across the thermionic diode so that the system efficiency is reduced. This tends to increase the number of diodes required, solar collection area, etc., and the amount of heat to be rejected by the radiator. (Refer to Figure 4-19.) The selected collector temperature was 1000 K (1340°F); the effective temperature of the heat pipe radiator is 900 K (1160°F).

As explained in section 4.6, the voltage output of a diode panel is 129 v.d.c. (150 v.d.c. is the approximate upper limit for electrical insulation at the temperatures of the diode). 382,000 v.a.c. is baselined for power distribution. A power converter is required to affect the voltage step-up. The efficiency and specific mass of power converter are a function of their power level. Thus it must be decided how many 20x20 m (65.6 ft.) power panels are to feed each power converter. Figure 5-1 shows the basic diode panel.

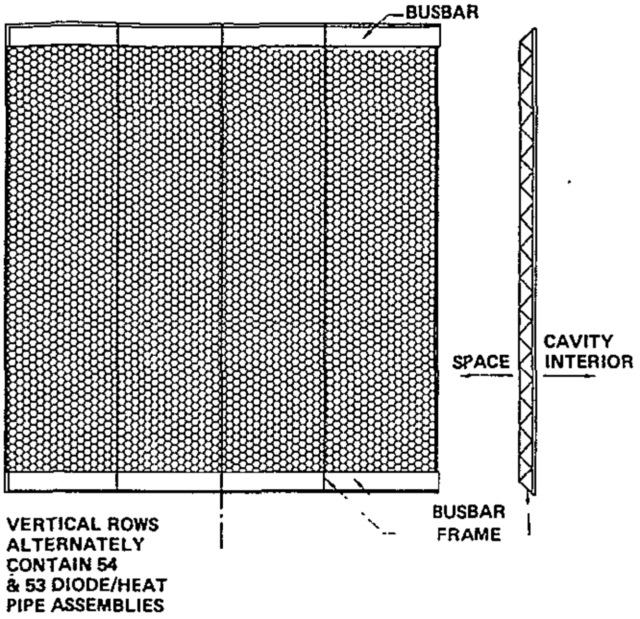

Fig. 5-1. Diode Panel (Heat Pipe Side)

A power converter could be located on this panel; however, the radiator for this converter would displace approximately one fourth of the diodes. The converter power rating would be approximately 2.6 MW. The combined efficiency of the d.c. to a.c. converter and its associated transformer would be approximately 0.92 at this power rating; the specific mass would be about 0.35 kg/kW (0.77 lbm/kW). By using four diode panels per power converter panel, as shown in Figure 5-2, a larger (14 MW) converter is possible.

The waste heat rejection from a 14 MW converter/transformer is just appropriate to a 20x20 m (65.6 ft) panel at a heat rejection temperature of 405 K (269°F). Also, four diode panels may be grouped around such a panel quite conveniently. At a 14 MW rating the power converter assembly has an efficiency of 0.96 and a specific mass of 0.29 kg/kW (0.63 lbm/kW).

Since the currents are so high good busbar design is required to achieve lightweights. Flat, high area busbars reject I^2R losses well if given a high emissivity coating. Insulation is required beneath the busbars to shield them from the high temperature of the cavity interior. The insulation used is "Multi-Foil" (see Section 4-6). A busbar width of one meter (3.28 ft.) was selected as a good compromise between obtaining sufficient radiator area and the concommittant enlargement of the cavity absorber, insulation mass increase, etc. On the diode panel the current handled by the busbar is a maximum at the connection to the power converter panel and a minimum at the other edge of the diode panel (the left side of Figure 5-1).

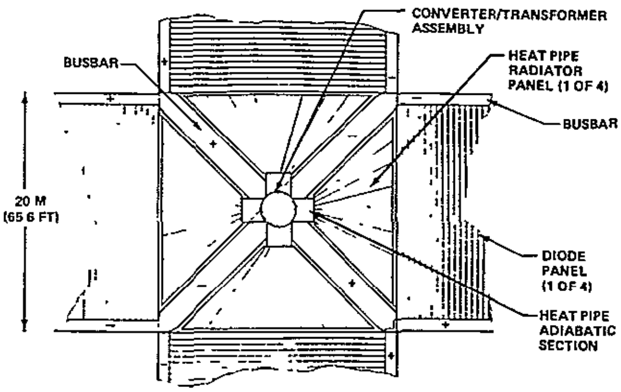

Fig. 5-2. Power Converter Panel (For Four Diode Panels)

This current distribution makes tapering the thickness of the busbar a practical method of mass reduction. Aluminum proved to yield a lighter conductor than copper when each was optimized to yield minimum mass for the busbar itself plus the SPS penalty from the I^2R loss in the busbar (this penalty was taken as 8.31 kg/kW of I^2R dissipation). The optimum aluminum busbar temperature is 450 K (350°); the optimum copper temperature would be 700 K (800°F). The aluminum busbar should be 1.17 cm (0.46 in.) thick at the point of connection to the diode panel; it may be only 0.56 mm (0.022 in.) thick at the other end. The busbars are 2 m (6.56 ft.) wide and 1.17 cm (0.46 in.) thick on the power converter panel. A circuit for the busbars of four diode panels and a power converter panel is given in Figure 5-3.

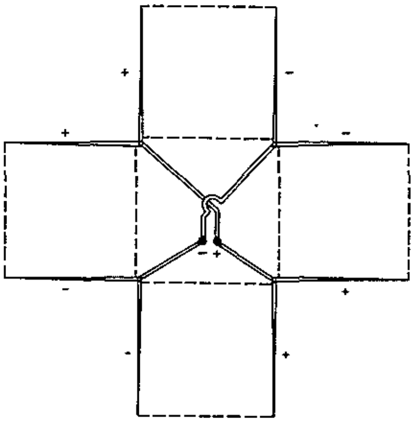

Fig. 5-3. Busbar Circuit

Masses of the diode assembly and the associated heat pipe radiator were given in Tables 4-5 and 4-6. Figure 5-4 gives masses for the three types of panel used to comprise the cavity absorber.

Diode panels			Power conversion panels			Blank panels		
Item	KG	LBM	Item	KG	LBM	Item	KG	LBM
Insulation	40	88	Insulation (multifoil)	1 600	3 527	Insulation	1,600	3,527
Diodes *	21,910	65,944	Busbars (alum)	1,770	3 902	Frames	1,200	2 646
Busbars	750	1,653	Supports, fittings	170	375		2,800	6,173
Frame	1 300	2,866	Rot conv/trans	4 010	8 640			
	24,000	52,910	Heat pipes	1,700	3,748			
			Control	300	661			
			High volt bus	100	220			
			Frame	1,300	2,866			
				10,950	53,220			

* With interelectrode busbars and heat pipes

Fig. 5-4. Panel Masses

The diode and power converter panels have been explained; the blank panels are necesary as fillers to complete the cavity absorber as shown in Figure 5-5.

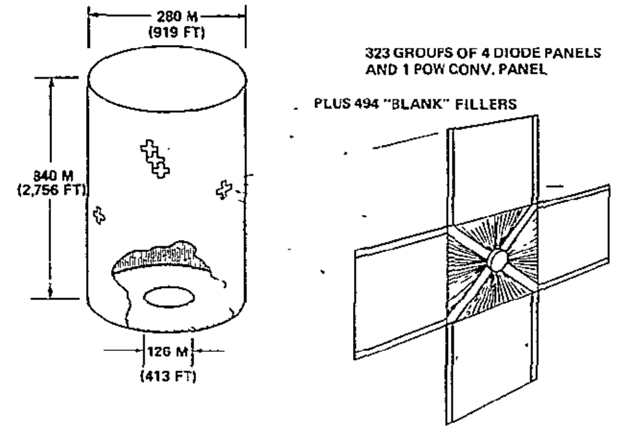

Fig. 5-5. Cavity Absorber is Formed From Panels

A cylindrical cavity was selected for the thermionic SPS for these reasons:

1. There is apparently no impact on efficiency relative to a sphere.
2. There is no point in placing diodes on the bottom of the cavity since the solar concentrator would block much of the view to space of the heat pipe radiators. A tall cavity (large ratio of length to diameter) minimizes the bottom area.

Figure 5-6 shows one module of the thermionic SPS. It is sized to provide 4.37 GW to the main bus (a total of 17.49 GW). The output of the rotary transformer would be 17.37 GW; the rectifier/filter assemblies on the transformer will accept this power level. This 16.43 GW is available under the optimum illumination conditions (solstices); at the equinoxes the output falls to 16.17 GW which is the minimum required to provide the 10 GW ground output (see Figure 4-89, the microwave efficiency chain).

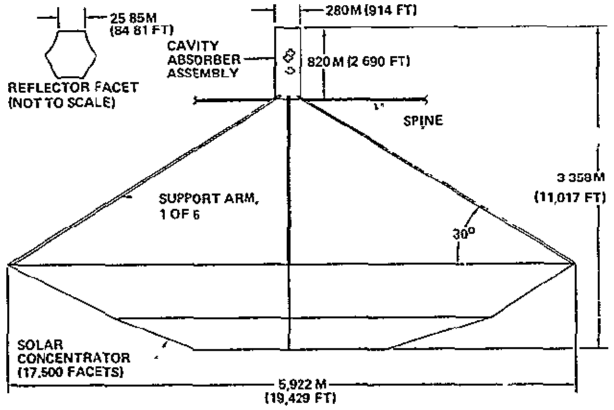

Fig. 5-6. Thermionic SPS Module

Per Section 4.5, the optimum reflector facet count is 17,000. The "spine" is a triangular, insulated structure carrying the 382,000 v.a.c.

Figure 5-7 is a general arrangement of the SPS configuration. It can be seen that the central spine stiffens the structure and provides a convenient path for power transfer. This spine would be parallel to the polar axis of the earth as the satellite flies "perpendicular to the orbit plane" (POP).

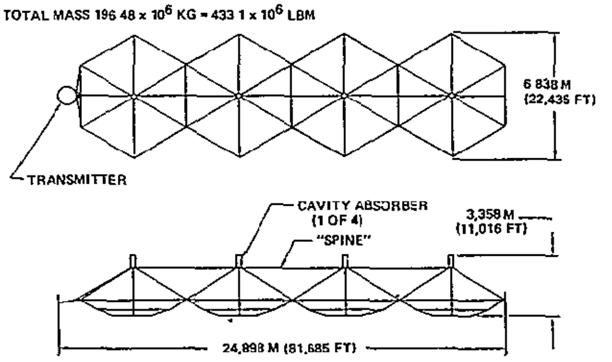

Fig. 5-7. Thermionic SPS Configuration

Some additional parameters relative to this configuration are given in Figure 5-8.

Ground output	10 GW
Orbit busbar	17 43 GW
Orientation	Perpendicular to orbit plane
Number of modules	4
Total number of diodes	17,473,008
Total number reflectors	70,000
Total number power convertors	1,292
Geometric concentration ratio	2,450
Cavity area ratio	68
Interior cavity temperature	1,800K (2,780°F)
Diode heat pipe temperature	900K (1,160°F)
Diode efficiency	0.24

Fig. 5-8. Thermionic SPS Parameters

Table 5-2 is a mass statement for the 10 GW ground output SPS.

Table 5-2. Thermionic SPS Mass Statement

Solar concentrators	10^6 kG	10^6 LBM
Facets	8.51	18.76
Support structure	20.69	45.61
	29 2	64.37
Solar absorbers		
Blank panels	5.52	12.17
Power converter panels	14.16	31.22
Diode panels	124.04	273 46
	143.72	316.85
Rotary transformer and radiator	2.30	5.07
Rectifier filter and radiator	5.41	11.93
Attitude cont., station keep	2.73	6.02
Transmitter	11.90	26.23
Total	196.84	433.95

Although configuration variations were not analyzed, it is possible that reconfiguration of the diode heat pipe radiators could result in a lighter SPS. By changing to a heat pipe configuration similar to that shown in Figure 5-8 the diodes would be brought closer together allowing a reduction in interelectrode busbar length. Examination of Figure 4-21 can lead to a calculation indicating that the total interelectrode busbar mass is 49.6×10^6 kg (1.09×10^8 lbm) which is approximately 25% of the total SPS mass. Thus there is some possibility that reconfiguration might effect a net thermionic SPS mass reduction of approximately 20% below that given in Table 5-2.

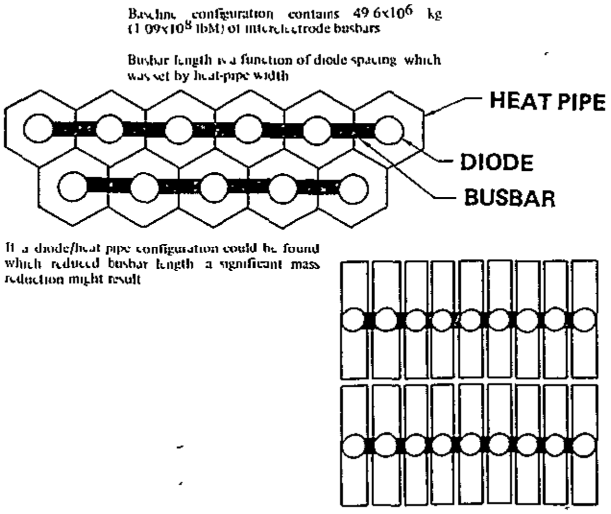
Baseline configuration contains 49.6×10^6 kg (1.09×10^8 lbM) of interelectrode busbars

Busbar length is a function of diode spacing which was set by heat-pipe width

If a diode/heat pipe configuration could be found which reduced busbar length a significant mass reduction might result

Fig. 5-8. Reduction of Interelectrode Busbar Mass

5.3 SOLAR LIQUID COOLED THERMIONIC (CONCEPT 2)

In this concept diode collector cooling is accomplished by a separately located radiator system. Such a radiator would be similar to that used in the Brayton systems (heat pipe panels with pumped manifolds).

By cooling the diode collectors with an active liquid metal loop that can in effect be coupled to a greater radiator area than is practical with fins attached to the collectors, achieve a greater temperature differential across the diode, and therefore obtain higher efficiency.

Figure 5-9 shows the approach taken to interface the liquid radiator to the individual diode collectors.

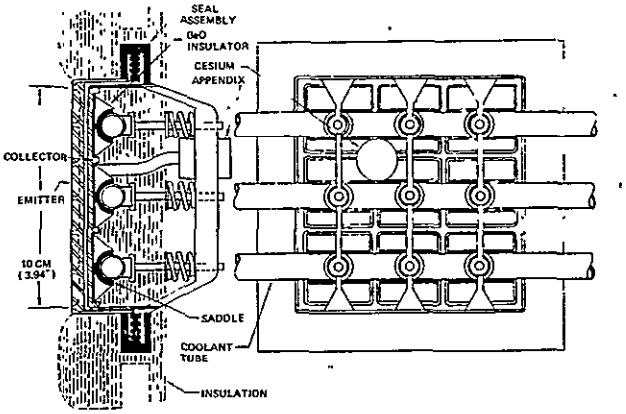

Fig. 5-9. Diode/Radiator Interface

One problem with this concept is that the diode collectors must be electrically isolated; thus the coolant tubes require electrical insulation. However, good thermal conductivity is also required. Beryllia (BeO) saddles provide the electrical insulation. Spring systems (kept cool by being outside the insulation batting) provide pressure to hold the diode collector, the saddles and the NaK tubes in contact. Aluminum is used as a contact improver; over the 30 year design life the NaK tubes will increase in diameter due to creep, the aluminum spacer should yield to accommodate this growth.

The tubes shown in Figure 5-9 would be brought together in manifolds which deliver NaK to the pump system, as shown in Figure 5-10.

The diagram shows a liquid metal (NaK) heat pipe/fin radiator concept. Liquid metal is pumped from the heat source through feeders and headers

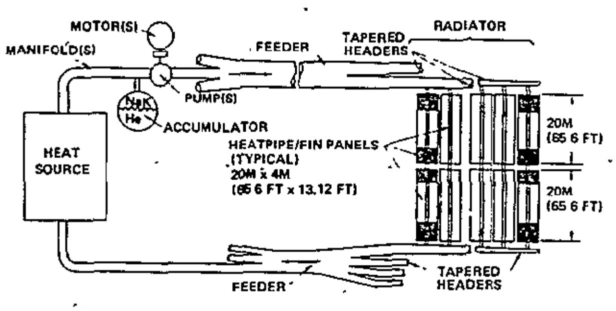

Fig. 5-10. Radiator Concept

into the radiator panels. The cooled liquid metal is returned through headers and feeders to the heat source completing the cycle. An accumulator provides a positive pressure at the pump inlet.

The heat pipe/fin panels are 20m x 20m (65.6 ft x 65.6 ft). A NaK header through the center of the panel carries thermal energy in the form of sensible heat. Meteoroid penetration of a heat pipe causes that pipe to stop operation, although it continues to act somewhat as a fin for adjacent heat pipes. Since the header fluid is isolated from the heat pipe fluid, heat pipe penetration does not cause loss of NaK. Leak detectors, isolation valves, and control systems associated with meteoroid punctures will not be required.

A most critical parameter to be determined was the optimum radiator temperature (hence collector temperature) to be used with the baseline molybdenum emitter temperature of 1800 K (2780°F). This and other critical parameters were addressed by parametric modeling and computer optimization. Figure 5-11 shows the systems interactions model (the interdependencies of primary system elements). Parametric expression for each of these variables were coded for automatic processing by the ISAIAH (Integrated Sensitivity and Interactions Analysis–Heuristic) program. The objective function was minimum system weight.

Several features of the model should be noted:

1. The radiator weight is a function of its temperature, to account for the change in material allowables with temperature.

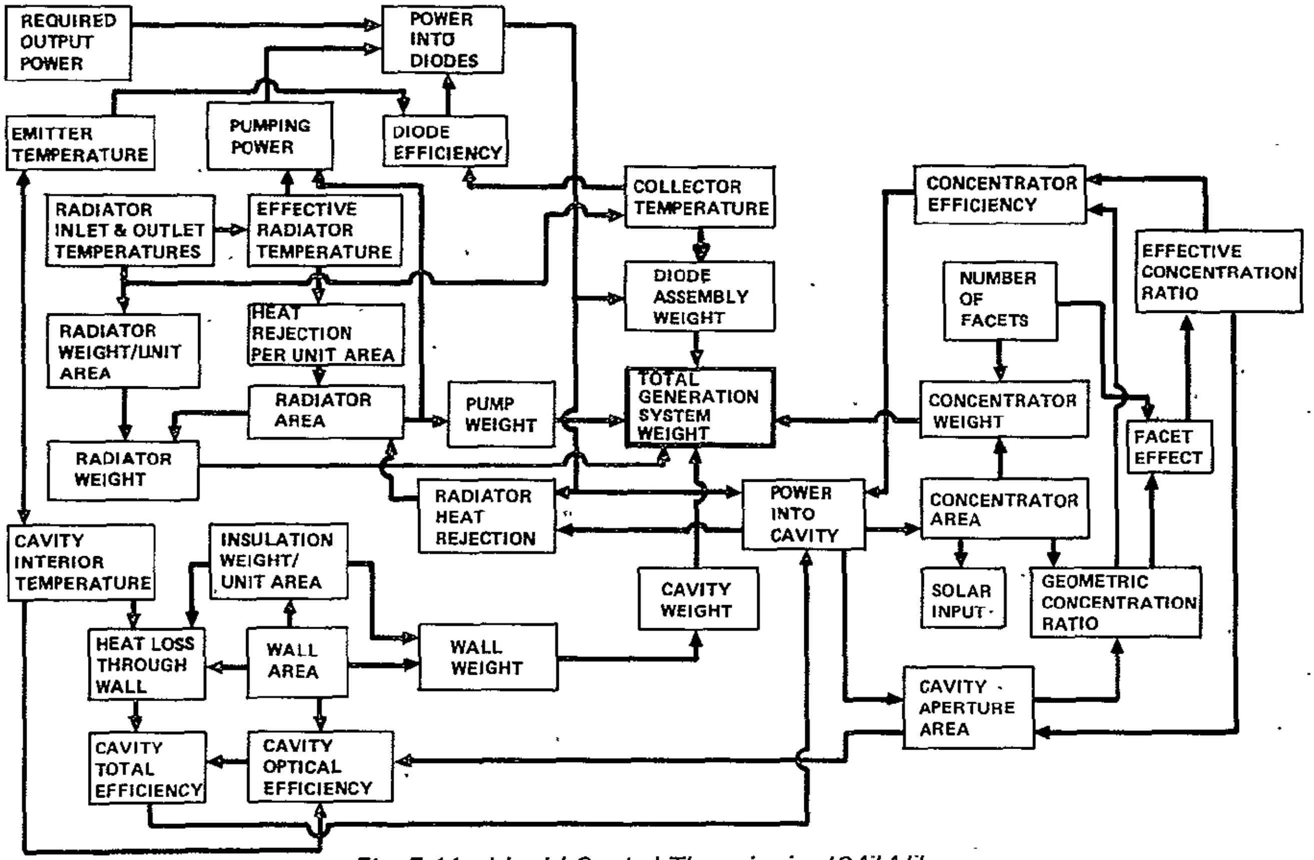

Fig. 5-11. Liquid Cooled Thermionics ISAIAH Model

2. Solar concentrator efficiency and mass are a function of the number of reflector facets used.

3. The total weight includes the solar concentrator, cavity absorber, diode assembly, radiator and radiator pumps.

The optimum radiator temperatures were: inlet, 868 K (1102°F), outlet 388 K (238°F). The "effective" radiator temperature (uniform temperature of an area equal to that of the radiator having the same emissivity and which rejects any equal power) is 589 K (600°F). Some diode collectors will be along their NaK tubes such as to be near the radiator inlet and will consequently be at approximately 900 K (1160°F); at the other end (the radiator outlet) the collector temperature will be only 405 K (269°F). The average collector temperature will be 605 K (629°F).

Table 5-3 is a mass statement for the optimized configuration. The total busbar power produced by this SPS is 17.5 GW; 0.64 GW of this is the power required to pump the radiator system. This requirement is not offset by the slightly higher diode efficiency (when comparing this system to the direct radiation cooled variant). However, the diodes can be placed quite close together, due to the remote radiator system, allowing short inter-electrode busbars. Consequently 17,000 diodes are grouped on a 20x20 m (65.6 ft.) panel. In order that the power conversion panels may be passively cooled without a remote radiator system, only one diode panel may be used per power conversion panel (to keep the dissipation within the capability of the area of the power conversion panel).

Table 5-3. Liquid Cooled Thermionic SPS Mass

	10^6 KG	10^6 LBM
Solar Concentrators		
Facets	8.51	18.76
Support Structure	20.69	45.61
Radiator and Pumps	116.00	255.73
Solar Absorbers		
Blank Panels	1.80	3.97
Power Conversion Panels	14.16	31.22
Diode Panels	135.74	299.25
Rotary Transformer and Radiator	2.30	5.07
Rectifier Filter and Radiator	5.41	11.93
Attitude Cont. & Station Keeping	2.73	6.02
Transmitter	11.90	26.23
Total	319.24	703.80

This SPS concept is seen to be far more massive than the direct radiation cooled thermionic SPS; it was consequently not pursued in the study extension phase.

5.4 SOLAR CLOSED CYCLE BRAYTON (CONCEPT 3)

Derivation of parametrics for the turbomachines, solar concentrators, radiator and cavity absorber.

SYSTEM DESCRIPTION: THERMAL ENGINE SPS

The basic configuration of this SPS is composed of four power generating modules and one microwave transmitter. The power generating modules consist of solar concentrator assembly of 16,500 metallized plastic film reflectors supported by a graphite-epoxy framework. The cavity absorber assemblies located at the focal points of these concentrators are hollow spheres 160 meters in diameter; the apertures are 100 meters in diameter. The solar concentrators are hexagonal in form with edge members 2482 meters long.

Figure 5-12 shows a single solar Brayton power module; the cavity absorber is held at the focal point of the concentrator by six support arms. The radiator is shown inclined by 11.75°. This positions the radiator midway in the apparent arc traveled by the sun from equinox to equinox. (The entire SPS is rolled 180° about the axis to the sun on each equinox.) As a result, less sunlight falls on the radiator, the radiator casts a smaller shadow on the concentrator, and the radiator sees a smaller effective meteoroid flux.

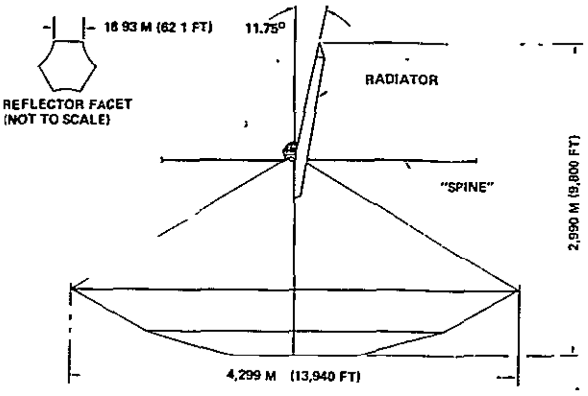

Fig. 5-12. Brayton Module

The module size shown is approximate to the use of four modules per 10 GW ground output SPS. The appropriate number of modules to use was determined by mass optimization. If the number of reflector facets is held constant (to keep a fixed concentrator efficiency) then the concentrator becomes proportionately heavier as a module is made smaller, since each facet still requires a pointing system and a support frame. As a module is made larger, the radiator system becomes proportionately heavier since addition of radiator area requires more manifold (and NaK) mass for a large module than for a smaller one (since the manifold lines must be longer to reach the added area in a larger module). These two effects act in opposite directions, allowing an optimization to be affected, as shown in Figure 5-13. Since the quantity of four, used in previous studies, is very close to the optimum of six, four modules were baselined.

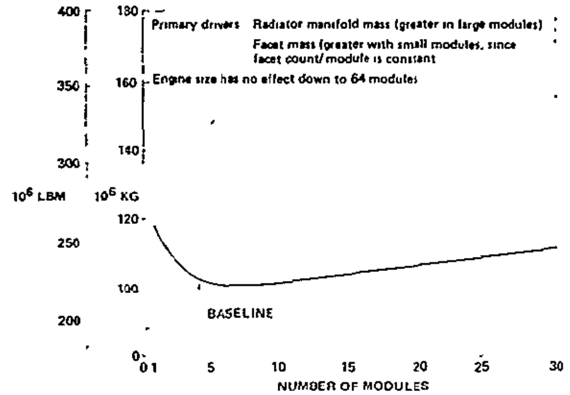

Fig. 5-13. Module Quantity Optimization

Operating temperatures for the Brayton System were set by use of an ISAIAH model. This model contained 93 independent and 32 dependent variables, all of which were simultaneously interacted to obtain an optimum. Significant resulting parameters are given in Table 5-4.

Table 5-4. Brayton SPS Parameters

- Cycle temperatures:
  - T0 400.7 K (261.3°F)(minimum gas temp, compressor in)
  - T1 586.9 K (596.4°F)(compressor out)
  - T2 1176 K (1657°F)(cavity inlet)
  - T3 1652K (2514°F)(cavity out, turbine in)
  - T4 1240 K (1772°F)(turbine out, recuperator in)
  - T5 651.4 K (712.5°F)(recuperator out, cooler in)
  - TL1 373.5 K (212.3°F)(radiator outlet)
  - TL2 597.0 K (614.6°F)(radiator inlet)
- Pressures:
  - P1 4.084 MN/m^2 (592 psi)(compressor outlet, maximum pressure)
  - P0 1.739 MN/m^2 (252 psi)(compressor inlet, minimum pressure)

$$P1/P0 = 2\ 348 = \text{cycle pressure ratio}$$

- Fraction pressure drops:

● In recuperator	0.02991
● In cooler	0.00957
● In cavity heat exchanger	0.02483
	0.06431

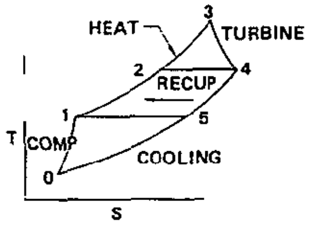

The resultant SPS system is illustrated in Figure 5-14. The four modules are arranged along the north-south axis which, in operation, lies parallel to the north-south axis of the earth. Thus the satellite flies "perpendicular to the orbit plane." Note that the four radiators are each inclined by 11.75°. Power distribution from the four cavity absorber assemblies to the transmitter takes place down the central "spine." The total solar capture area of the system is approximately 62 km^2 (24 square miles).

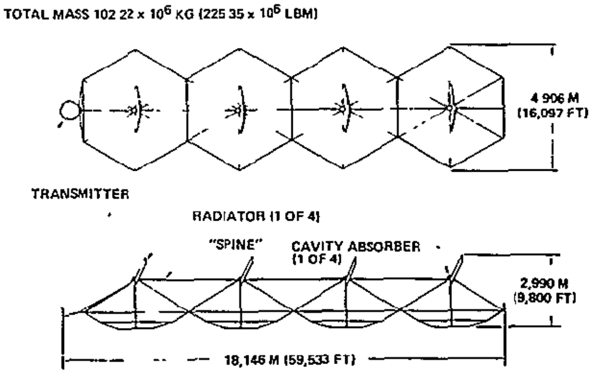

Fig. 5-14. Brayton SPS Configuration

Table 5-5 is a mass statement for the Brayton SPS.

Table 5-5. Brayton SPS Mass Statement

Solar concentrators	10^6 kg	10^6 lbm
Facets	4.38	9.66
Structure	10.64	23.46
	15.02	33.12
Conductive spine	1.20	2.64
Cavity absorber		
Tubing	3.92	8.64
Insulation/skin/frame	1.29	2.84
Turbomachines	2.16	4.76
Recuperator/coolers	6.36	14.02
Generators, with cooling	4.50	9.92
Step-up transformers, with cooling	2.11	4.65
Rotary transformer, with cooling	2.68	5.91
Rectifier/filters, with cooling	6.22	13.72
Radiators with pumps (BOL*)	43.28	95.42
Transmitter	11.90	26.23
Attitude control, station-keeping continued	1.58	3.48
Total	102.22	225.35

*Beginning of life; 4.2 x 10^6 kg NaK added over 30 years.

5.5 THERMIONIC BRAYTON CASCADE (CONCEPT 4)

The original incentive for study of this system was as follows:

1. A "topping" cycle using thermionics would allow the maximum temperatures in the SPS to occur only in the passive (non-moving) elements of the thermionic diodes.

2. After temperature reduction in the diodes, a Brayton cycle would follow, with the rotating parts consequently operating at a lower temperature.

3. The two systems combine to produce the required power.

Study of the two systems, however, indicate the following factors:

1. The efficiency of the thermionic system was 24% with a maximum temperature of 1800 K (2780°F) and a collector temperature of 1000 K (1340°F).

2. The Brayton system affords an efficiency of 24.4% with a maximum temperature (turbine inlet) of 1652 K (2514°F) and a minimum gas temperature of 401 K (262°F).

3. The thermionic system has a specific mass of about 8.2 kg/kW_e generated; the Brayton specific mass is about 5.0 kg/kW_e generated.

As a consequence all cascaded combinations of the two systems were seen to have a higher specific mass than the Brayton system alone.

5.6 SOLAR SILICON PHOTOVOLTAIC (CONCEPT 5)

Cell performance, radiation resistance, etc. are discussed in Section 4.7. A critical question is that of solar concentration ratio; if reflectors are used to augment cell performance, what should their area be relative to the cells?

As solar concentration is increased, the cell area relative to that of the total SPS decreases, concentration raises the temperature of the cells so that they become less efficient, tending to increase the required area of the SPS (including reflectors). Relatively small cell areas means that thicker cover glass can be used for radiation, protection without a high mass penalty. Also relatively small cell areas (by high concentration ratios) tends towards lower total cell cost, but may be offset by increased concentrator and structure cost and mass. Because of the complexity of these interactions, an ISAIAH computer model was developed. The block diagram of this model is given in Figure 5-16.

This chart shows the relationships between parametric elements which make up the model for photovoltaic system optimization. The following code is used:

I1	independent variable
I	dependent variable
t1	one-dimensional table
T1	two-dimensional table
+/-	summation function
ρ	ratio
π	product

REPRODUCIBILITY OF THE ORIGINAL PAGE IS POOR

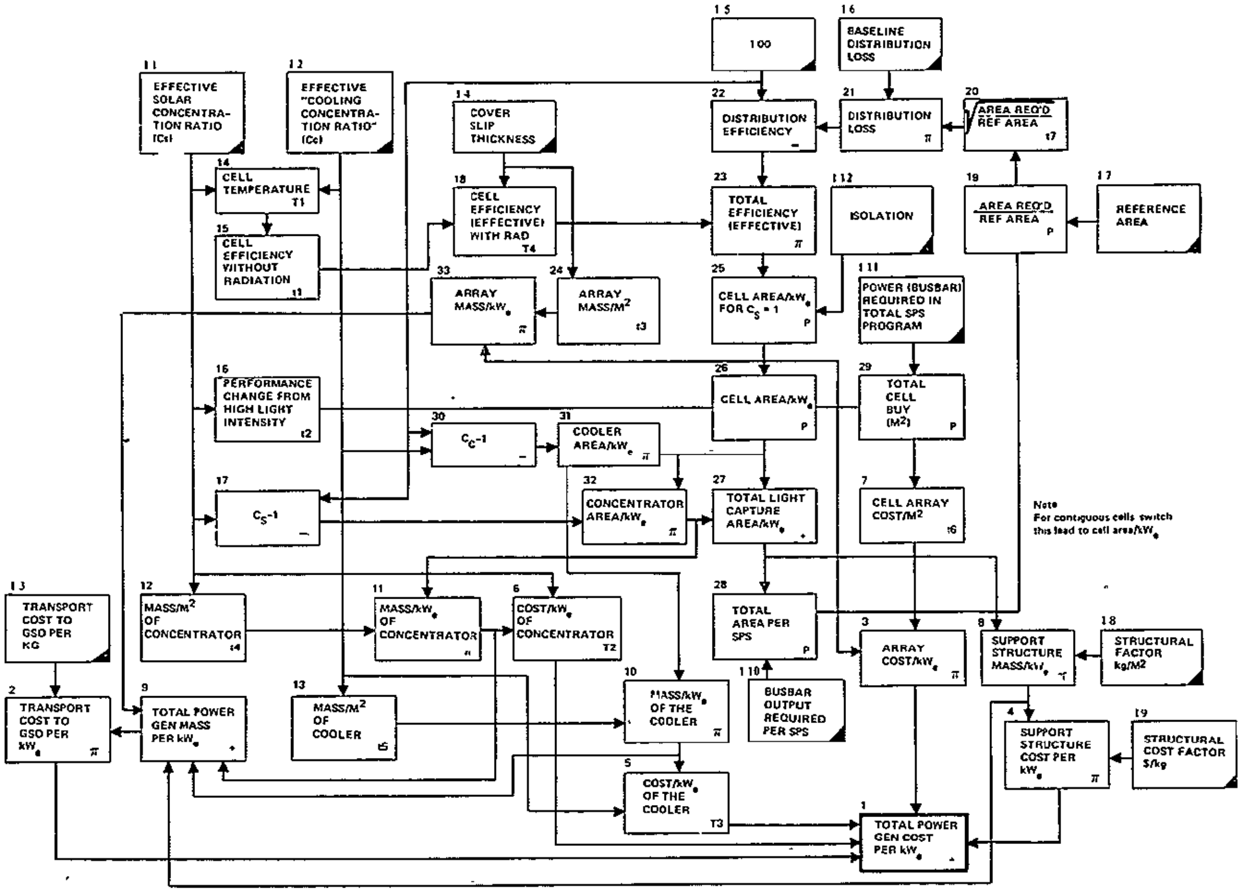

Note
For contiguous cells switch this lead to cell area/kWe

Fig. 5-15. Optimization Model, Photovoltaic SPS

The "objective function" is dependent variable one (1) "Total Power Generation Cost Per kWe." The machine program to process this model is ISAIAH (Integrated Sensitivity and Interactions Analysis—Heuristic).

As an example of the form of the data used in this model, refer back to Figure 4-31. This is the cost of solar arrays (per unit area) relative to the total area of cells procured. A production rate factor (or learning curve) of 80% was used; when the quality (area) produced is double that of the previous quantity, the unit cost per area of that quantity is 80% of that unit cost per area of the previous quantity. The curve of Figure 4-31 was used to produce Table #7 "CELL ARRAY COST/M^2" in Figure 5-15. As a further example, Figure 4-30 was the basis for Table #18 "CELL EFFICIENCY, EFFECTIVE, WITH RADIATION." Figure 5-16 shows the optimization results.

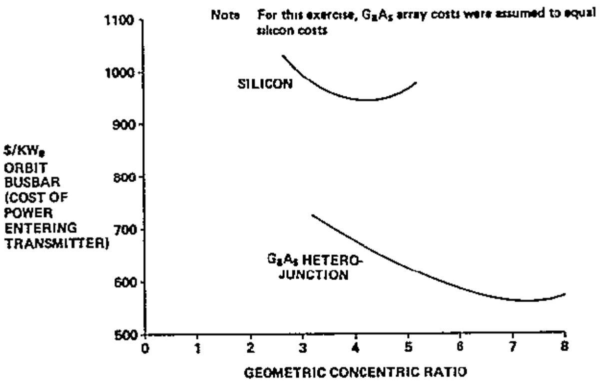

Note For this exercise, GaAs array costs were assumed to equal silicon costs

Fig. 5-16. Derivation at Optimum Concentration Ratios

Minimum orbit busbar costs are obtained with silicon solar cells with a concentration ratio of approximately 4.3. This means that the projected area of the SPS would be 4.3 times the area of the cells. The resultant SPS is not a minimum mass system. As shown in Figure 5-17, minimum cost does not coincide with minimum mass.

The assumed transportation cost to geosynchronous orbit in this optimization was $80 kg ($36.3/lbm).

In general, if solar cell costs for an SPS program are lower than shown in Figure 4-31 the optimum concentration ratio will be below 4.3, and conversely.

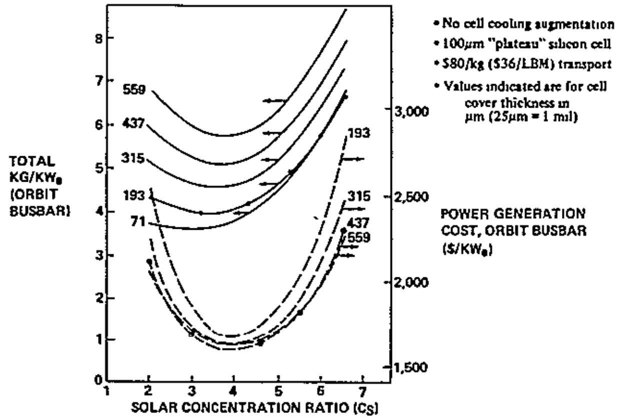

Fig. 5-17. Cost and Mass Minima are not Coincident

The microwave power transmission system efficiency was taken as 0.62; thus for a 10.0 GW ground output 16.17 GW must be supplied to the transmitter. Figure 5-18 shows the total orbit busbar power is determined.

Item	Efficiency	Power level, GW
Power to transmitter	—	16.17
DC distribution losses	—	17.43
Auxiliary ops, attitude control		17.58
Allowance for flying "P O.P"* (2 7%)		18.05
Self power transportation losses** (This is beginning of life output of 12 modules)		19 86

* Perpendicular to orbit plane

** 20% of cells exposed, 55% degradation

Fig. 5-18. Silicon SPS Efficiency Chain

With a concentration ratio of 4.3, the operating temperature of the cells is 367 K (201°F). Due to this elevated temperature, the cell efficiency (beginning of life) is only 11.23%. (A lower concentration ratio would yield higher efficiency, but as previously explained, higher cost.) At end of life (30 years) the cell efficiency is 7.5%, or 68% of the original.

Figure 5-19 shows the approaches considered to compensate for cell radiation degradation. Annealing of the damage (by thermal effects) is an apparently very desirable solution. However, pending tests which accurately and repeatedly duplicate the geosynchronous environment, including solar flares, annealing must be considered as uncertain. As shown, the concept of periodic cell/concentration addition was selected as the most promising of solutions other than annealing.

Consequently a modular configuration was developed. In this concept the SPS would begin life with the number of modules required to produce somewhat more than the required 10 GW ground output. After a period of time, cell degradation would have brought the output to 10 GW and additional area would have to be added. This process would be repeated over the 30 year life of the SPS.

1. For Brayton and thermionic, replace failed or degraded parts as needed:
   - Output remains essentially constant
2. For photovoltaic satellites, three approaches to handling cell degradation
   - A. Annealing —— Uncertain
   - B. Add new satellites —— Requires purchase of "extra" microwave power transmission systems
   - SELECTED → C Add new cell area —— Requires initial satellite design be capable of handling additions
   - D Initial oversize —— Wastes MPTS capability, front end cost

In addition, photovoltaic satellites require failed part replacement

Fig. 5-19. Approaches to SPS Maintenance

Figure 5-20 shows the selected silicon SPS configuration. The system begins life with 12 modules installed. At the end of life 18 modules are installed; during the 30 year life the system output does not drop below 10 GW (ground). Figure 5-21 shows the main frame of the SPS to which the 18

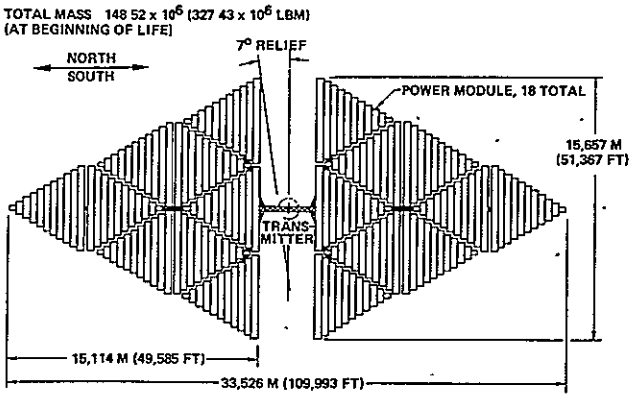

Fig. 5-20. Silicon SPS End-of-Life Configuration

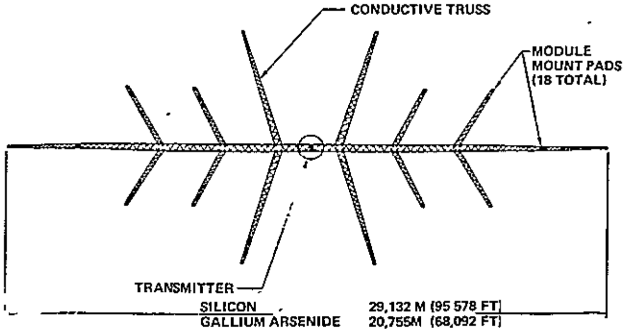

Fig. 5-21. Main Frame, Silicon SPS

modules are attached. The modular system permits utilization of the self power concept, wherein the modules are fabricated in low orbit and are flown to geosynchronous orbit by electric thrusters energized by the output of the module itself. In this orbit transfer mode, only 20% of the cells are in place (the remaining 80% are in radiation shielded canisters). The exposed cells lose 55% of their output capability as a result of exposure to the trapped radiation environment.

Figure 5-22 gives the dimensions of a single power module. The basic power element is a one megawatt strip 380 M (1247 ft.) long and 20 M (65.6 ft.) wide. This module is supported on its own frame, including an interface (or "docking") pad by which it connects to the main frame of the satellite.

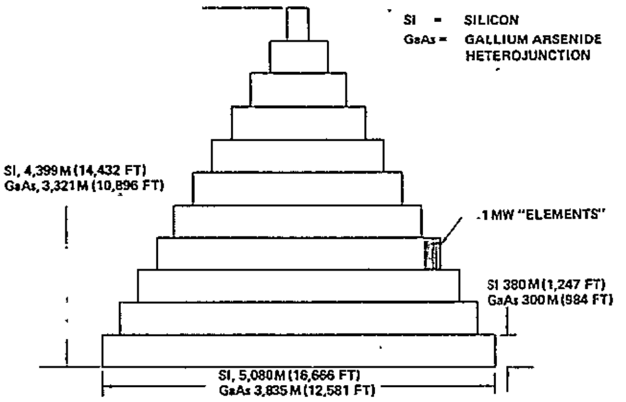

Fig. 5-22. Silicon SPS Power Module

The solar arrays of the power module are as shown in Figure 5-23. The total silicon array thickness is 410 micrometers (0.01614 inches). In this figure, thickness (relative to width) has been multiplied by a factor of 100 for visibility. A cell thickness of 100 micrometers (0.004 inch) was baselined as the minimum that could with assurance be considered practical.

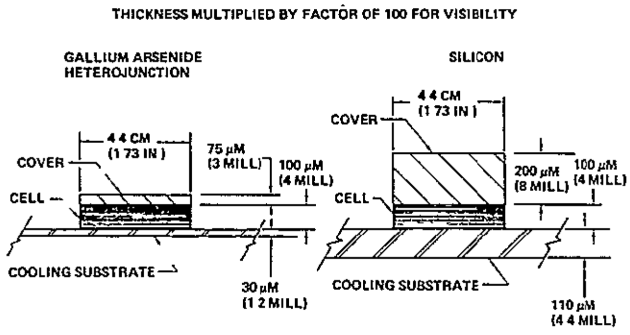

Figure 5-23. Photovoltaic Array

Ideally, the compound parabolic concentrators need be only thick enough to support themselves against installation loads (perhaps 2 micrometers, i.e., 0.0008 inch thick). A possible means of fabrication might be vapor deposition upon a smooth mandril, turning out many CPC's at once. However, the capability to do this is not assured. Therefore a conventional fabrication method, impact extrusion, was baselined. The thickness was set at 75 micrometers (0.003 inch). Consequently the concentrators are the largest item in the mass table (Table 5-5).

Table 5-5. Silicon Photovoltaic SPS Mass Statement

	Initial satellite (with 12 modules)		Six make-up modules	
	10^6 KG	10^6 LBM	10^6 KG	10^6 LBM
Cooler	41 45	91 38	20 72	45 68
Concentrators	43 86	96 69	21 93	48 35
Cells and covers	27 44	60 49	13 72	30 25
Concentrator frames	2 19	4 83	1 10	2 43
Array mount system	2 74	6 04	1 37	3 02
Cell radiation cans	0 86	1 90	0 43	0 95
Electrical control	2 97	6.55	1 49	3.28
At. cont/station keep	1 40	3 09	0 70	1 54
Structure	13 71	30.22	3 79	8 35
Transmitter	11 90	26 23	–	–
	148.52	327 43	65.25	143 85
Areas	KM^2	$Mile^2$	KM^2	$Mile^2$
Cell	31 1	12 00	15 6	6 02
Projected concentrator	102.9	39 71	51 5	19 87
Total	134 1	51 71	67 1	25 89

5.7 SOLAR GALLIUM ARSENIDE PHOTOVOLTAIC (CONCEPT 6)

As with the silicon system, an optimization was performed to determine the best concentration ratio. For this optimization the cost of GaAs arrays was considered to be the same for identical construction volumes as silicon arrays. Due to the better temperature coefficient of GaAs as compared to silicon, the resultant concentration ratio was 7.5 (see Figure 5-16). As with silicon, the minimum cell thickness was taken as 100 micrometers (0.004 inch).

Due to the higher concentration ratio, the compound parabolic concentrators are larger for a given cell size than with silicon. This is illustrated in Figure 5-24.

The lower radiation damage rate of gallium arsenide cells (only approximately one third that of silicon) means not as much array must be added to the SPS over its life to maintain the required 10 GW output.

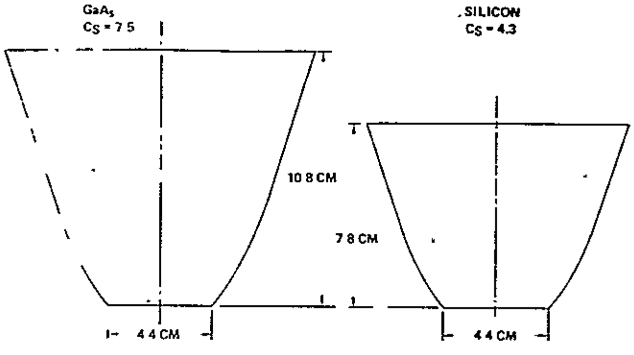

GOAL IN SPACE PRODUCTION BY VAPOR DEPOSITION, T ≈ 12μM (1/2 MILL)
BASELINE SURFACE FABRICATION BY CONVENTIONAL MEANS, T = 75μM (3 MILL)

Fig. 5-24. Compound Parabolic Concentrators

Figure 5-25 shows the GaAs SPS configuration; it begins geosynchronous operation with 16 modules present. Two additional modules are added (after 12 years) to bring the system to its total of 18. The ground output is 10 GW or more throughout the 30 year life. The GaAs SPS end of life area is 113.2 km^2 (43.69 miles^2) compared to 201.2 km^2) for the silicon SPS.

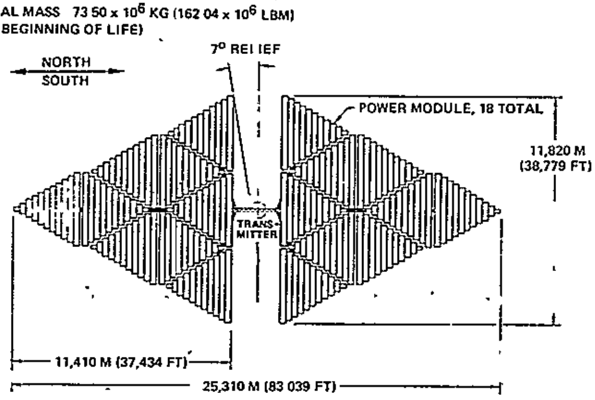

Fig. 5-25. GaAs SPS Configuration

As with the silicon SPS, minimum concentrator thickness was assumed to be 75 micrometers (0.003 inch); the concentrators are the most massive element of the GaAs SPS, but permit the required power to be produced by the SPS program while procuring only approximately one-fifth of the cells that would otherwise be required. With the 80% production rate factor (learning curve) assumed for cell costs, this reduction in cell area is extremely significant.

Table 5-6 gives the total GaAs mass statement, including the beginning of life (BOL) condition masses and the mass of the two add-on modules.

Table 5-6. GaAs SPS Mass Statement

	Initial satellite (with 16 modules)		Two make-up modules	
	10^6 KG	10^6 LBM	10^6 KG	10^6 LBM
Cooler	7.98	17.64	1.00	2.20
Concentrators	29.94	64.82	3.74	8.25
Cells and covers	8.22	18.12	1.03	2.27
Concentrator frames	1.50	3.31	0.19	0.42
Array mount system	0.82	1.81	0.10	0.22
Cell radiation cans	0.26	0.57	0.13	0.29
Electrical control	2.83	6.24	0.35	0.77
At. cont/station keep	0.80	1.76	0.10	0.22
Structure	9.25	20.39	0.72	1.59
Transmitter	11.90	26.23	–	–
	73.50	162.04	7.26	16.00
Areas	KM^2	Mile^2	KM^2	Mile^2
Cell	13.6	5.25	1.51	0.58
Projected concentrator	88.3	34.07	9.81	3.79
Total SPS	101.9	39.32	11.32	4.37

5.8 NUCLEAR THERMIONIC (CONCEPT 7)

Nuclear reactors are discussed in Section 4- . The nuclear thermionic SPS configuration investigated was the molten salt breeder reactor (MSBR). Thermionics are discussed in Section 4-6.

Probable maximum effective power densities for thermionic diodes of 10 w/cm^2 cause a 17.5 GW orbit busbar SPS (10 GW ground output) to require 175,000 m^2 (1.88x10^6 ft^2) of active diode area. The baselined reactor quantity for a 10 GW SPS was 16; their total thermal power would be approximately 40 GW. The surface area of all of these reactors (diameter of 4 meters each) is only 804 m^2 (8654 ft^2). Thus the reactor walls do not provide sufficient area for mounting of the diodes. Therefore a sensible heat sodium loop is provided to heat the diode emitters, which located separately from the reactors. The molten salt flow from the reactors of course contains sufficient thermal energy but has insufficient volume to heat the required 175,000 m^2. Thus a molten salt to sodium heat exchanger is required, as shown in Figure 5-26.

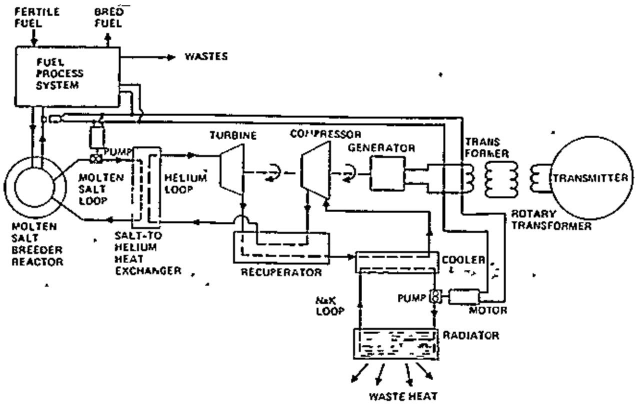

Fig. 5-26. MSBR Nuclear Thermionic System

The sodium flow must transfer heat to each diode emitter; the NaK flow of the radiator loop removes heat from the diode collectors. Figure 5-9 shows a possible method of interfacing a heat transfer loop to a thermionic diode. Good thermal contact is required, yet electrical isolation must be provided.

Pumping power for the radiator is parasitic upon the diode output. Therein lies the fundamental problem with the nuclear thermionic concept.

1. Maximum temperature is set by the reactor capability.
2. Minimum temperature is set by the size of the radiator system.
3. Larger and cooler radiators require the most pumping power.
4. A high temperature radiator reduces diode efficiency, thus increasing the waste heat to be dissipated.

If the diode efficiency is E, and the electrical power required for the MTPS is P_{MTPS} then the waste power (power to be rejected) is:

$$R = P_{MTPS} \left(\frac{1}{E} - 1\right)$$

For a radiator pumping power of P_{pump}, the heat rejection increases:

$$R = (P_{MTPS} + P_{pump})\left(\frac{1}{E} - 1\right)$$

But P_{pump} is a function of R, i.e., more heat rejection requires a larger radiator and more pumping power.

Evaluation of this concept over a wide range of collector temperatures indicated that the system could not generate the pumping power necessary to pump the radiator system required for waste heat generation. As an example, with a 1020 K (1394°F) emitter and a 400 K (260°F) emitter, the diode efficiency is only 23%. Thus 77% of the solar power absorbed must be rejected as a waste heat. The resultant radiator pumping power exceeds the diode output

5.9 NUCLEAR CLOSED BRAYTON CYCLE (CONCEPT 8)

The nuclear Brayton cycle SPS contains sixteen 1 GW busbar output molten salt breeder reactor modules. The main structure of the satellite consists of a spine with sixteen ribs to which are attached the reactor modules and their primary radiators. Each reactor module has secondary radiators for cooling the generators and nuclear fuel processing systems. The ground output of the nuclear Brayton cycle power satellite is 10 GW. The concept is shown in Figure 5-27.

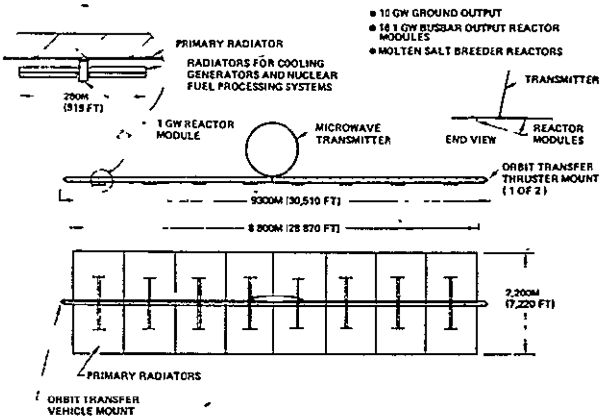

Fig. 5-27. Nuclear Brayton Cycle SPS

In the baseline concept, Figure 5-28, sixteen of these modules are used to provide 10 GWe ground output. The molten salt breeder reactor (MSBR) is spherical. The shield to reduce the radiation level at the transmitter is located only along lines-of-sight to the transmitter. Molten salt flows to six

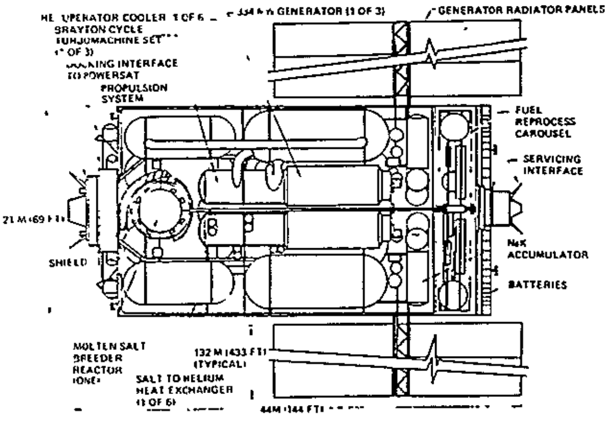

Fig. 5-28. Reactor Module

salt-to-helium heat exchangers. Hot helium then flows to turbines of the Brayton rotating unit (three, with one generator each). Six recuperator modules surround the turbomachines. The helium-to-liquid metal (NaK) heat exchangers (coolers) are located in the recuperator housings. NaK accumulators (volume make-up) and pumps are located between the recuperators and the fuel process carousel. High and low temperature NaK and electrical power pass through the interface to the powersat main frame (on left).

A small flow of molten salt is continuously circulated through the fuel process module, which accomplishes the following:

- Removes protactinium (which decays to uranium).
- Removes other wastes
- Removes bred fuel
- Accepts fertile fuel
- Adjusts salt mixture

The fuel process module is located on a continuously rotating carousel; the resultant inertial forces simulate gravity and permit operation of the countercurrent separation columns. Module servicing (e.g., waste removal) is accomplished through the docking port on the right.

The battery stack on the right is part of the system which allows the reactor module to separate and operate as an independent spacecraft. Propulsion and attitude control systems are located at the left, delta velocity capability is nominally 100 m (328 ft/sec) which allows a malfunctioning reactor system to be undocked and separated a safe distance from the powersat which continues to operate at a reduced power level.

In Section 4.9 reasons were given for consideration of a rotating particle bed reactor (RPBR). Two approaches to implementing the RPBR are given in Figure 5-29:

1. Rotate the reactor itself about its vertical axis. This is the type reactor system examined by the Brookhaven National Laboratory. This concept is shown on the left; note that a rotating seal is required in the gas loop. In this configuration 64 individually rotating reactors would be used in a 20 GW ground output unit. This concept does not require a rotary joint of the transmitter.

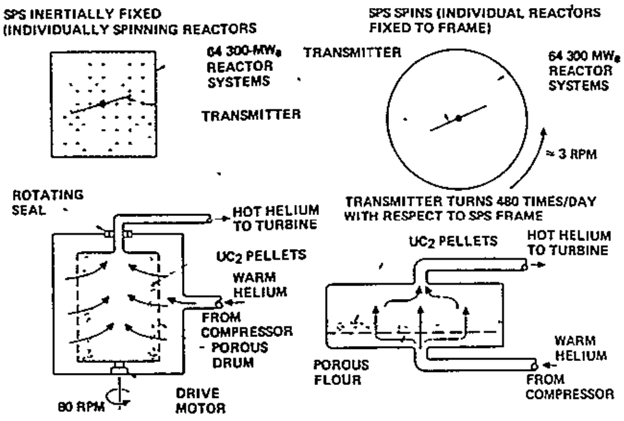

Fig. 5-29. RPBR Approaches

2. Locate the reactor in a rotating assembly to produce a conventional "gravity" field in the reactor. This way the same type reactor can be used in space and on earth. The reprocessing plant, and other reactor systems, could be located in the same rotating assembly. For this configuration a 1 g level at the reactors is produced by rotation at 3 rpm. This means that the rotary joint to the transmitter rotates at this rate—a possible problem.

A potential rotating particle bed reactor configuration is shown in Figure 5-30.

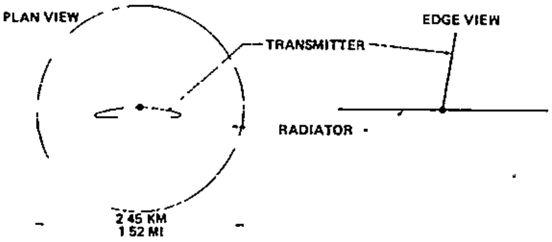

Fig. 5-30. Simplified RPBR Configuration

The circular element is the radiator system, a planar array made up of panels, headers and manifolds as in the solar Brayton configuration. The projected area is 4.71 km^2 (1.82 mile^2). The transmitter and power generating systems are located at the center of the radiator.

A mass statement (preliminary estimate) for the RPBR system is given in Table 5-7.

Table 5-7. Rotating Particle Bed Reactor SPS Mass Statement

Item	10^6kg	10^6lbm
Turbomachines	2.16	4.76
Recuperation/coolers	6.36	14.02
Generators, with cooling	4.50	9.92
Step-up transformers, with cooling	2.11	4.65
Rotary transformers, with cooling	2.68	5.91
Rectifier/filters, with cooling	6.22	13.72
Radiators with pumps (initial)	43.28	95.42
Transmitter	11.90	26.23
Reactor systems, shields	16.00	35.27
Fuel reprocess system	2.00	4.41
Framework	1.00	2.20
Attitude control, stationkeeping	0.60	1.32
	98.81	217.83

5.10 SOLAR POWER TRANSFER (CONCEPT 9)

A mirror system in geosynchronous orbit which would directly reflect sunlight to an area on the surface of the earth might be used to enhance the performance of a ground based solar power generating system. Analysis was first concentrated on the size of image which a geosynchronous mirror could produce:

An important optical effect must be considered. Since the sun is not a point source, its angular width of 0.53°, as viewed from the region of the Earth, will be duplicated by the reflected light cone produced by any mirror, no matter its size (see Figure 5-31).

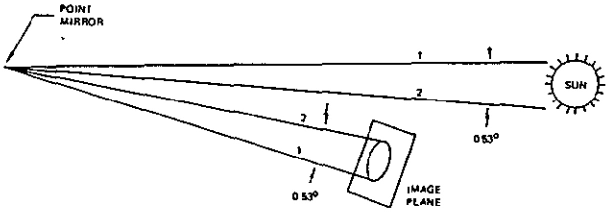

Fig. 5-31. Cone Angle of Solar Image is Equal to the Cone Angle to the Sun

This was noted in 1929 by Herman Oberth on page 354 of his "Wege Zur Raumschiffahrt" (Ways to Space Flight), "The laws of optics provide that the reflected image of the sun, seen from a facet of the mirror, must appear at least as large as the sun itself, seen from the mirror."

As a consequence, the smallest image which can be produced on Earth by any geosynchronous orbit mirror is approximately 330 km (205 s.m.) in diameter.

Figure 5-32 shows that an orbital mirror can not provide full illumination at all times; for example, at noon the mirror is edge-on to the sun and no image can be produced.

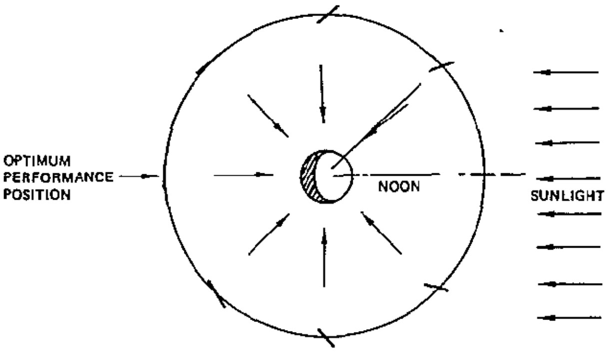

Fig. 5-32. Mirror Attitude Changes Around Orbit

Figure 5-33 shows the approximate combined output of the sun and the satellite mirror assuming a mirror sized to produce at midnight an output equal to the sun at noon. The average of the combined output over the 24 hour period is almost exactly one "sun."

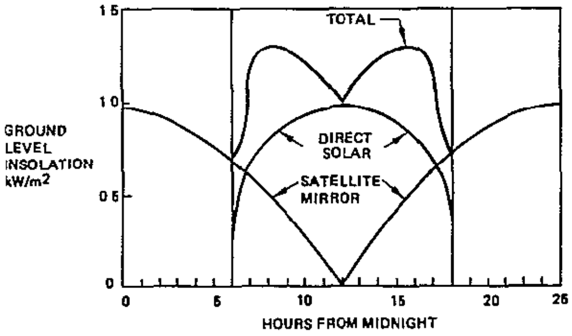

Fig. 5-33. Combined Mirror and Solar Output

The target size to be shown is based on the following somewhat optimistic assumptions:

1. Optimum mirror curvature, i.e., all elements of mirror surface "aimed" at target center.

2. No scattering of reflected light by mirror surface irregularities.

3. Perfect mirror pointing.

Assignment of probable values to these three factors indicates that actual target areas would be approximately 20% larger than the ideal image size indicated.

Potential target area were sought with a goal of minimum population in the image area. Two "best" sites were identified; one is in the southwest desert near the Mexican border; the other is near the Canadian border. Approximately 70,000 and 50,000 persons live in, respectively, the low and high latitude sites.

Figure 5-34 shows the low latitude target area for the power relay system.

Image sizes were calculated for three United States latitudes (λ). The images are elliptical, with the long axis running parallel to lines of longitude.

Image sizes are given in Table 5-8; dimensions a and b are, respectively, the semi-major and semi-minor axes:

Unless moved out of the target area, the occupants would be exposed to the full environments effects produced by having a one sun average illumination continuously (unless blocked by clouds). The average surface temperature would tend to rise to approximately 150°F.

The mirror itself must have a curved surface in order to maintain the required image. If composed of individual facets on a flat base, each facet must be oriented so that all images are superimposed. The edge facets are tilted the most, by 0.13 relative to the mirror plane. Some form of active tilt control would probably be required. To provide a reflected solar image of one sun intensity, a mirror having at least the same area as the ground target is required; it would have a system mass of 4×10^{10} KG (45,000,000 tons). Over 10^6 kW of on board power generation capacity would be required to drive the electric thrusters necessary to overcome the "solar sail" thrust forces.

Optical effects cause minimum image size to be quite large:

Any target area selected within contiguous U.S. will involve at least 50,000 occupants.

For "one sun" image strength:

1) Total mirror area required is ≈ 134,000 km^2 (52,000 mi^2)
2) System mass is ≈ 4×10^{10} kg (45,000,000 tons)

The mirror system may cause significant environmental effects

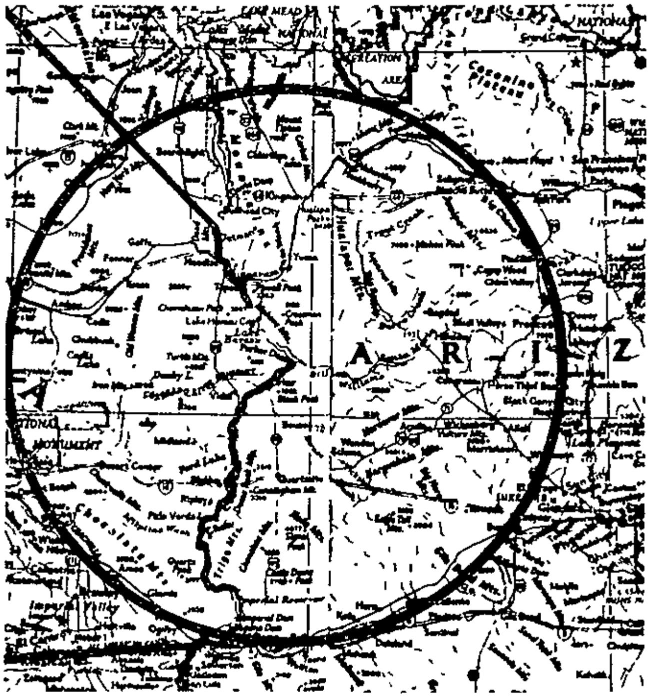

Fig. 5-34. Shows the Low Latitude Target Area for the Power Relay System

Table 5-8. Tangent Plane Image Size for Various Latitudes

$\lambda = 30^{\circ}$	$\lambda = 40^{\circ}$	$\lambda = 50^{\circ}$
a = 208.0 km (129 s.m.) b = 170 4 km (106 s.m)	a = 250.89 km (156 s.m.) b = 173 4 km (108 s.m.)	a = 327.83 km (204 s.m.) b = 177.05 km (110 s.m.)

6.0 COST

6.1 BASELINED AUXILIARY SYSTEMS

Low orbit construction and self powered transfer to geosynchronous orbit was baselined, due to the apparent lower cost of this approach. The launch vehicle baselined was the Class IV, single stage to orbit, from the Heavy Lift Launch Vehicle study. The electric propulsion concepts and the chemical OTV maintenance freighter concepts were drawn from the Future Space Transportation System Analysis Study. Figure 6-1 is the low orbit launch vehicle; Figure 6-2 is the chemical OTV maintenance freighter.

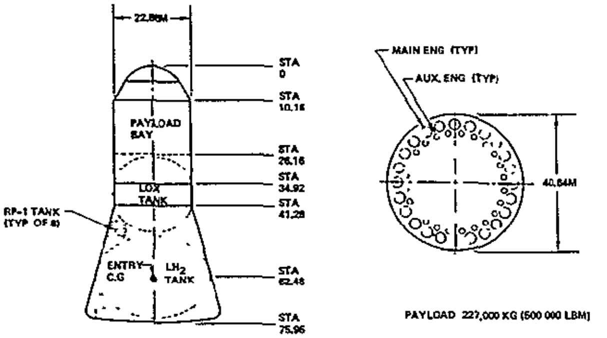

Fig. 6-1. Heavy Lift Launch Vehicle

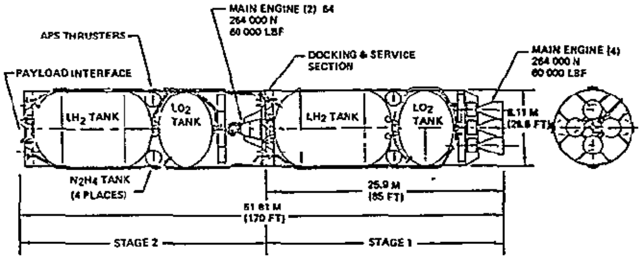

- Payload capability = 227 000 kg (500 000 lbm)
- OTV startburn mass = 549 000 kg (1 100 000 lbm)
- Stage characteristics (each)
  - Propellant = 222,270 kg (490,000 lbm)
  - Inerts = 20 400 kg (45 000 lbm)

Fig. 6-2. Chemical OTV Maintenance Freighter

In the self power concept electric power produced by a SPS module built in low orbit energizes thrusters which raise it to high orbit. The propulsion system consists of magnetoplasmadynamic (MPD) thrusters, argon propellant tanks, electric power processors, controls, gimbals, frames, etc. Figure 6-3 gives quantities and masses associated with each emphasized SPS concept

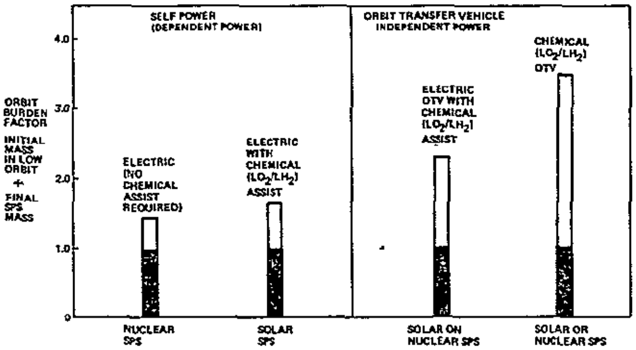

Fig. 6-3. Self Power Requirements

Figures 6-4 through 6-10 show assembly and support stations baselined for the various SPS concepts.

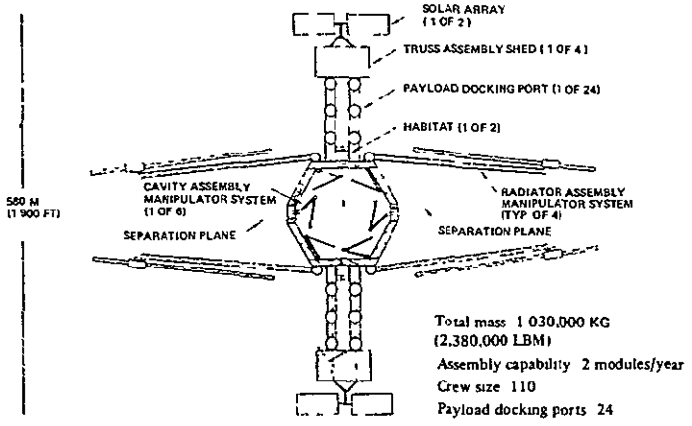

Total mass 1 030,000 KG (2,380,000 LBM)
Assembly capability 2 modules/year
Crew size 110
Payload docking ports 24

SOLAR BRAYTON ASSEMBLY STATION

Fig. 6-4. Thermal Engine SPS Assembly Station

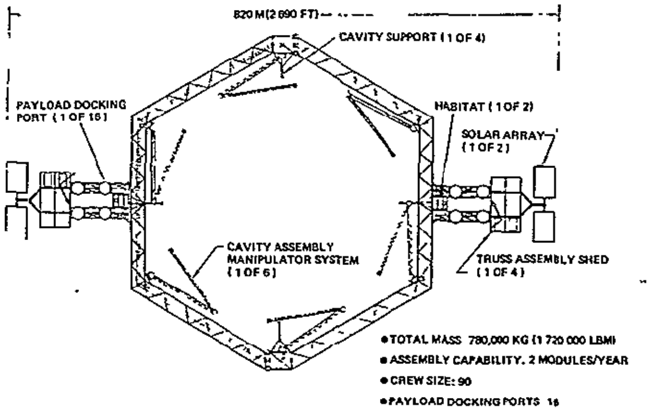

- TOTAL MASS 780,000 KG (1 720 000 LBM)
- ASSEMBLY CAPABILITY. 2 MODULES/YEAR
- CREW SIZE: 90
- PAYLOAD DOCKING PORTS 16

THERMIONIC ASSEMBLY STATION

Fig. 6-5. Thermionic SPS Assembly Station

Assembly capability eight 1 GW modules/year
Total mass 2,750,000 KG (6,063,000 LBM)
Crew size 240
Payload docking ports 62

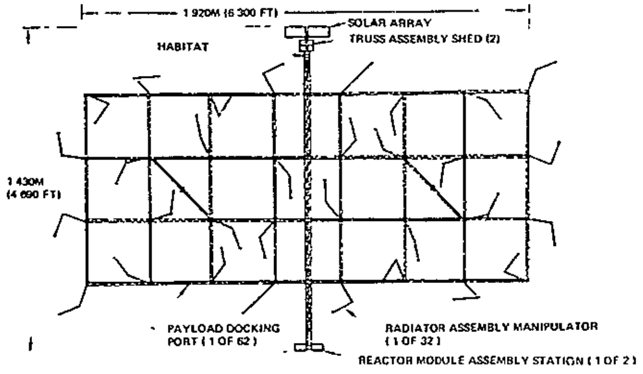

Fig. 6-6. MSBR (Nuclear) SPS Assembly Station

MASS 120 000 KG GaAs (150 000 Si)
CREW 25 GaAs 32 SILICON
DOCKING 3 HLLV PAYLOAD PORTS (4 SILICON)
9 STANDARD PORTS

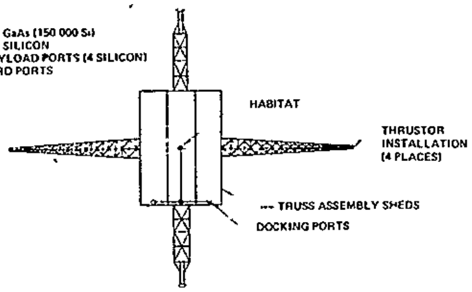

Fig. 6-7. Photovoltaic SPS Main Frame Assembly Station

- Total mass (without spares or support vehicles) : 600,000 KG
- Support capability: up to Powersats producing a total of 100 GW ground output
- Payload docking ports 21
- Maximum crew size 50
- Placement by arriving Powersat module

MASS 70 000 KG GaAs (90 000 SILICON*)
CREW 20 GaAs 25 SILICON
DOCKING 4 HLLV PAYLOAD PORTS (6 SILICON)
8 STANDARD PORTS

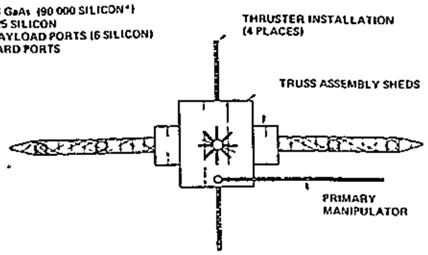

Fig. 6-8.. Photovoltaic SPS Module Assembly Station

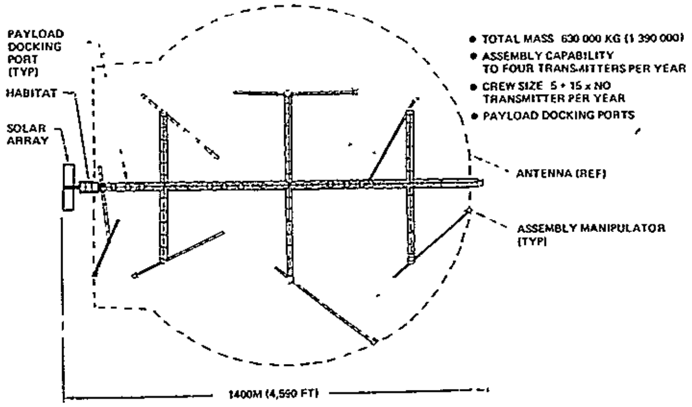

- TOTAL MASS 630 000 KG (1 390 000)
- ASSEMBLY CAPABILITY TO FOUR TRANSMITTERS PER YEAR
- CREW SIZE 5 + 15 x NO TRANSMITTER PER YEAR
- PAYLOAD DOCKING PORTS

Fig. 6-9. SPS Transmitter Assembly Station

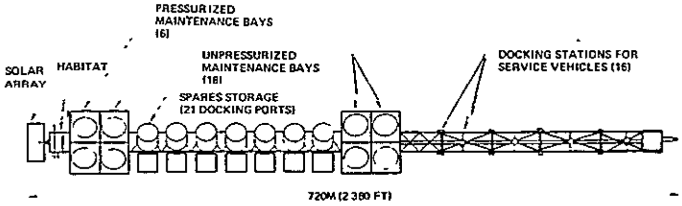

Fig. 6-10. SPS Geosynchronous Orbit Assembly Station

	1995	1996	1997	1998	1999	2000	2001	2002	2003	2004	2005	2006	2007	2008	2009	2010	2011	2012	2013	2014	2015	2016	2017	2018	2019	2020	2021	2022	2023	2024	2025	2026	2027	2028	2029	2030	2031	2032	2033	2034	2035	2036	2037	2038	2039	2040	2041	2042	2043	2044	2045
SPS ADDED EACH YEAR	0	0.25	0.25	0.50	1	1	2	2	2	2	2	3	3	4	4	4	4	5	5	5	5	5	0	0	0	0	0	0	0	0	0	0	0	0	0	0	0	0	0	0	0	0	0	0	0	0	0	0	0	0	0
TOTAL SPS AVAILABLE	0	0.25	0.50	1	2	3	5	7	9	11	13	16	19	23	27	31	35	40	45	50	55	60	60	60	60	60	60	60	60	60	60	59.75	59.5	59	58	57	56	53	51	49	47	44	41	37	33	29	25	20	15	10	5
RECTENNAS ADDED	0	1	0	0	1	1	2	2	2	2	2	3	3	4	4	4	4	5	5	5	5	5	0	0	0	0	0	0	0	0	0	0	0	0	0	0	0	0	0	0	0	0	0	0	0	0	0	0	0	0	0
TOTAL RECTENNAS	0	1	1	1	2	3	5	7	9	11	13	16	19	23	27	31	35	40	45	50	55	60	60	60	60	60	60	60	60	60	60	60	60	59	58	57	56	53	51	49	47	44	41	37	33	29	25	20	15	10	5
GROUND OUTPUT GW ADDED	0	2.5	2.5	5	10	10	20	20	20	20	20	30	30	40	40	40	40	50	50	50	50	50	0	0	0	0	0	0	0	0	0	0	0	0	0	0	0	0	0	0	0	0	0	0	0	0	0	0	0	0	0
GROUND OUTPUT GW AVAILABLE	0	2.5	5	10	20	30	50	71	90	110	130	160	190	230	270	310	361	401	451	501	550	601	601	598	598	600	599	600	601	602	600	600	599	589	580	569	547	526	506	486	467	438	410	368	327	287	246	196	146	97	48
NUMBER OF MAKE UP MODULES ADDED	0	0	0	0	1	1	1	3	3	3	4	5	5	6	8	9	10	11	12	14	14	16	16	11	13	14	10	11	11	11	7	7	8	8	9	4	4	4	5	5	5	5	5	0	0	0	0	0	0	0	0
LOW ORBIT STATIONS IN OPERATION (FRAME)	1	1	1	1	1	1	2	2	2	2	2	3	3	4	4	4	4	5	5	5	5	5	0	0	0	0	0	0	0	0	0	0	0	0	0	0	0	0	0	0	0	0	0	0	0	0	0	0	0	0	0
TRANSMITTER STATIONS IN OP	1	1	1	1	1	1	1	1	1	1	1	1	1	1	1	1	2	2	2	2	2	2	0	0	0	0	0	0	0	0	0	0	0	0	0	0	0	0	0	0	0	0	0	0	0	0	0	0	0	0	0
GSO STATIONS IN OP (MODULE STA)	0	1	1	1	3	3	5	5	5	5	5	6	5	7	10	10	10	12	13	13	13	13	3	3	3	3	2	2	2	2	2	2	2	2	2	1	1	1	1	1	1	1	1	1	1	1	1	1	1	1	1
PERSONNEL IN LOW ORBIT	77	102	107	202	227	227	424	424	424	424	424	621	621	818	843	843	843	1045	1045	1045	1045	1045	76	76	76	75	50	50	50	50	50	50	50	50	50	25	25	25	25	25	25	25	25	0	0	0	0	0	0	0	0
PERSONNEL IN HIGH ORBIT	0	20	20	20	31	34	40	46	52	58	64	73	82	96	143	165	170	185	200	240	255	255	255	255	255	255	255	230	230	230	230	230	230	227	224	146	190	184	178	172	166	157	148	111	99	87	75	60	45	30	15
HEAVY LIFT LAUNCHES PER YEAR	16	296	293	575	1242	1248	2398	2520	2597	2621	2722	3901	4074	5264	5453	5577	5701	6965	7099	7241	7321	7580	1930	1550	1702	1778	1474	1550	1550	1550	1510	1510	1322	1312	1377	983	959	930	989	965	940	905	517	441	396	347	298	238	179	119	79
MODULES TRANSFERRED TO HIGH ORBIT (BASIC)	0	3	3	6	12	12	24	24	24	24	24	36	36	48	48	48	48	60	60	60	60	0	0	0	0	0	0	0	0	0	0	0	0	0	0	0	0	0	0	0	0	0	0	0	0	0	0	0	0	0	0
GSO FREIGHTER TRIPS	3	3	3	3	7	11	17	24	31	38	45	55	65	79	92	106	119	136	153	170	187	204	204	204	204	204	204	204	204	204	204	204	204	201	198	194	187	181	174	167	160	150	140	126	113	99	85	68	51	34	17
SUPPORTING SHUTTLE LAUNCHES (GROWTH)	4	5	6	9	11	11	19	19	20	20	20	28	29	37	40	40	41	50	50	52	52	52	14	14	14	14	12	12	12	12	12	12	12	12	11	9	9	9	9	8	8	8	7	5	4	4	3	3	2	2	1
HEAVY LIFT VEHICLES PROCUREDW/O WEAROUT	1	2	0	2	4	0	8	2	0	0	1	7	0	8	1	1	1	9	3	0	0	2	0	0	0	0	0	0	0	0	0	0	0	0	0	0	0	0	0	0	0	0	0	0	0	0	0	0	0	0	0
GSO FREIGHTERS PROCURED W/O WEAROUT	1	0	0	0	0	0	0	0	0	0	0	0	0	0	0	0	0	0	0	1	0	0	0	0	0	0	0	0	0	0	0	0	0	0	0	0	0	0	0	0	0	0	0	0	0	0	0	0	0	0	0
MODULE TRANSFER SETS PROCURED	0	3	3	6	13	13	25	27	27	27	28	41	42	54	56	57	58	61	72	74	74	76	16	11	13	14	10	11	11	11	7	7	8	9	9	4	4	4	5	5	5	5	5	0	0	0	0	0	0	0	0
MODULE ASSEMBLY STATIONS (LEO)	1	1	1	2	4	4	7	7	7	7	7	11	11	14	14	15	15	17	18	19	19	19	4	3	4	4	3	3	3	3	3	2	2	2	3	1	1	1	1	5	5	5	5	0	0	0	0	0	0	0	0

(NOT INCLUDING WEAROUT)

Fig. 6-11. Silicon Photovoltaic SPS Program

Manning requirements to construct the SPS units at the required rates, numbers of stations, maintenance flights, space shuttle crew rotation flights, rectenna installations, etc., were calculated for the SPS system concepts as given in Figures 6-11 through 6-14.

Fig. 6-12. Gallium Arsenide Photovoltaic SPS Program

	1995	1996	1997	1998	1999	2000	2001	2002	2003	2004	2005	2006	2007	2008	2009	2010	2011
SPS ADDED EACH YEAR	0	0.25	0.25	0.50	1	1	2	2	2	2	2	3	3	4	4	4	4
TOTAL SPS AVAILABLE	0	0.25	0.5	1	2	3	6	7	9	11	13	16	19	23	27	31	35
RECTENNAS ADDED	0	1	0	0	1	1	2	2	2	2	2	3	3	4	4	4	4
TOTAL RECTENNAS	0	1	1	1	2	3	6	7	9	11	13	16	19	23	27	31	35
GROUND OUTPUT GW ADDED	0	2.5	2.5	5	10	10	20	20	20	20	20	30	30	40	40	40	40
GROUND OUTPUT GW AVAILABLE	0	2.5	5	10	20	29.8	29.6	69.3	79.5	99.0	118.8	138.5	168.1	197.7	237.5	277.1	316.8
NUMBER OF MAKE UP MODULES ADDED	0	0	0	0	0	0	1	2	1	2	2	2	3	4	4	5	6
LOW ORBIT STATIONS IN OPERATION (FRAME)	1	1	1	1	1	1	2	2	2	2	2	3	3	4	4	4	4
TRANSMITTER STATIONS IN OP	1	1	1	1	1	1	1	1	1	1	1	1	1	1	1	1	2
GSO STATIONS IN OP (MODULE STA)	0	1	1	1	2	2	6	6	6	5	5	7	7	8	8	9	9
PERSONNEL IN LOW ORBIT	50	65	65	85	105	105	225	225	225	225	225	325	325	425	425	450	465
PERSONNEL IN HIGH ORBIT	0	20	20	20	40	40	100	100	100	100	100	140	140	180	180	180	180
HEAVY LIFT LAUNCHES PER YEAR	13	136	135	258	533	535	1060	1085	1095	1113	1127	1673	1687	2238	2261	2293	2329
MODULES TRANSFERRED TO HIGH ORBIT (BASIC)	0	3	3	6	12	12	24	24	24	24	24	36	36	48	48	48	48
GSO FREIGHTER TRIPS	2	2	2	2	5	6	10	14	18	22	26	33	38	47	54	62	70
SUPPORTING SHUTTLE LAUNCHES (GROWTH)	2	4	4	4	6	6	13	13	13	13	13	18	19	25	25	25	25
HEAVY LIFT VEHICLES PROCURED	1	1	0	1	3	0	5	0	0	0	0	5	0	5	0	1	0
GSO FREIGHTERS PROCURED	1	0	0	0	0	0	0	0	0	0	0	0	0	0	1	0	0
MODULE TRANSFER SETS PROCURED	0	3	3	6	12	12	25	26	27	26	26	38	39	52	52	53	54
MODULE ASSEMBLY - STATIONS (LEO)	1	1	1	2	3	3	7	7	7	7	7	10	10	13	13	14	14

	2012	2013	2014	2015	2016	2017	2018	2019	2020	2021	2022	2023	2024	2025	2026	2027	2028
SPS ADDED EACH YEAR	5	5	5	5	5	0	0	0	0	0	0	0	0	0	0	0	0
TOTAL SPS AVAILABLE	40	45	50	55	60	60	60	60	60	60	60	60	60	60	59.75	59.5	59
RECTENNAS ADDED	5	5	5	5	5	0	0	0	0	0	0	0	0	0	0	0	0
TOTAL RECTENNAS	40	45	50	55	60	60	60	60	60	60	60	60	60	60	60	60	59
GROUND OUTPUT GW ADDED	50	50	50	50	50	0	0	0	0	0	0	0	0	0	0	0	0
GROUND OUTPUT GW AVAILABLE	366.7	406.6	456.1	506.4	555.1	604.9	604.8	606.2	606.3	606.9	606.8	606.1	606.6	607.5	608.8	608.3	607.8
NUMBER OF MAKE UP MODULES ADDED	6	6	6	8	8	9	9	9	4	5	6	5	6	5	0	0	0
LOW ORBIT STATIONS IN OPERATION (FRAME)	5	5	6	6	6	0	0	0	0	0	0	0	0	0	0	0	0
TRANSMITTER STATIONS IN OP	2	2	2	2	2	0	0	0	0	0	0	0	0	0	0	0	0
GSO STATIONS IN OP (MODULE STA)	11	11	11	12	12	2	2	2	2	2	2	2	2	2	2	2	2
PERSONNEL IN LOW ORBIT	525	525	525	525	525	60	60	60	20	40	40	40	40	0	0	0	0
PERSONNEL IN HIGH ORBIT	220	220	220	240	240	60	50	50	60	50	50	50	50	50	50	50	50
HEAVY LIFT LAUNCHES PER YEAR	2881	2914	2948	2991	3022	456	456	456	436	440	440	440	440	440	417	413	413
MODULES TRANSFERRED TO HIGH ORBIT (BASIC)	60	60	60	60	60	0	0	0	0	0	0	0	0	0	0	0	0
GSO FREIGHTER TRIPS	81	91	101	111	120	120	120	120	120	120	120	120	120	120	118	118	118
SUPPORTING SHUTTLE LAUNCHES (GROWTH)	30	30	30	31	31	5	5	5	3	4	4	4	4	2	2	2	2
HEAVY LIFT VEHICLES PROCURED	0	0	0	0	0	0	0	0	0	0	0	0	0	0	0	0	0
GSO FREIGHTERS PROCURED	0	0	0	0	0	0	0	0	0	0	0	0	0	0	0	0	0
MODULE TRANSFER SETS PROCURED	66	66	66	68	68	9	9	9	4	5	5	5	5	5	0	0	0
MODULE ASSEMBLY - STATIONS (LEO)	17	17	17	17	17	3	3	3	1	2	2	2	2	0	0	0	0

	2029	2030	2031	2032	2033	2034	2035	2036	2037	2038	2039	2040	2041	2042	2043	2044	2045
SPS ADDED EACH YEAR	0	0	0	0	0	0	0	0	0	0	0	0	0	0	0	0	0
TOTAL SPS AVAILABLE	58	57	55	53	51	49	47	44	41	37	33	29	25	20	15	10	5
RECTENNAS ADDED	0	0	0	0	0	0	0	0	0	0	0	0	0	0	0	0	0
TOTAL RECTENNAS	58	57	55	53	51	49	47	44	41	37	33	29	25	20	15	10	5
GROUND OUTPUT GW ADDED	0	0	0	0	0	0	0	0	0	0	0	0	0	0	0	0	0
GROUND OUTPUT GW AVAILABLE	597.5	577.4	567.0	546.8	526.5	506.2	485.8	465.4	435.2	405.0	365.1	285.8	245.9	196.6	147.3	98.1	49
NUMBER OF MAKE UP MODULES ADDED	0	0	0	0	0	0	0	0	0	0	0	0	0	0	0	0	0
LOW ORBIT STATIONS IN OPERATION (FRAME)	0	0	0	0	0	0	0	0	0	0	0	0	0	0	0	0	0
TRANSMITTER STATIONS IN OP	0	0	0	0	0	0	0	0	0	0	0	0	0	0	0	0	0
GSO STATIONS IN OP (MODULE STA)	2	2	2	2	2	2	2	2	2	2	2	1	1	1	1	1	1
PERSONNEL IN LOW ORBIT	0	0	0	0	0	0	0	0	0	0	0	0	0	0	0	0	0
PERSONNEL IN HIGH ORBIT	50	50	50	50	50	50	50	50	50	50	50	25	25	25	25	25	25
HEAVY LIFT LAUNCHES PER YEAR	406	399	385	371	357	343	329	308	287	259	231	203	176	140	115	70	35
MODULES TRANSFERRED TO HIGH ORBIT (BASIC)	0	0	0	0	0	0	0	0	0	0	0	0	0	0	0	0	0
GSO FREIGHTER TRIPS	116	114	110	106	102	98	94	88	82	74	66	58	50	40	30	20	10
SUPPORTING SHUTTLE LAUNCHES (GROWTH)	2	2	2	2	2	2	2	2	2	2	2	1	1	1	1	1	1
HEAVY LIFT VEHICLES PROCURED	0	0	0	0	0	0	0	0	0	0	0	0	0	0	0	0	0
GSO FREIGHTERS PROCURED	0	0	0	0	0	0	0	0	0	0	0	0	0	0	0	0	0
MODULE TRANSFER SETS PROCURED	0	0	0	0	0	0	0	0	0	0	0	0	0	0	0	0	0
MODULE ASSEMBLY - STATIONS (LEO)	0	0	0	0	0	0	0	0	0	0	0	0	0	0	0	0	0

(NOT INCLUDING WEAROUT)

Fig. 6-13. Brayton Thermal Engine SPS Program

	1995	1996	1997	1998	1999	2000	2001	2002	2003	2004	2005	2006	2007	2008	2009	2010	2011
SPS ADDED EACH YEAR	0	0.25	0.25	0.50	1	1	2	2	2	2	2	3	3	4	4	4	4
TOTAL SPS AVAILABLE	0	0.25	0.50	1	2	3	5	7	9	11	13	16	19	23	27	31	35
RECTENNAS ADDED	0	1	0	0	1	1	2	2	2	2	2	3	3	4	4	4	4
TOTAL RECTENNAS	0	1	1	1	2	3	5	7	9	11	13	16	19	23	27	31	35
GROUND OUTPUT GW ADDED	0	2.5	2.5	5	10	10	20	20	20	20	20	30	30	40	40	40	40
GROUND OUTPUT GW AVAILABLE	0	2.5	5.0	10	20	30	50	70	90	110	130	160	190	230	270	310	350
NUMBER OF MAKE UP MODULES ADDED	NOT APPLICABLE																
LOW ORBIT STATIONS IN OPERATION	1	1	1	2	2	4	4	4	4	4	6	6	6	8	8	8	10
TRANSMITTER STATIONS IN OP	1	1	1	1	1	1	1	1	1	1	1	1	1	1	1	1	2
GSO STATIONS IN OP	0	1	1	1	1	1	1	1	1	2	2	2	2	3	4	4	4
PERSONNEL IN LOW ORBIT	95	45	130	240	240	475	475	475	475	475	710	710	945	945	945	945	1180
PERSONNEL IN HIGH ORBIT	0	20	20	20	20	30	30	40	50	65	75	90	105	130	155	175	195
HEAVY LIFT LAUNCHES PER YEAR	19	203	195	378	746	775	1511	1551	1592	1641	1680	2436	2506	3283	3383	3442	3536
MODULES TRANSFERRED TO HIGH ORBIT	0	1	1	2	4	4	8	8	8	8	8	12	12	16	16	16	16
GSO FREIGHTER TRIPS	3	5	3	6	12	18	30	42	54	69	78	96	114	138	162	186	210
SUPPORTING SHUTTLE LAUNCHES (GROWTH)	4	5	6	11	11	21	21	21	22	22	32	32	42	43	44	45	55
HEAVY LIFT VEHICLES PROCURED	1	2	0	2	4	1	6	1	1	1	1	8	1	8	1	1	2
GSO FREIGHTERS PROCURED	1	0	0	0	0	0	0	0	0	0	0	0	0	0	0	0	1
MODULE TRANSFER SETS PROCURED	0	1	1	2	4	4	8	8	8	8	8	12	12	16	16	16	16

	2012	2013	2014	2015	2016	2017	2018	2019	2020	2021	2022	2023	2024	2025	2026	2027	2028
SPS ADDED EACH YEAR	5	5	5	5	5	0	0	0	0	0	0	0	0	0	0	0	0
TOTAL SPS AVAILABLE	40	45	50	55	60	60	60	60	60	60	60	60	60	60	59.75	59.5	59
RECTENNAS ADDED	5	5	5	5	5	0	0	0	0	0	0	0	0	0	0	0	0
TOTAL RECTENNAS	40	45	50	55	60	60	60	60	60	60	60	60	60	60	60	60	59
GROUND OUTPUT GW ADDED	50	50	50	50	50	0	0	0	0	0	0	0	0	0	0	0	0
GROUND OUTPUT GW AVAILABLE	400	450	500	550	600	600	600	600	600	600	600	600	600	600	597.5	595	590
NUMBER OF MAKE UP MODULES ADDED																	
LOW ORBIT STATIONS IN OPERATION	10	10	10	10	10	0	0	0	0	0	0	0	0	0	0	0	0
TRANSMITTER STATIONS IN OP	2	2	2	2	2	0	0	0	0	0	0	0	0	0	0	0	0
GSO STATIONS IN OP	4	5	5	6	6	6	6	6	6	6	6	6	6	6	6	6	6
PERSONNEL IN LOW ORBIT	1180	1180	1180	1180	50	50	50	50	50	50	50	50	50	50	50	50	50
PERSONNEL IN HIGH ORBIT	220	250	275	305	330	330	330	310	330	330	330	330	330	310	330	330	325
HEAVY LIFT LAUNCHES PER YEAR	4324	4476	4524	4626	4729	1260	1260	1260	1260	1260	1260	1260	1260	1260	1256	1250	1234
MODULES TRANSFERRED TO HIGH ORBIT	16	20	20	20	20	20	0	0	0	0	0	0	0	0	0	0	0
GSO FREIGHTER TRIPS	240	270	300	330	360	360	360	360	360	360	360	360	360	360	359	357	354
SUPPORTING SHUTTLE LAUNCHES (GROWTH)	56	56	56	60	16	16	16	16	16	16	16	16	16	16	16	16	15
HEAVY LIFT VEHICLES PROCURED	10	2	2	2	2	0	0	0	0	0	0	0	0	0	0	0	0
GSO FREIGHTERS PROCURED	0	0	0	0	0	0	0	0	0	0	0	0	0	0	0	0	0
MODULE TRANSFER SETS PROCURED	16	20	20	20	20	20	20	0	0	0	0	0	0	0	0	0	0

	2029	2030	2031	2032	2033	2034	2035	2036	2037	2038	2039	2040	2041	2042	2043	2044	2045
SPS ADDED EACH YEAR	0	0	0	0	0	0	0	0	0	0	0	0	0	0	0	0	0
TOTAL SPS AVAILABLE	58	57	55	53	51	49	47	44	41	37	33	29	25	20	15	10	5
RECTENNAS ADDED	0	0	0	0	0	0	0	0	0	0	0	0	0	0	0	0	0
TOTAL RECTENNAS	58	57	55	53	51	49	47	44	41	37	33	29	25	20	15	10	5
GROUND OUTPUT GW ADDED	0	0	0	0	0	0	0	0	0	0	0	0	0	0	0	0	0
GROUND OUTPUT GW AVAILABLE	580	570	550	530	510	490	470	440	410	370	330	290	250	200	150	100	50
NUMBER OF MAKE UP MODULES ADDED																	
LOW ORBIT STATIONS IN OPERATION	0	0	0	0	0	0	0	0	0	0	0	0	0	0	0	0	0
TRANSMITTER STATIONS IN OP	0	0	0	0	0	0	0	0	0	0	0	0	0	0	0	0	0
GSO STATIONS IN OP	6	6	6	6	6	6	6	5	5	4	4	3	3	2	2	1	1
PERSONNEL IN LOW ORBIT	50	50	50	50	50	50	50	50	50	30	30	30	30	20	20	10	10
PERSONNEL IN HIGH ORBIT	320	315	305	295	285	270	260	245	230	205	185	160	140	110	85	55	30
HEAVY LIFT LAUNCHES PER YEAR	1218	1197	1155	1113	1071	1027	981	924	861	777	693	604	525	420	315	210	105
MODULES TRANSFERRED TO HIGH ORBIT	0	0	0	0	0	0	0	0	0	0	0	0	0	0	0	0	0
GSO FREIGHTER TRIPS	348	342	330	318	306	294	282	264	246	222	198	174	150	120	90	60	30
SUPPORTING SHUTTLE LAUNCHES (GROWTH)	15	15	15	14	14	13	13	12	12	10	9	8	7	6	5	3	2
HEAVY LIFT VEHICLES PROCURED	0	0	0	0	0	0	0	0	0	0	0	0	0	0	0	0	0
GSO FREIGHTERS PROCURED	0	0	0	0	0	0	0	0	0	0	0	0	0	0	0	0	0
MODULE TRANSFER SETS PROCURED	0	0	0	0	0	0	0	0	0	0	0	0	0	0	0	0	0

Fig. 6-14. Thermionic SPS Program

	1995	1996	1997	1998	1999	2000	2001	2002	2003	2004	2005	2006	2007	2008	2009	2010	2011
SPS ADDED EACH YEAR	0	0.25	0.25	0.50	1	1	2	2	2	2	2	3	3	4	4	4	4
TOTAL SPS AVAILABLE	0	0.25	0.50	1	2	3	5	7	9	11	13	16	19	23	27	31	35
RECTENNAS ADDED	0	1	0	0	1	1	2	2	2	2	2	3	3	4	4	4	4
TOTAL RECTENNAS	0	1	1	1	2	3	5	7	9	11	13	16	19	23	27	31	35
GROUND OUTPUT GW ADDED	0	2.5	2.5	5	10	10	20	20	20	20	20	30	30	40	40	40	40
GROUND OUTPUT GW AVAILABLE	0	2.5	5.0	10	20	30	50	70	90	110	130	160	190	230	270	310	350
NUMBER OF MAKE UP MODULES ADDED		NOT APPLICABLE															
LOW ORBIT STATIONS IN OPERATION	1	1	1	1	2	4	4	4	4	4	6	6	6	6	6	6	10
TRANSMITTER STATIONS IN OP	1	1	1	1	1	1	1	1	1	1	1	1	1	1	1	1	2
GSO STATIONS IN OP	0	1	1	1	1	1	1	1	1	2	3	3	3	3	4	4	4
PERSONNEL IN LOW ORBIT	85	85	110	200	200	395	395	395	395	395	590	590	785	785	785	785	980
PERSONNEL IN HIGH ORBIT		25	20	20	20	30	30	40	50	65	75	90	105	130	165	175	195
HEAVY LIFT LAUNCHES PER YEAR	18	348	340	1,368	1,372	1,384	2,744	2,752	2,760	2,777	2,760	4,162	4,172	5,544	5,660	5,580	5,609
MODULES TRANSFERRED TO HIGH ORBIT	0	1	1	2	4	4	8	8	8	8	8	12	12	16	16	16	16
GSO FREIGHTER TRIPS	3	3	5	10	20	30	50	70	90	110	130	160	190	230	270	310	350
SUPPORTING SHUTTLE LAUNCHES (GROWTH)	4	8	8	8	8	17	17	18	18	18	27	28	36	37	38	39	47
HEAVY LIFT VEHICLES PROCURED •	1	3	0	10	0	0	14	0	0	0	0	14	0	14	0	0	0
GSO FREIGHTERS PROCURED •	1	0	0	0	0	0	0	0	0	0	0	0	0	0	1	0	0
MODULE TRANSFER SETS PROCURED	0	1	1	3	4	4	8	8	8	8	8	12	12	16	16	16	14

	2012	2013	2014	2015	2016	2017	2018	2019	2020	2021	2022	2023	2024	2025	2026	2027	2028
SPS ADDED EACH YEAR	5	5	5	5	5	0	0	0	0	0	0	0	0	0	0	0	0
TOTAL SPS AVAILABLE	40	45	50	55	60	60	60	60	60	60	60	60	60	60	59.75	59.75	59
RECTENNAS ADDED	5	5	5	5	5	0	0	0	0	0	0	0	0	0	0	0	0
TOTAL RECTENNAS	40	45	50	55	60	60	60	60	60	60	60	60	60	60	60	60	59
GROUND OUTPUT GW ADDED	50	50	50	50	50	0	0	0	0	0	0	0	0	0	0	0	0
GROUND OUTPUT GW AVAILABLE	400	450	500	550	600	600	600	600	600	600	600	600	600	600	597.5	595	590
NUMBER OF MAKE UP MODULES ADDED																	
LOW ORBIT STATIONS IN OPERATION	10	10	10	10	10	0	0	0	0	0	0	0	0	0	0	0	0
TRANSMITTER STATIONS IN OP	2	2	2	2	2	0	0	0	0	0	0	0	0	0	0	0	0
GSO STATIONS IN OP	4	5	5	6	6	6	6	6	6	6	6	6	6	6	6	6	6
PERSONNEL IN LOW ORBIT	980	980	980	980	50	50	50	50	50	50	50	50	50	50	50	50	50
PERSONNEL IN HIGH ORBIT	220	250	275	305	330	330	330	330	330	330	330	330	330	330	330	330	325
HEAVY LIFT LAUNCHES PER YEAR	6,976	7,005	7,020	7,049	7,064	264	264	264	264	264	264	264	264	264	264	264	264
MODULES TRANSFERRED TO HIGH ORBIT	20	20	20	20	20	0	0	0	0	0	0	0	0	0	0	0	0
GSO FREIGHTER TRIPS	400	450	500	550	600	600	600	600	600	600	600	600	600	600	600	600	590
SUPPORTING SHUTTLE LAUNCHES (GROWTH)	48	50	51	52	18	18	18	18	18	18	18	18	18	16	16	16	15
HEAVY LIFT VEHICLES PROCURED •	15	0	0	0	0	0	0	0	0	0	0	0	0	0	0	0	0
GSO FREIGHTERS PROCURED •	0	0	0	0	0	0	0	0	0	0	0	0	0	0	0	0	0
MODULE TRANSFER SETS PROCURED	20	20	20	20	0	0	0	0	0	0	0	0	0	0	0	0	0

	2029	2030	2031	2032	2033	2034	2035	2036	2037	2038	2039	2040	2041	2042	2043	2044	2045
SPS ADDED EACH YEAR	0	0	0	0	0	0	0	0	0	0	0	0	0	0	0	0	0
TOTAL SPS AVAILABLE	58	57	56	53	51	49	47	44	41	37	33	29	25	20	15	10	5
RECTENNAS ADDED	0	0	0	0	0	0	0	0	0	0	0	0	0	0	0	0	0
TOTAL RECTENNAS	58	57	56	53	51	49	47	44	41	37	33	29	25	20	15	10	5
GROUND OUTPUT GW ADDED	0	0	0	0	0	0	0	0	0	0	0	0	0	0	0	0	0
GROUND OUTPUT GW AVAILABLE	580	570	550	530	510	490	470	440	410	370	330	290	250	200	150	100	50
NUMBER OF MAKE UP MODULES ADDED																	
LOW ORBIT STATIONS IN OPERATION	0	0	0	0	0	0	0	0	0	0	0	0	0	0	0	0	0
TRANSMITTER STATIONS IN OP	0	0	0	0	0	0	0	0	0	0	0	0	0	0	0	0	0
GSO STATIONS IN OP	6	6	6	6	6	5	5	5	5	4	4	3	3	2	2	1	1
PERSONNEL IN LOW ORBIT	50	50	50	50	50	50	50	50	50	30	30	30	30	20	20	10	10
PERSONNEL IN HIGH ORBIT	320	315	305	295	285	270	260	245	230	206	185	160	140	110	85	65	30
HEAVY LIFT LAUNCHES PER YEAR	260	252	244	236	248	216	208	196	176	164	144	128	112	88	68	44	24
MODULES TRANSFERRED TO HIGH ORBIT	0	0	0	0	0	0	0	0	0	0	0	0	0	0	0	0	0
GSO FREIGHTER TRIPS	580	570	550	530	510	490	470	440	410	370	330	290	250	200	150	100	50
SUPPORTING SHUTTLE LAUNCHES (GROWTH)	15	15	15	14	14	13	13	12	11	10	9	8	7	5	5	3	2
HEAVY LIFT VEHICLES PROCURED •	0	0	0	0	0	0	0	0	0	0	0	0	0	0	0	0	0
GSO FREIGHTERS PROCURED •	0	0	0	0	0	0	0	0	0	0	0	0	0	0	0	0	0
MODULE TRANSFER SETS PROCURED	0	0	0	0	0	0	0	0	0	0	0	0	0	0	0	0	0

• (NOT INCLUDING WEAROUT)

Program costs were derived using the RCA PRICE cost model and the Boeing PCM cost model. Their use is given in detail in the interim report of this study "Interim Report, Space Based Power Conversion and Power Relay Systems, Preliminary Analysis of Alternate Systems, May 26, 1976." Table 6-1 gives ground Rules and Assumptions.

Table 6-1. Ground Rules and Assumptions

COSTS

1. All dollars in 1976 values
2. Discount rate is 7½% on constant 1976 dollars for net present value analysis.
3. STS transportation costs are based on NASA Baseline (1971) cost per flight data escalated to 1976 values
4. Expendable propellants and fluids are included in HLLV costs All other program expendables including Nuclear Brayton NaK are excluded from program cost.
5. An allowance of 10% of hardware production cost is made to cover system spares
6. Satellite assembly is in Low Earth Orbit with no orbital manufacturing.

HARDWARE DETAILS

1. Sixty power satellites in each system generating 600 GW ground output
2. Average packaging factor for HLLV payloads is 96%
3. Numbers of ground and flight test units are based on consideration of total unit sizes and representative core section sizes.
4. STS will provide LEO crew transport with 100 person capacity payload bay pods .
5. STS will provide all verification program LEO transport.
6. No salvage consideration or values are made for any spent hardware.

ORBITAL CREW DETAILS

1. Crew Tasks
   - Deploy structural modules
   - Install solar cells and reflectors
   - Attach structural modules together
   - Attach microwave modules
   - Perform test and checkout
   - Re-perform all procedures as maintenance requires
2. Crew Work Cycle is 90 Days On-Orbit
3. Base Provisions
   - Means of operating for prolonged periods in space
   - Means of mobility throughout 10 square mile work area
   - Means of handling and controlling massive structures

HARDWARE LIFE TIME

1. STS 500 flights
2. HLLV 500 flights
3. Satellite OTV-12 flights
4. Crew OTV 20 flights
5. Power Satellite--30 years
6. Ground Rectenna - indefinite
7. Ground Control Complex- indefinite
8. LEO Base indefinite
9. GEO Base indefinite
10. GEO and LEO Manipulators-indefinite

Program costs are summarized in Tables 6-2 through 6-5. The results are given graphically in Figure 6-15.

Table 6-2. Brayton SPS Program Costs

Contract NAS 8-31628
Brayton SPS Program Cost
- 60 satellites
- Maintenance launches included

$B 1976	Program	Program ÷ 60
STS buys	7.36	0 12
STS launches	10 90	0 18
HLLV buys	134 09	2 23
HLLV launches	647 36	10 79
Chem OTV	18 38	0 31
SPS OTV	29 05	0 48
SPS (pow gen)	432 80	7 21
Xmitter	74 40	1 24
Rectenna	121 74	2 03
GEO bases	2 25	0 04
GEO service vehicle	0 37	0 01
LEO assembly sta	7 31	0 12
Ant assembly sta	1 22	0 02
Ground control	25 65	0 43
Prog mgm	11 31	0 19
	1524 19	25 40
DDT&E	41 93	0 70
	1566 12	26 10

All costs time phased over entire program with 7 5% discount rate, gave required power costs of 2 6 ¢ kWh

Table 6-3. Silicon Photovoltaic SPS Program Costs

- 60 satellites
- Maintenance launches included
- $B, 1974

	Program	Program – 60
STS buys	5 87	0 098
STS launches	9 30	0.155
HLLV buys	130 18	2.170
HLLV launches	657 08	10 951
Chem OTV	10 44	0 174
SPS OTV	57.23	0 954
SPS (pow gen)	1662 44	27 707
Xmitter	74 40	1 240
Rectenna	121.74	2 029
GEO bases	1 08	0 018
GEO service vehicle	0 37	0 006
LEO assembly sta	4 70	0 078
Antenna assembly sta	1.22	
Ground control	25 65	0 428
Program mgm	11.31	0 189
	2771 93	46.198
DDT&E	45 40	0 757
	2817 33	46.956

All costs, time phased over entire program, with 7 5% discount rate, give required power costs of 4.4¢/kWh

Table 6-4. Gallium Arsenide Photovoltaic SPS Program Costs

- 60 satellites
- Maintenance launches included
- $B, 1976

	Program	Program - 60
STS buys	3 84	0 064
STS launches	4 83	0 081
HLLV buys	68 44	1 141
HLLV launches	322 57	5 376
Chem OTV	6 14	0 102
SPS OTV	24 95	0 416
SPS (pow gen)	1328 36	22.139
Xmitter	74 40	1 24
Rectenna	121.74	2 029
GEO bases	0 89	0 015
GEO service vehicle	0 37	0 006
LEO assembly sta	4 31	0 718
Antenna assembly sta	1.22	0 020
Ground control	25 65	0 428
Program mgm	11 31	0 189
	1999 02	33 317
DDT&E	41 05	0 684
	2040 07	34 001

All costs time phased over entire program, with 7 5% discount rate, gave required power costs of 3.6¢/kWh

All costs, time phased over entire program with 7.5% discount rate, gave required power costs of 2.6¢/kWh.

Table 6-5. Thermionic SPS Program Costs

- 60 satellites
- Maintenance launches included
- $B, 1976

	Program	Program ÷ 60
STS buys	7 56	0 126
STS launches	10 90	0 182
HLLV buys	209 57	3 493
HLLV launches	1173 53	19 559
Chem OTV	30 79	0 513
SPS OTV	57 17	0 952
SPS (pow gen)	1482 59	24 710
Xmitter	74 40	1 240
Rectenna	121 74	2 029
GEO bases	2 25	0 0375
GEO service vehicle	0 37	0 006
LEO assembly sta	7 31	0 122
Antenna assembly sta	1 22	0 020
Ground control	25 65	0 428
Program mgm	11 31	0 189
	3216 36	53 606
DDT&E	43 20	
	3259 56	54.326

All costs, time phased over entire program with 7 5% discount rate, gave required power costs of 4.8¢/kWh

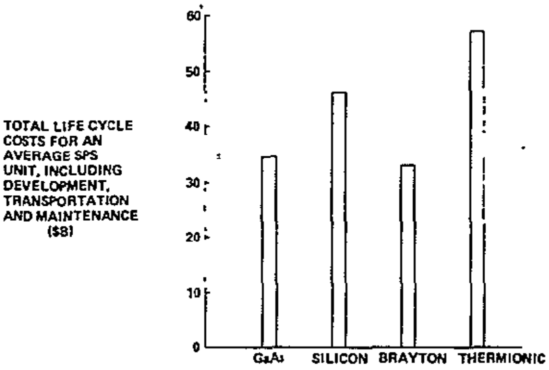

Fig. 6-15. SPS Program Costs

Net present value analysis is used to establish the present value of each system's costs and determine the value each KW-HR of ground available output must have to give the same present value. Summing the equal cost debits and generated power credits results in a zero net present value.

The process of analysis uses the cost-time spreads and power output-time spread of each SPS program. A present value for each year's costs is calculated using the following formula:

$$p = \frac{f}{(1+i)^n}$$

where
p = present value
f = future value
i = interest rate—compound
n = time periods—years

This results in 64 present values from 1978 through 2041. The present values are all summed to establish the system present value.

All SPS options produce the same electric power. A 7.5% discount rate was used to determine the required busbar cost (at the ground rectenna output) to amortize the program costs given above. These required busbar costs are given in Figure 6-2.

Power costs for the nuclear MSBR concept were estimated at 82 mills/kWh. The more advanced rotating particle bed reactor concept conceivably could provide costs in the 25 to 45 mills/kWh range.

Present value for power output is established in the same manner, except that a cost rate must first be assumed. By trial and error the cost rate is adjusted until the power output has the same present value as the system costs. The final cost rate becomes the present value cost per KW-HR.

The present value case represents a discount rate of 7.5%. A power output efficiency factor of 95% is used to allow for occultation and maintenance. The results are shown in Figure 6-16. The 7.5% case represents a possible cost of money for this project. It should be noted that 7.5% is calculated on constant 1976 dollars whereas a typical realtime rate in a 8% per year inflation would be 15.5%. The results are used for system comparison in Section 7.0.

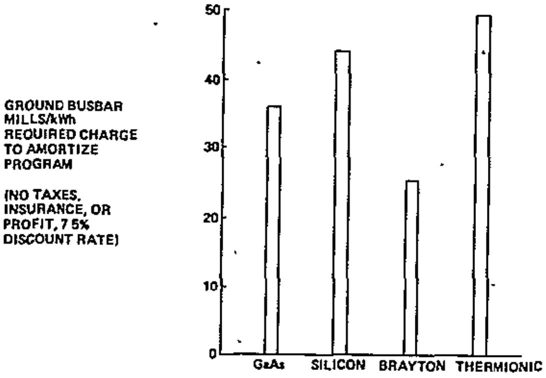

Fig. 6-16. Required Busbar Costs

7.0 COMPARISON OF CONCEPTS

7.1 APPROACH

Comparison of alternative SPS concepts should ultimately be based on factors such as:

- size
- mass
- life cycle cost
- packaging capability
- constructability
- risk
- development cost
- resources consumption

The scope of this study permitted evaluation of only the first three of these factors.

7.2 CONFIGURATION AND MASS COMPARISON

Figure 7-1 shows the emphasized concepts to the same scale. The photovoltaic systems are shown in their end-of-life (EOL) configuration i.e., the necessary modular additions have been made to compensate for radiation-induced solar cell degradation.

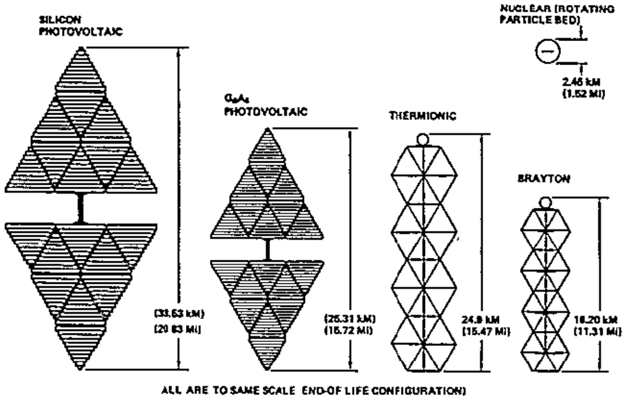

Fig. 7-1. Concepts to Same Scale (10 GW Ground Output)

Since all systems produce the same ground output and have the same microwave power transmission systems, the "solar capture" areas are inversely proportional to the energy conversion efficiency of each. The nuclear system has no solar capture area; the projected area shown is that of radiator system (which has the same area as the solar Brayton radiator system).

System masses are compared in Figure 7-2. N
the mass changes resulting from the module a
tions to the photovoltaic concept. The mass cha
to the Brayton concept results from the addi
of NaK to counter creep-induced swelling of
radiator manifolds.

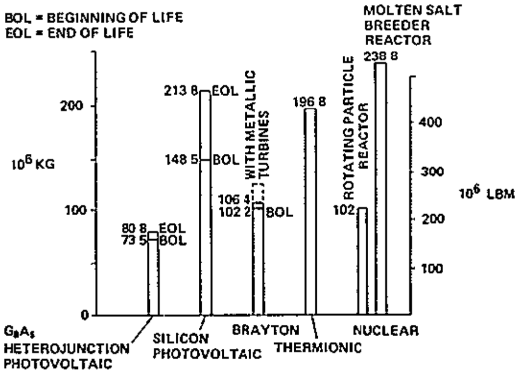

Fig. 7-2. Mass Comparison of Concepts

Cost data from the preceding section are sum
rized in Figure 7-3. The "life cycle" costs sh
here include system ground production, lau
assembly, transfer to geosynchronous orbit
maintenance for 30 years (including modular a
tions where required). No costs for system disp
at end of life were included nor was any salv
value assumed.

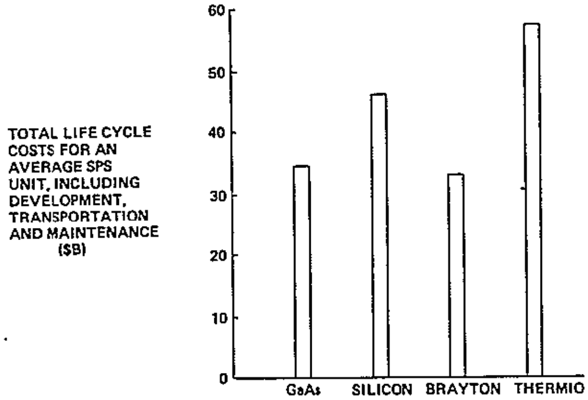

Fig. 7-3. System Life Cycle Costs

The charges for electrical power produced by t
SPS concepts was calculated on a 7.5% disc
rate. Charges are for power at the rectenna out
no distribution charges are included (nor are t
or profits). (See Section 6.0.)

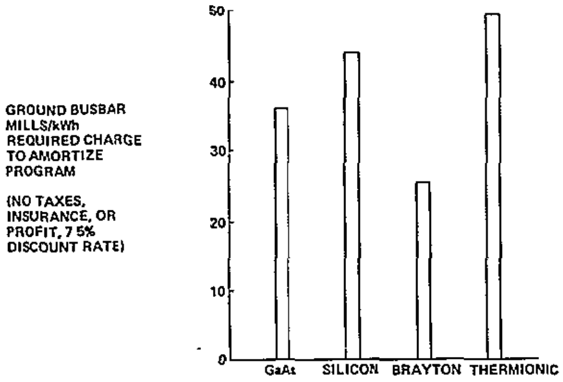

Fig. 7-4. Required Busbar Charges

7.3 ENVIRONMENTAL IMPACT

7.3.1 Exhaust Emissions

All systems require the same land use for their rectennas, since a common microwave power transmission system was baselined. Also the effects of the microwave power system itself as regards ionospheric impact, heating, sidelobes, etc., will be the same.

Effects of the launch vehicle exhaust will be in direct proportion to the mass of the system; refer back to Figure 7-2.

Table 7-1. Launch Vehicle Exhaust Emissions for Total Life Cycle of a Solar Brayton 10 GW SPS

EMISSION	MASS, 10^9KG	MASS, 10^9LBM
H_2O	1.95	4.30
CO	0.39	0.86
CO_2	0.41	0.90
H_2	0.21	0.46
Al_2O_3*	0.0017	0.0037
HCL*	0.0026	0.0057

*From solid rocket boosters of shuttle used for crew rotation.

Table 7-1 gives quantities of various exhaust products released into the atmosphere by the launches associated with a typical SPS installation (the Brayton type). The number of launches for each system is in the order of 1500, depending on system mass and includes launches for maintenance during a 30-year period. The emissions are for altitudes above 12 Km (40,000 ft.). Below this altitude, CO and CO_2 emissions would be approximately the same as above 12 Km, but H_2O would be very much less. The maximum H_2O produced would be somewhat greater than a small thunderstorm, but considerably less than a tropical thunderstorm. The chart shows probable maximum masses of nitrides of oxygen which are too small to be drawn to scale. Also indicated are masses of HCL and Al_2O_3 produced by the space shuttle in associated crew rotation launches.

7.3.2 Energy Balance

MSFC correspondence (1) directed that methods suggested in a recent article in Science (2) be considered. In (2), the author considers all energy necessary to perform functions (e.g., processing of ore to produce metal, transportation of parts, etc.) that are part of total plant construction as subsidy. Thus, the sum of all subsidies represents an energy investment and the useful energy output is the return. The ratio of the return to the subsidy is the performance index used in (2) and below.

Subsidy density (defined as kWh/kg) data has been found in many sources. Wherever possible, those sources have been used that consider primary energy by using the "input-output method of analysis" (see (2)). Also in the case of fuel and plastics, feedstock energies are included in the subsidy.

The approach used in (2) and here is somewhat new, and subsidies are not readily found for all materials or functions. All estimates for materials or functions for which no subsidy could be found were conservatively estimated.

In these calculations energy subsidies are given in terms of kW thermal, as the majority of such quantities are related to hydrocarbon fossil fuels. However, system electrical output is, of course, in kW electric. Thus "energy grade" must be considered. In (2) the method used was to multiply electrical energy by a factor of 3.5, to compensate for the inefficiency of conversion of fossil to electrical energy in power plants. This method is used here, i.e., the 30 year electrical output is multiplied by the factor 3.5. Table 7-2 summarizes the various subsidy components, in terms of their masses and energy contents for each system. The liquid hydrogen is assumed to be produced by electrolysis, and its energy subsidy has, therefore, been multiplied by the same factor of 3.5. Power availability (plant factor) is assessed at 95%.

In the example given in Table 7-2, the satellite returns in 30 years 32.63 times more energy than required to establish and maintain it; "payoff" is achieved in less than one year. Note that 90% of the energy is used in transporting the system to orbit.

Table 7-2. Energy Balance (Solar Brayton Cycle)

	Kg X 10^{-6}	Lbm X 10^{-6}	kWh_{th} X 10^{9}	BTU X 10^{12}
Aluminum	26.17	57.71	2 07	7 05
Magnesium	1.15	2 53	0 13	0.45
Steel	10.6	23 48	0 17	0 58
Tedlar/Kapton	0.61	1.33	0.02	0 05
Min-K	1 80	3 96	0.09	0.31
Copper	4 66	10.27	0 08	0.26
Niobium	24.27	53.5	1 33	4.56
Beryllium	6.69	14.74	0 37	1 26
Haynes-188	5.92	13 06	0 39	1 31
NaK	20.39	44 95	0.08	0 28
			4.72	16.11
Ground Transportation (SPS Materials)				
300 mi (Rail)			0.0066	
200 mi (Truck)			0 0185	
			0.0251	0.086
30 Year Replacement Parts				
NaK	4 49	9 89	0.018	0.061
Other	12 24	27.09	0.492	1.677
	16 77	36.98	0.523	1 738
Orbit Transfer of SPS and Parts				
Argon	60.04	132 39	0.180	0.615
LH_2	2.36	5.21	0.463	1.581
LO_2	16.45	36 28	0.049	0 168
Propulsion Modules	0.33	0.73	0.722	2 464
Assembly Station	0 05	0.12	0.005	0.016
Flights of Low Orbit Transport System				
	X 10^{2}	X 10^{2}		
LO_2	74.97	265.3	22.56	76 99
RP	5.11	11.26	9.00	30 73
LH_2	10.98	24.24	215.54	735 65
			247.11	843.38

Rectenna and Transmission Corridor (Nominal Length, 100 KM = 62 S Mi.)

Area lost to farming — Assume acreage in corn and complete loss during 30 yr.

	Energy lost	30 Yr. Energy Loss (KW Hrs.)	BTU
Rectenna 100 KM^2	2.5 X 10^{8} kWh/Yr.	7 5 X 10^{9}	22.0 X 10^{12}
Transmission Corridor 100 KM^2	2.5 X 10^{8} kWh/Yr.	7 5 X 10^{9}	22 0 X 10^{12}
		15.0 X 10^{9}	44 X 10^{12}
TOTAL		2.68 X 10^{11} kWh	9.13 X 10^{14} BTU

30 Yr X 10 GW X 0 95 Availability = 2.50 X 10^{12} kWh

$$\frac{2.5 \times 10^{12}\ \text{kWhe} \times 3.5}{2.68 \times 10^{11}\ \text{kWh}} = 32\ 63$$

7.4 OVERVIEW

As explained in Section 3.1, several SPS concepts were de-emphasized for a variety of technical reasons. However, the net result of this study is that "power from space" is not dependent upon a single power generation concept. Analyses of the exhaust emission quantities of the associated launch systems, rectenna land use, etc. indicate that the environmental impact associated with the SPS concept is extremely low.

The baseline program would produce the first commercial power from space in 1996. This would be by no means an "accelerated" program; SPS operation could probably be achieved at a much earlier date.

REFERENCES

1. MSFC Letter, W. E. Whitacre to D. Gregory, Subject: "Energy Balance Analysis," October 30, 1975.
2. Gilliland, M. W., "Energy Analysis and Public Policy," Science, September 26, 1975.

8.0 SPS DEVELOPMENT

8.1 DEVELOPMENTAL GOALS

SPS development as defined here culminates upon the achievement of:

- successful operation of a full-size orbital power generation system and a full size microwave power transmission system (MPTS) of "ready-for-production" configurations.
- successful operation of all space transportation systems, including the heavy lift launch vehicle (HLLV), crew rotation vehicles and a system for transfer to geosynchronous orbit (either by "conventional" chemical orbit transfer vehicles or by electric "self-power" transfer).
- successful operation of all orbital production and support facilities (but not necessarily in the quantities required for full SPS production).

This is to be contrasted with the current SPS status, which essentially consists of system concepts established by analytical studies, plus the NASA/JPL MPTS tests.

8.2 RECOMMENDED DEVELOPMENT PROGRAM

The program recommended here consists of four parts:

I Expanded Analysis and Ground Experiments
II Shuttle Based Demonstrations
III Precursor System Development & Demonstration
IV Operational System Development & Demonstration

The following sections expand upon these four program parts.

8.3 EXPANDED ANALYSIS AND GROUND EXPERIMENTS (PART I)

As a minimum, the following elements should be included:

1. Expanded system analysis (at perhaps five to 10 times the CY 1977 funding level) to allow concept selection and detailed definition.
2. Tests of the geosynchronous orbit environment (as now known) upon candidate materials, solar cells, etc. Repeated cycles of solar cell exposure/annealing should be included. Life of components in this environment should be predicted.
3. Ground tests of a phased-array transmitter phase locked to the pilot transmitter of a small rectenna (JPL "billboard").
4. Development tests of automated space production systems should begin, possibly in neutral buoyancy tanks.
5. Tests of microwave effects on flora and fauna should begin, to generate data necessary for the establishment of microwave standards.
6. Tests of ionospheric heating effects by ground-based transmission of a high power beam.

8.4 SHUTTLE BASED DEMONSTRATIONS (PART II)

As the shuttle becomes available, the following program elements should be undertaken:

1. Launch to geosynchronous orbit (possibly by IUS) of long duration experiments to fix precisely the geosynchronous orbit environment (meteoroids, radiation, etc.).
2. Launch to geosynchronous orbit (possibly by IUS) of one or more payloads to conduct interferometric transmissions to a network of ground receivers to evaluate MPTS operation through the ionosphere.
3. Tests of automated beam machines and other aspects of large area, in-space fabrication, including development of timelines, manning requirements, need for lighting, etc.
4. Tests of full scale candidate microwave power transmitter "tubes."
5. Tests to determine potential effects of low orbit operations, such as thermal cycles, due to repeated occultations.

8.5 PRECURSOR SYSTEM DEVELOPMENT AND DEMONSTRATION (PART III)

The necessity for, and form of, an SPS precursor system has been a subject of debate by those studying the SPS concept. Views of the precursor program have ranged from none, to a small "pilot plant" of perhaps 1 MW orbit busbar, to a larger pilot plant of perhaps 50 MW orbit busbar (1 MW rectenna output) to a 1000 MW ground output "commercial demonstrator." A significant aspect of this range of options is that the space shuttle is adequate to launch all except the commercial demonstrator, although there would be a cost and environmental impact benefit to the use of a liquid booster "growth shuttle."

In general, space projects are lowest in total cost, if performed expeditiously, i.e., in an accelerated fashion; "stretchouts" are costly. An early commitment to a large scale precursor program entails more financial risk, but could speed the date of space power availability.

Selection of a detailed precursor program plant will probably involve analysis and trades in Part I and Part II, followed by "national" decisions, i.e., Presidential and Congressional approval.

As a "middle-of-the-road" approach to selection of a precursor program activity level a 50 MW orbit busbar, 1 MW ground output pilot plant is here baselined. Program elements are:

1. Selection and design of the orbital power generation system and the microwave power transmitter.
2. Ground and shuttle sortie tests of elements of the above.
3. Selection and design of orbital assembly equipment for the "pilot plant."
4. Equipment ground fabrication.
5. Launch, assembly and checkout of the orbital assembly facility.
6. Launch of the pilot plant system hardware. If low orbit assembly and "self-power" transfer is selected approximately 50 shuttle flights would be required. Assembly at geosynchronous orbit, with parts transfer from low orbit by chemical OTV, would require approximately 100 shuttle flights.
7. Construction and tests of the ground test rectenna system.
8. Assembly and checkout of the orbital systems.
9. Long term microwave power transmission tests, including ionospheric effects tests.

8.6 OPERATIONAL SYSTEM DEVELOPMENT & DEMONSTRATION (PART IV)

In addition to the full size SPS system, rectenna, construction facilities, etc., the heavy lift launch vehicle and high orbit transfer systems must be developed. The HLLV might conceivably be begun quite early, perhaps even in Part II.